3D Ultrasound-based Patient Positioning for Radiotherapy

by

Michael Haizhou Wang

B.E.(Hons), University of Canterbury, New Zealand, 2003

A THESIS SUBMITTED IN PARTIAL FULFILMENT OF
THE REQUIREMENTS FOR THE DEGREE OF

Master of Applied Science

in

The Faculty of Graduate Studies

(Electrical and Computer Engineering)

The University Of British Columbia

August 8, 2006

Abstract

A novel 3D ultrasound-based patient positioning system for target localisation during radiotherapy is described. This system incorporates the use of optically tracked dedicated 3D ultrasound probes to acquire images of the target anatomy during both the radiotherapy simulation and treatment procedures. The ultrasound scan taken during simulation is registered to the planning CT so that the prescribed dose plan can be transferred to the simulation ultrasound coordinates. Finally, this ultrasound is registered to the treatment ultrasound image using a rigid-body intensity-based registration algorithm to localise the target at the time of treatment.

This thesis first describes the method for registering CT and 3D ultrasound scans taken during the radiotherapy simulation procedure using infra-red LED (IRED) markers of the optical position sensing system directly as fiducial markers in CT. This approach was tested on a phantom and a RMS target registration error (TRE) of $1.09mm$ was achieved. In addition, an automatic intensity-based registration algorithm was shown to be capable of registering 3D ultrasound images acquired from the neck of a volunteer.

Finally, a novel experimental technique is described which allows the entire radiotherapy treatment process using the proposed 3D ultrasound-based patient positioning system to be simulated. This method uses polymer gel dosimetry to record the dose delivered to a phantom, allowing this to be compared to the intended dose plan, thereby closing the loop on the entire treatment process.

The mean target localisation accuracy of the proposed system was $2.5mm$ for 4 target locations inside the phantom, compared to $1.6mm$ obtained using the conventional patient positioning method of alignment lasers. These results suggest that 3D ultrasound-based target localisation is practically feasible and and potentially capable of increasing the accuracy of patient positioning for radiotherapy treatment in sites where day-to-day organ shifts are greater than $1mm$ in magnitude.

Contents

List of Tables

List of Figures

Notation

${}^{\mathbf{A}}\mathbf{x}$	Homogeneous coordinates of point $\underline{x}$ in coordinate system $\{\underline{o}_A, \underline{C}_A\}$.
${}^{\mathbf{B}}\mathbf{T}_{\mathbf{A}}$	Homogeneous transformation matrix from coordinate system A to coordinate system B.
$\underline{C}$	Frame.
$\underline{x}$	Vector.
$\underline{x}$	Point.
$\{\underline{o}_A, \underline{C}_A\}$	Coordinate system A.
${}^{A}x$	Coordinates of point $\underline{x}$ in coordinate system $\{\underline{o}_A, \underline{C}_A\}$.

Glossary

2D Two dimensional.

3D Three dimensional.

4D Four dimensional. In this thesis, 4D refers to 3 spatial dimensions plus one time dimension.

BB Ball bearing.

BEV Beam's eye view. A rendering of patient anatomy viewed from the perspective of the source of radiation.

CBCT Cone-beam CT.

CCD Charge-coupled device.

3D-CRT Three-dimensional conformal therapy. A treatment technique which allows dose distributions to be conformed to the target volume in 3D, excluding as much healthy tissue as possible.

CT Computed tomography.

CTV Clinical target volume. Includes the GTV and suspected tumour.

DOF Degree of freedom.

DRR Digitally reconstructed radiograph. Images reconstructed from acquired CT information resembling a radiograph depicting the beam's eye view (BEV) of the treatment field anatomy.

fraction The total dose delivered to the tumour during a course of radiation therapy is divided and administered in small daily doses, or fractions.

GTV Gross tumour volume. The demonstratable tumour.

HU Hounsfield unit.

IGRT Image-guided radiotherapy. The use of medical imaging inside the treatment room to improve the accuracy of radiation delivery.

IMRT Intensity-modulated radiation therapy. A treatment technology which allows nonuniform exposure across the beam's eye view (BEV).

interfractional Occurring between radiotherapy treatment fractions.

intermodality Images acquired using different sensors.

intrafractional Occurring during the radiotherapy treatment fraction.

intramodality Images acquired using the same sensor.

IRED Infrared light emitting diode.

isocenter The point of intersection of the three axes of rotation (gantry, collimator and couch) of the treatment unit.

kV Kilovoltage.

LINAC Linear accelerator. A radiotherpy treatment unit that produces x-rays or electrons for treatment.

MV Megavoltage.

portal imaging Radiograph depicting the beam's eye view (BEV) of the treatment anatomy generated using megavoltage electrons produced by the treatment unit.

PTV Planning target volume. Includes the CTV and margins for geometric uncertainties.

RMS Root-mean-squre.

ROI Region of interest.

TRE Target registration error.

treatment field (portal) The volume exposed to radiation from a single radiation beam.

Acknowledgements

This work would not have been possible without the contribution and assistance of many individuals. First and foremost, I wish to thank my supervisor, Dr. Robert Rohling, for giving me the opportunity to pursue my studies in his lab at UBC. His generous support, constant encouragement, and valuable insights throughout my time here has made my studies a thoroughly rewarding experience.

I would like to express my gratitude to the staff of the Medical Physics Department at the British Columbia Cancer Agency. In particular, I would like to thank Dr. Brenda Clark for generously giving her time to answer the many questions I had about radiotherapy, and providing me with contacts so that I could pursue this area of research. I would like to thank Dr. Cheryl Duzenli for her expertise and advice on polymer gel dosimetry, and providing me access to the cancer agency's treatment unit. I am very grateful to Dr. Susan Zhang for assisting me with large portions of my practical work at the cancer agency, and spending time after hours so that I could complete my experiments. I thank Kurt Luchka for help in CT scanning. I would also like to thank Carol Marlowe for constructing the immobilisation mask used in my experiments.

I gratefully acknowledge Dr. Andrew Jirasek of the Department of Physics and Astronomy at the University of Victoria for providing instructions on polymer gel manufacture.

I would like to thank all my lab mates in the Robotics and Control Lab for their friendship and support. In particular, I thank Dr. Neculai Archip for his valuable assistance in conceptualising this project initially, and his helpful discussions. I am also grateful to Tony Poon for allowing me to use his ultrasound probe calibration method. I would like to thank Hani Eskandari for fearlessly volunteering to become the man behind the immobilisation mask in my experiments.

Finally, I want to say thanks to all my family and friends for their words of inspiration and encouragement, wherever they may be. This is for you, mom.

Chapter 1

Introduction

The aim of radiotherapy treatment is to deliver a lethal dose of radiation to the tumour while minimising the exposure of surrounding healthy tissues to radiation. In external beam radiotherapy[1], errors in patient positioning at the time of treatment leads to either geometric miss of the target volume and reduced tumor control, or irradiation of greater amounts of healthy tissue and increased morbidity. Therefore, accurate daily repositioning of patients throughout a course of fractionated radiation therapy is of paramount importance.

With the advent of conformal treatment techniques such as three-dimensional conformal therapy (3D-CRT) and intensity-modulated radiation therapy (IMRT), 3D dose distributions which accurately match the shape of the target volume can now be achieved, facilitating increases in radiation dose to tumor sites and reductions in treatment margins. However, one of the weakest links in the radiotherapy treatment process remains patient positioning [111], which poses a significant challenge to the implementation of these techniques in clinical practice.

This thesis presents a 3D ultrasound-based patient positioning system for radiation therapy, shows that it is feasible to implement in practice, and demonstrates its capability in positioning a phantom object inside the treatment room. This chapter begins with an overview of the major processes involved in a course of radiotherapy treatment, followed by a description of the most significant sources of positioning errors, and will end with an outline of the thesis structure as well as its main contributions.

[1]Hereafter simply referred to as 'radiotherapy' or 'radiation therapy'.

1.1 The Radiotherapy Treatment Process

The typical steps involved in implementing a course of radiotherapy in current practice are summarised in Figure 1.1 and are described in the following subsections. It must be noted that patients treated with radiation therapy will be involved in numerous other procedures, from diagnosis to ongoing patient follow-up, which are not shown here. The experience of every individual patient will also vary depending on their condition, type and extent of disease, as well as protocols at different treatment centers.

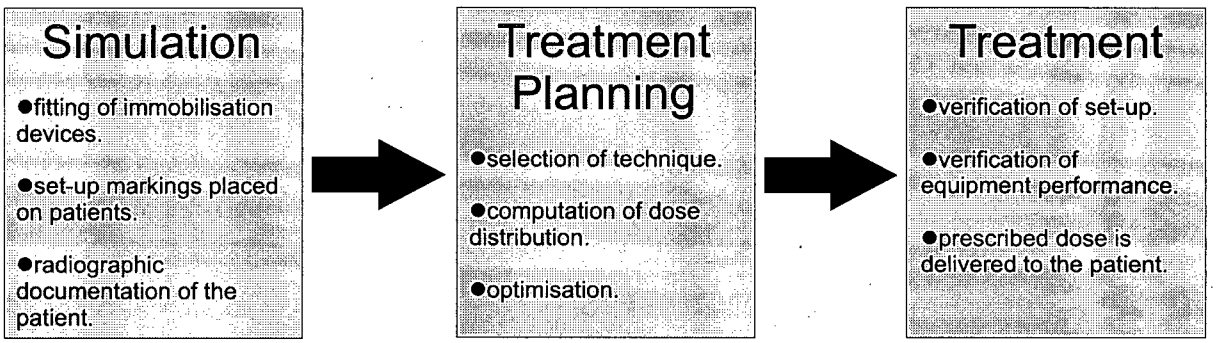

Figure 1.1: Major steps involved in the process of radiotherapy.

1.1.1 Simulation

The primary purpose of the simulation procedure is to assist physicians in the treatment planning process. Traditionally, this was accomplished by taking radiographs of the patient using a device called a simulator, which duplicated the mechanical, geometrical, and optical parameters of treatment units. In the early 1990s, dramatic improvements in computed tomography (CT) image quality meant that CT images of the patient could now be used for treatment planning purposes. High quality digitally reconstructed radiographs (DRR) could be generated from CT data to allow CT, or 'virtual' simulation to take place. This had a number of advantages over conventional, or 'physical' simulation, including minimising patient attendance, allowing more complex beam configurations to be simulated, and enabling full 3D verification of beam coverage. As a consequence, the need for conventional simulation has been made largely redundant.

The process of CT simulation[2] begins with the patient positioned on the couch of a CT scanner in the treatment position. If necessary, immoblisation devices are used to help minimise patient motion. To establish a consistent coordinate system between the CT simulator and the treatment unit, a laser alignment system that casts long lines ($> 1m$) on the body of the patient is used. An identical set of alignment lasers in the treatment room is employed. These lines correspond to the orthogonal axes of the the linear accelerator (LINAC)[3], and intersect at at the common point of all machine rotations (isocenter). The coordinate system of the treatment unit is illustrated in Figure 1.2.

Once the patient's position has been secured, the laser lines on the patient are permanently marked on the skin or on the immobilisation device to facilitate repositioning for each treatment fraction. In addition, radiopaque markers, such as lead ball bearings (BBs), are adhered to the patient on top of the markings to establish a reference for the alignment lines in the CT image. Usually, three BBs at the center of the laser crosshairs are used to indicate the lateral and anterior-posterior axes of the treatment unit.

The CT scanning process begins with a pilot scan to determine the region of interest over which axial slices will be acquired. These slices are then scanned using the established imaging protocol for the anatomical site to be treated. At the completion of the CT scan, the patient is free to leave, the image data is reconstructed and transferred to the treatment planning workstation.

1.1.2 Treatment Planning

Treatment planning is the process by which dose delivery is optimised for a given patient and clinical situation. It begins with identification and contouring of the target volume and critical normal structures on each slice of the patient CT data. Margins around tumour bearing regions are also defined according to the standards set in [1], which is outlined in Figure 1.3. The contouring process is not automatic and is indeed the most labour-intensive part of the treatment planning procedure.

After target and anatomy delineation, the appropriate treatment machine parameters are

[2]Hereafter simply referred to as 'simulation'.

[3]The terms 'treatment unit' and 'LINAC' will be used interchangeably in this thesis.

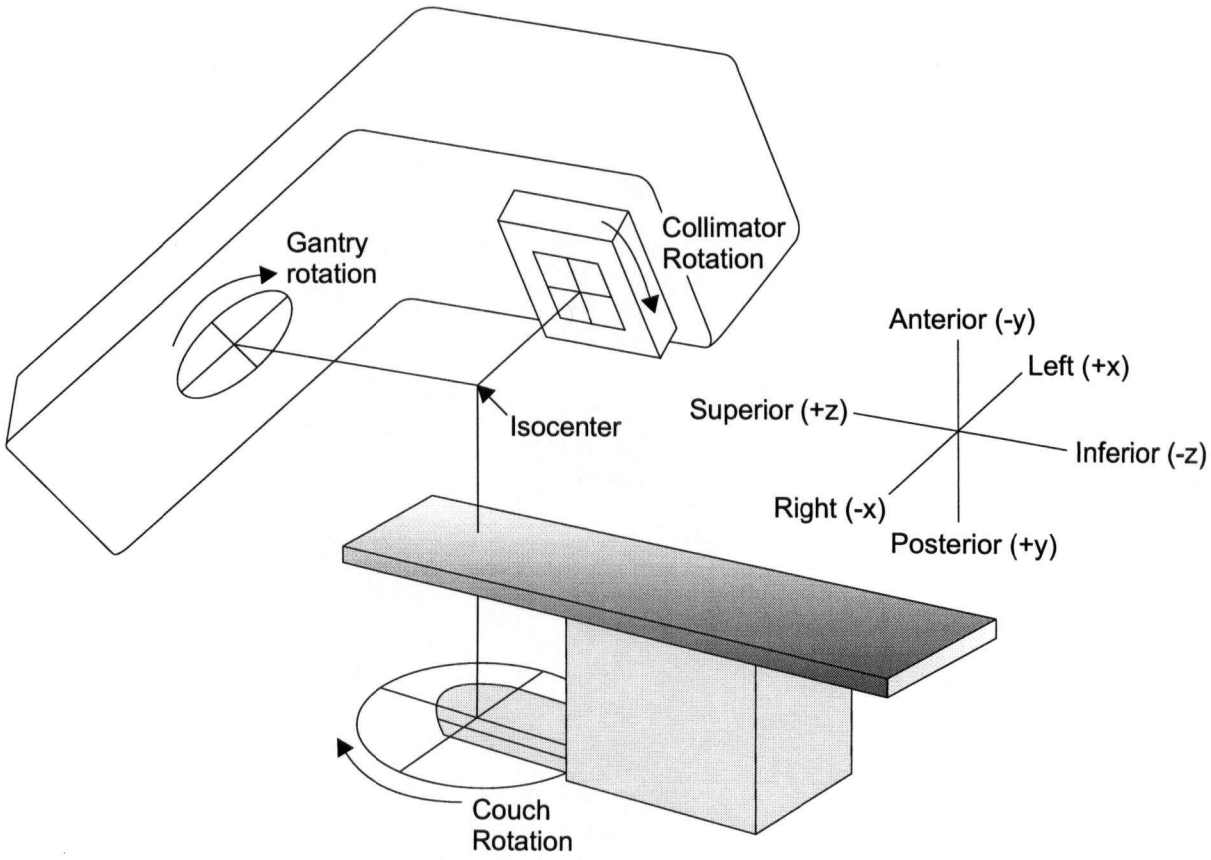

Figure 1.2: The LINAC coordinate system. The common point of the gantry, collimator, and couch rotation is the machine isocenter and origin. The conventional names for the axes are also shown. The gantry rotates around the z axis, the couch around the y axis, while the collimator axis of rotation depends on the gantry angle. Redrawn from Bentel, 1999 [6].

selected in the treatment planning system. The orientation and shape of treatment beams are then arranged to maximise the dose to the PTV while minimising dose to critical structures. The radiopaque markers appearing in the CT scan, which correspond to patient skin marks, are used to establish the origin and coordinate system of the plan. The location of the isocenter, which is usually positioned at the center of the PTV, is defined with respect to the plan coordinates. Recall that the LINAC rotates around the isocenter. This enables the target to be irradiated from different directions without moving the patient. Once the beams have been set up, the amount of dose to be delivered from each beam is determined.

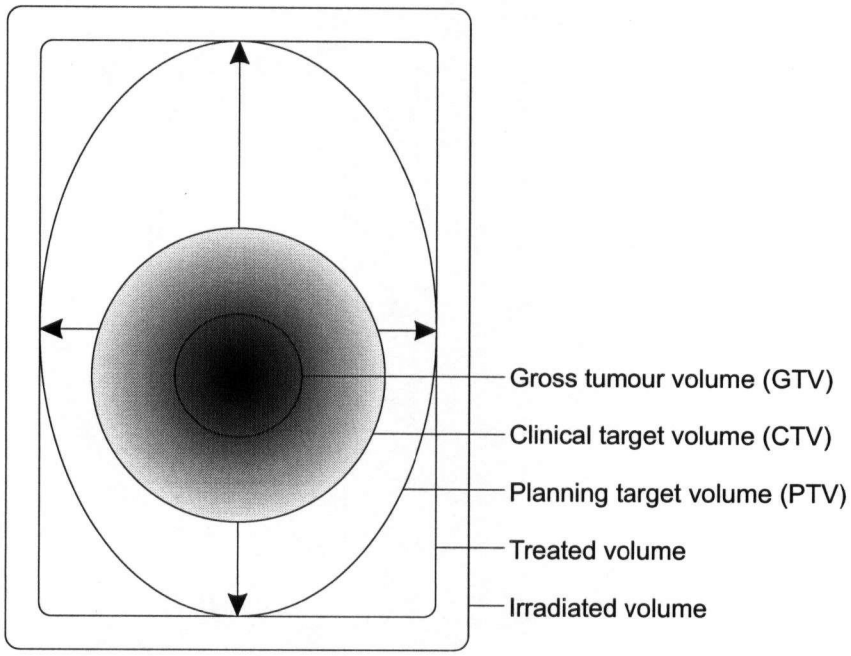

Figure 1.3: Target margins used in radiation therapy. The *GTV* contains the gross palpable or visible tumour. The *CTV* contains the *GTV* and surrounding tissue with possible (subclinical) disease. The *PTV* contains the *CTV* plus margins to account for geometric uncertainties in treatment. The *PTV* margin around the *CTV* is not necessarily symmetric, as greater spatial uncertainty in the target position may exist in one direction than another. The *treated volume* is enclosed by the prescription isodose surface chosen to achieve the purpose of treatment. Due to limitations in treatment delivery, the *treated volume* is always bigger than the *PTV* and usually has a simpler shape. The *irradiated volume* contains tissue that receives a dose considered significant in relation to tissue tolerance. Redrawn from International Commission on Radiation Units (ICRU) Report #50 [1].

Finally, to evaluate the plan, dose calculations are made. Dose distributions are computed using previously delineated contours of relevant anatomical features and electron density values derived from CT numbers. Each treatment plan is assessed to decide if it can be used to deliver the prescribed dose under target dose homogeneity and normal tissue protection constraints. The complexity and viability of the plan is also reviewed before approval.

1.1.3 Treatment Delivery

A course of radiation therapy typically involves up to thirty or more fractions, given on a daily basis, over a period of six or seven weeks. During each treatment session, the patient's position on the couch during simulation must be duplicated. Any immobilisation devices used during simulation are again employed. By using the motorised couch, the patient is brought into correct position with the aid of alignment lasers inside the treatment room and markings on the skin.

During the first treatment session, the offset of the planned isocenter location from the treatment plan origin (defined by the skin marks placed during simulation), must also be taken into account. This offset is implemented using couch shifts. The laser alignment lines at this new position are clearly marked on the patient and used for set-up on subsequent fractions.

With the patient in correct treatment position, the LINAC isocenter should be in exact alignment with the target isocenter on the treatment plan. The accurate alignment of these two points, as well as the correct orientation of the patient with respect to the LINAC axes, are crucial for the successful execution of the treatment plan.

Once the patient is positioned for treatment, beam configuration, gantry, collimator, and couch angles are set for irradiation of the first field. If desired, portal images, generated using the megavoltage (MV) beam of the LINAC, can now be taken and compared with DRRs from simulation to verify placement of the isocenter, beam position, and beam shape. Portal images are usually taken at the first treatment session to assess systematic errors in translating the treatment set-up from the simulator to the treatment unit. Thereafter, the frequency of portal imaging is based on established treatment protocols, but once every week is an accepted standard [56].

Finally, after the radiation therapist is satisfied that all treatment parameters are met, the radiation beam is turned on, and the prescribed dose is delivered. Most treatment plans require radiation delivery from more than one field. The radiation therapist must ensure that the patient remains stationary on the couch for the entire procedure. The treatment session ends when all fields of the treatment plan is delivered. The entire session typically lasts up to 20 minutes.

1.2 Treatment Uncertainties

Although every step of the radiotherapy treatment process is carefully carried out, there are inevitably uncertainties in the planning and delivery of radiation therapy. These can be broadly divided into two groups: those relating to dose (variabilities in machine output, inaccuracies in dose calculation algorithms), and geometrical uncertainties between the patient and radiation beam. Geometrical errors can further be reduced to mechanical uncertainties in the equipment, or patient-related uncertainties.

In the following subsections, the most significant sources of geometrical uncertainties in radiotherapy will be described, as well as strategies for their control. Approximate magnitudes of these uncertainties are taken from the text by Bentel [6], and if noted, other sources in the literature. Patient-related uncertainties will be emphasised, as this is particularly difficult to eliminate, and is presently the subject of considerable research efforts.

1.2.1 Mechanical Uncertainties

Various sources of mechanical uncertainties, and their approximate magnitudes are shown below:

Isocenter Deviations may occur due to sagging of the machine ($\sim 2mm$).

Couch There are differences in sag between couches ($5 - 10mm$). Couch tops may also become tilted with extensive use.

Laser Alignment system Lines may not intersect at isocenter ($< 5mm$) or be perpendicular. Lines may have a thickness of up to $3mm$.

Field size settings Mechanical dials, often with a resolution of $0.5cm$, may have a error of $\sim 2mm$.

Rotational settings Mechanical dials, often with a resolution of $1°$, may have a error of $\leq 1°$.

Many sources of mechanical errors may be reduced by rigorous quality-assurance testing of radiotherapy equipment on a daily, monthly, or annual basis. Other uncertainties are inherent in

the system (for example, width of alignment lines, resolution of motor driven parts) and cannot be eliminated. The couch tops used in simulation should match those used in treatment to avoid discrepancies.

1.2.2 Patient-Related Uncertainties

Various sources of patient-related uncertainties, and their approximate magnitudes are shown below:

Target Delineation Error in determining the extent of the tumour from simulation data may be up to $5mm$.

Organ Motion This may be divided into two categories: intrafractional motion (e.g., respiratory, cardiac), occurring during the treatment session, and interfractional motion (e.g., bowl movements, bladder filling), occurring between treatment fractions. The extent of organ motion varies considerably among different anatomical sites. For example, interfractional motion of the prostate has been measured by many authors to be in the order of $5 - 10mm$ [57]. Meanwhile, intrafractional motion of the liver has been measured to be in the order of $10 - 20mm$ [57].

Skin Marks These may shift with respect to underlying tissue ($\sim 5mm$), especially in areas with thick soft tissue.

Patient Motion Some patients, especially children, may move ($\sim 5mm$) during radiation delivery.

Patient-related uncertainties are difficult to eliminate. They are an accepted part of radiotherapy and treatment plans are made with adequate margins to accommodate their effect. Recall from Figure 1.3 that the CTV contains a margin around the GTV to account for volumes of suspected tumour, and that the PTV contains a margin around the CTV to account for geometric uncertainties and beam penumbra. A minimum margin of $5mm$ is typically used around the GTV, while a $1.5cm$ margin is often set around the CTV [6].

A number of strategies are available to reduce the magnitude of patient-related uncertainties. Respiratory motion may be reduced by asking the patient to breath quietly during treatment or to perform breath-holding while the radiation beam is on. Respiratory gating is a technique whereby the patient is allowed to breath freely while a sensor monitoring the phases of the respiratory cycle is used to gate the radiation beam [76].

Patient repositioning accuracy and their ability to maintain the correct treatment position may be improved through the use of immobilisation devices. Many forms of immobilisation aids exist, including thermoplastic facial masks moulded to the patient's facial contour, dental fixation, foam body moulds, and stereotactic head frames for intracranial targets. Immobilisation devices have the added benefit of allowing set-up marks to be placed on rigid surfaces rather than mobile surfaces of the skin.

Consistency of organ size and location may be maintained by requesting the patient to adhere to guidelines such as having an empty or full bladder, or not eating immediately prior to treatment. Air-filled rectal balloons may used to ensure consistent daily prostate location [73].

An attractive option for dealing with organ motion, and an active field of research, is the use of image-guidance inside the radiotherapy treatment room. Images of the patient anatomy are acquired in order to locate the position of the target with respect to the treatment unit immediately prior to the commencement of daily treatment. Corrections to the patient position can then be made to bring the planned isocenter into alignment with the LINAC isocenter before irradiation. Several imaging modalities have been used or are under investigation for this purpose, including ultrasound, CT, and electronic portal imaging. Current research in image-guided radiotherapy (IGRT) will be reviewed in Chapter 2.

1.3 Thesis Outline

This thesis presents a novel 3D ultrasound-based patient positioning system for image-guided radiotherapy treatment. The unique aspects of this system include:

- Use of dedicated 3D probes for acquiring ultrasound scans of the patient anatomy.

- Use of explicitly registered simulation CT and ultrasound scans to transfer planned dose information.
- The ability to use automatic intramodality image registration algorithms to compare patient anatomy at the time of treatment to the simulation session.

In Chapter 2, the current state-of-the-art in IGRT systems will be reviewed. Techniques will be classified according to the modality used to image the patient inside the treatment room, and strengths and weaknesses of each approach will be discussed. The chapter will conclude by presenting the problems which are to be addressed by the remainder of this thesis.

In Chapter 3, the proposed 3D ultrasound patient positioning system will be presented. The hardware components of the system will be described, followed by the envisaged treatment protocol when the system is used to position patients. Finally, all the coordinate transforms used by the proposed system to localise the patient inside the treatment room will be described and compared to other similar systems using a common mathematical framework.

In Chapter 4, proof of concept tests demonstrating the practical feasibility of the proposed system are described. In particular, the accuracy of the technique used to register simulation CT and ultrasound scans are evaluated on a phantom. To investigate whether 3D ultrasound volumes of real anatomy can be registered using automatic pixel-intensity based methods, an experiment performed on images collected from the neck of a volunteer is presented.

In Chapter 5, a novel experimental method which allows the entire radiotherapy treatment process to be simulated on a phantom is presented. This enables the location of the final delivered dose to be compared to the planned dose, thereby closing the loop on the entire treatment process using the proposed system. The experimental approach used may be extended to evaluate the accuracy of other image-guidance systems for radiotherapy as well. No previous work has shown this type of validation.

Finally, in Chapter 6, conclusions derived from the work presented in this thesis will be given. The main benefits of the proposed patient positioning system will be summarised, as well as the contributions of this thesis. Future work required to fully implement the system inside the clinic will be outlined.

Chapter 2

Image-Guided Radiotherapy

Numerous new technologies are allowing radiation oncologists to increase doses to tumour sites, while achieving conformal avoidance of normal tissue. Three dimensional conformal therapy (3D-CRT) uses six or more fields with different shape and beam angle to achieve target dose escalation and a sharp dose fall-off in healthy tissue. Intensity modulated radiation therapy (IMRT) adds an extra degree of freedom by using non-uniform exposure across the beam's eye view (BEV). The precision of treatment is now limited only by the fidelity and acuity of the image representation of the patient before and during the course of treatment [67]. In response, radiotherapy is rapidly entering the image-guided era [64].

Image-guidance in radiotherapy can be defined as the use of medical imaging inside the treatment room to improve the accuracy of radiation delivery. Essential elements of an ideal IGRT system include [64]:

- 3D imaging capability of soft tissues including tumours.
- efficient acquisition and comparison of images.
- an effective process for clinically meaningful intervention.

Both technological and cost restrictions mean that the above features are only met to a degree by existing IGRT systems. Intervention techniques are largely influenced by the imaging capability available. These strategies may be classified according to the frequency at which corrective action is taken. At the most basic level, patient images can be analysed off-line after delivery and correction strategies implemented at the next treatment fraction. At the most advanced, images are acquired and processed in real-time during the delivery process and corrective action taken immediately.

The spectrum of image-guidance strategies for radiotherapy is presented in Table 2.1, along with the enabling imaging technology and the type of set-up error each strategy is able to cope with. Although real-time guidance would be the ideal solution, the most clinically meaningful method of utilising treatment image information will ultimately depend on the specific disease site and clinical application. For example, in disease sites where intrafractional motion is insignificant and targets are associated with bony landmarks, on-line correction using 2D portal imaging alone may prove to be sufficient [37].

Table 2.1: Spectrum of image-guidance strategies for radiotherapy.

Image-guidance strategy	Frequency of intervention	Range of errors able to be corrected	Enabling imaging modality
Off-line correction	Usually weekly	Systematic error (deviation from average target location)	Portal imaging (film)
On-line correction	Daily	As above, plus interfractional organ motion	Portal imaging (EPID) MB CBCT MV helical CT kV helical CT
Real-time correction	At short intervals during treatment delivery	As above, plus interfractional organ motion	Fluoroscopy Ultrasound

Current research in IGRT is described in the following sections according to the imaging modality used. This chapter will conclude with an overview of the specific problems addressed by this thesis.

2.1 Portal Imaging

The imaging system most commonly employed on a LINAC today is a portal image, which is a type of planar radiograph. In this system, the megavoltage therapeutic beam generated by the LINAC is used to create an image of the target area. This allows the projection of the patient

anatomy within the radiation field boundary to be visualised. The attenuated photons exiting the patient are detected using film or electronic portal imaging detectors (EPIDs).

Portal imaging has been important historically as part of the quality-assurance procedure in radiotherapy. Currently, most portal images are generated by film. They are taken either immediately before or after treatment on a weekly basis and compared with reference images such as simulation DRRs or radiographs. This image comparison process is mostly subjective, with room for individual interpretation [111]. Often, port films are evaluated off-line after treatment and corrective action is only taken at the next treatment fraction. Even when port films are evaluated prior to treatment delivery, patient motion during the long length of time taken to develop the films prohibit timely corrections from being made. The weekly evaluation of port films also means that errors in treatment set-up may not be corrected for several days.

Electronic portal imaging is becoming more prevalent at treatment centers. In contrast to film, these images can be generated in seconds and facilitate portal verification on a daily basis by radiation therapists, as well as on-line correction of positioning error [37, 38].

A number of reasons has prevented portal imaging from having a more prominent role in IGRT. One is the poor quality of the images themselves, due to the lack of contrast of human anatomy at the megavoltage photon energies used to generate portal images [12]. This has limited the use of portal imaging to comparing the locations of bony landmarks [21, 86] or implanted radiopaque fiducial markers [3, 110] for determining set-up error. In addition, the field of view of the images is very limited, since they are generated by the treatment portals. Furthermore, the lack of features in portal images has made quantitative comparisons of treatment and simulation anatomy using automatic image registration algorithms challenging [53]. Finally, planar radiographs are difficult to interpret with respect to 3D simulation data, especially when out-of-plane rotations are present.

2.2 Fluoroscopy

To date, one of the most advanced IGRT systems available, the Cyberknife® (Accuray Inc., Sunnyvale, CA) [2, 33], is based on fluoroscopic imaging. This system was designed for frameless radiosurgery of intracranial targets and has so far been installed at 68 locations world-wide with

over 20,000 patients treated. Radiosurgery differs from conventional radiotherapy in that a high dose of radiation is delivered to a small target volume in a single fraction, and generally without target margins. Therefore, very accurate positioning and immobilisation techniques are required. Traditionally, such levels of accuracy was only able to be achieved for intracranial targets, due to the small magnitude of organ motion inside the skull and the availability of stereotactic head frames which can be rigidly screwed to the cranium.

The Cyberknife® system allows the treatment of intracranial targets without the use of head frames. The system consists of a non-isocentric LINAC mounted on a 6 degree of freedom (DOF) robotic arm and an orthogonal pair of x-ray fluoroscopes positioned beside the couch. The X-ray cameras acquire real-time radiographs of the target region at repeated intervals during treatment (typically 20 to 40 seconds). These radiographs are automatically registered to simulation DRRs to localise the exact position of the target in manipulator coordinates. A control loop between the imaging system and the robotic arm allows the LINAC therapeutic beam to be precisely aligned with the target at start of each imaging cycle.

Compared to other IGRT systems in clinical use, the Cyberknife® is the only one capable of monitoring the target location at continuous intervals throughout the entire treatment procedure. Nevertheless, this system has disadvantages which has limited its general applicability. Firstly, fluoroscopic images have low spatial and contrast resolution of soft tissue. This means image guidance outside the cranium is only possible where targets are associated with bony landmarks. Thus far, the Cyberknife® has been used most extensively outside the cranium to treat spinal tumours. For other treatment sites, implantation of metal fiducials near the tumour is necessary. In these cases, image registration must be performed using limited information from the fiducial markers. Another disadvantage of the Cyberknife® system is that the 3D rigid transformation of patient movement must be estimated from two orthogonal 2D projection images, which is non-trivial [30].

2.3 CT

Currently, CT[1] imaging is the modality of choice for creating a model representation of the patient anatomy for planning, dosimetric, and verification purposes in radiotherapy. The main advantages of CT are that it is a 3D imaging modality, that it has good soft tissue contrast, and that electron density can be inferred from pixel intensity for dose calculation [82]. Performing an additional CT scan of the patient in the treatment room would facilitate detection of daily anatomical changes and positioning error through direct comparison of images from the same modality. Therefore, considerable effort has been made to introduce tomographic imaging capabilities into the treatment room. Technological approaches under investigation to achieve this goal are summarised in the following subsections.

2.3.1 MV Cone-Beam CT

The development of tomographic imaging capabilities inside the treatment room can be traced back to the work of Simpson *et al.* in the early 1980s [97]. Their approach involved mounting a single linear array of x-ray detectors on the rotating gantry of a LINAC. The 4MV therapeutic beam was collimated to a fan beam by existing collimator jaws and passed through the target. By rotating the LINAC gantry through 220° and obtaining projections of the target at different angles, a 2D tomographic image centered at the LINAC isocenter was able to be reconstructed using filtered-back-projection [43].

While this technique enabled visualisation of the patient in a single plane, obtaining multiple slices was problematic due to the slow speed of gantry rotation, and the need to translate the patient for each slice without introducing positioning error. This prompted the development of MV cone-beam CT (CBCT) on the LINAC [49, 79, 88, 94].

MV CBCT has been made possible by the development of suitable reconstruction algorithms [25] in the mid-1980s, and the more recent advances in portal imaging technology. The process of obtaining a CBCT using a LINAC is similar to the technique used by Simpson *et al.* described previously for obtaining a 2D image. In CBCT, a 2D detector array, such as a standard EPID

[1]Unless indicated otherwise, CT in this thesis refers to kilovoltage (kV) helical computed tomography.

for portal imaging, is used to collect 2D projections of the target. This allows a 3D image to be reconstructed from data collected in a single gantry revolution.

MV CBCT has a number of appealing features. No additional hardware is required for imaging, and the image is obtained exactly in the LINAC coordinate system. Moreover, the voxel intensity values directly correspond to the material electron density at the treatment beam energy, meaning no approximate conversions are necessary as with kV CT images for dose calculation.

In addition, cone-beam reconstruction algorithms can also be used to reconstruct the 3D dose delivered to the patient if the exit dose is monitored by portal imaging [83]. The dose distribution may then be superimposed onto the planning CT to provide thorough treatment verification. The ability to monitor delivered dose distributions could potentially allow modifications to the dose plan to be made for future treatment fractions to account for deficiencies. The application of feedback to the radiotherapy process, or adaptive radiotherapy (ART), is a relatively new concept which is undergoing active research [112].

However, MV CBCT has disadvantages as well. The low tissue contrast at MV energies and low-efficiency of current flat-panel x-ray detectors means that high doses are necessary to achieve an acceptable signal to noise ratio (SNR) in MV CBCT images [35]. The size of the flat-panel detectors currently available, and restrictions in the cone beam angle due to the LINAC collimator also limits the size of MV CBCT images to roughly $25cm$ in diameter and length [48]. Thus far, the clinical use of MV CBCT for image-guidance has not been reported. Nevertheless, recent work [88] suggest that low-dose MV CBCT of sufficient quality could be generated for online alignment of bony anatomy and air cavities to planning CT.

2.3.2 kV Cone-Beam CT

The addition of a diagnostic x-ray source to the LINAC to generate kV radiographs of the patient in the treatment position has been reported since the 1980s [8]. The original motivation was the obvious advantage of improved image quality over portal imaging, the ability to image the patient during irradiation, and the fact that the dose delivered in a kV exposure is significantly lower than a MV image, which allows more frequent imaging and additional views of the anatomy to

be obtained.

The potential for tomographic imaging using an integrated kV imaging system was first reported by Jaffray *et al.* [49]. In this system, a kV x-ray tube and fluoroscopic imager were rigidly fixed to a LINAC so that the imaging plane was 90° to the treatment beam axis. With continued improvements to flat-panel x-ray detector technology, the use of kV CBCT in clinical practice is now becoming a reality. Currently, all 3 major LINAC manufacturers are offering integrated kV CBCT systems [Elekta Synergy® (Elekta, Sweden), Varian On-board Imager™ (Varian, Palo Alto, CA), and Siemens Artiste™ (Siemens, Concord, CA)].

In [109], van Herk *et al.* described their clinical experience in using kV CBCT images to correct set-up error in prostate, head and neck, and lung cancer patients. Set-up error was determined by registering bony anatomy in the kV CBCT to the planning CT scan. Comparison of CBCT data and setup error derived from portal imaging showed a systematic error of $1mm$, and site-dependant standard deviations of $1-3mm$, which was mainly attributed to observer variation in portal image analysis. Recently, Létourneau *et al.* [63] implanted radiopaque markers made of high-winding coils into the prostate of 8 patients. Set-up error was determined by registering the locations of these fiducials in kV CBCT and planning CT scans. In addition, intrafractional motion was monitored by tracking the marker locations in 2D kV radiographs taken using the same imaging system every 30s throughout the treatment procedure. The residual set-up error after CBCT correction was determined using a second CBCT and was within a standard deviation of $1.5mm$. Intrafractional motion of the prostate was found to have a standard deviation of $0.9mm$.

Despite its advantages, a number of challenges exist in kV CBCT systems. Currently, 2D flat-panel x-ray detectors still suffer from limited dynamic range, lag, ghosting, and the effects of high x-ray scatter [48]. Motion artifacts also affect kV CBCT images due to its long acquisition time ($\sim 30-120s$). The need to register kV CBCT images with the LINAC coordinates through calibration and the need to maintain geometric stability of the system must also be considered [96].

2.3.3 MV Helical CT

The integration of a LINAC and helical CT scanner, or "tomotherapy", was first proposed by Mackie *et al.* in 1993 [66]. In tomotherapy, a MV radiation emitting device is placed in a conventional CT-like ring gantry configuration. Therapeutic radiation is delivered using a rotating fan-beam modulated by a collimator system while the patient is moved through the gantry in the longitudinal direction on a couch. Radiation is delivered in slices, hence the prefix "tomo".

Unlike a traditional isocentric LINAC, tomotherapy units are not able to deliver radiation to patients from non-coplanar directions, hence limiting their capability in carrying out treatment plans where this is necessary. However, their obvious advantage is that of an integrated imaging system. A conventional CT detector system is mounted on the gantry directly opposite to the x-ray source. This enables volumetric MV CT images of the patient at the time of treatment delivery to be acquired for set-up verification. In addition, during irradiation, the exit dose from the patient can be monitored by the CT detectors and used in a back-projection process to compute the dose distribution that is delivered to the patient [52]. This information can then be compared with the planned dose distribution to facilitate an adaptive radiotherapy process.

Tomotherapy units are currently marketed by Tomotherapy Inc. (Madison, WI). Clinical experience with this device is growing as its usage becomes more widespread. In [59], Langen *et al.* investigated the use of MV CT images from a tomotherapy unit to correct for daily prostate motion. The use of prostate fiducial markers were found to be necessary for accurate registration of the low-contrast MV CTs to the kV planning CT. In [90], Ramsey *et al.* used MV CT to position lung cancer patients daily. The MV CT images were of sufficient quality to allow identification of the GTV and use of automatic voxel intensity based methods for registration with planning CT. The same group have also reported the use of tomotherapy for the treatment of spinal lesions [69].

As with all MV imaging systems, MV helical CT from the tomotherapy unit suffer from poor contrast resolution and increased noise and dose to the patient due to the low quantum efficiency of the detectors. Compared to EPIDs, however, the detectors used in tomotherapy systems are much more efficient [5]. Therefore, the CT image quality from tomotherapy systems can be expected to be better than MV CBCT.

2.3.4 kV Helical CT

Images generated from conventional kV helical CT scanners are still the gold standard in terms contrast, noise, efficiency and dynamic range when compared to other CT technologies. Therefore, numerous investigators in the past decade have attempted to introduce diagnostic CT scanners into the treatment room [17, 55, 107]. These systems consist of a CT scanner placed directly opposite to a LINAC, and a common shared couch in between. The gantry of the LINAC and CT scanner are coaxial so that the CT volume shares the same coordinate system as the LINAC. The common couch can be rotated 180° from a treatment position to an imaging position. To minimise the amount of couch movement, the entire CT gantry is translated on rails during imaging.

Currently, these "CT-on-rails" systems are commercially available [EXaCT Targeting^{TM} (Varian) and PRIMATOM^{TM} (Siemens)]. A number of North American and Japanese centers are gaining experience in their use. In [19], Court *et al.* reported on the mechanical and alignment uncertainties on an EXaCT Targeting^{TM} system installed at the M. D. Anderson Cancer Center, Houston, TX. The precision of the system was predicted to be less than $0.7mm$ (1 standard deviation) in any orthogonal direction. The same group has proposed a protocol for deforming the treatment beam's intensity distribution to account for daily anatomic changes observed in treatment CT scans [77]. Zhang *et al.* at the same cancer center used repeat CT scans to compare set-up error in different regions of interest in head and neck patients with the use of immobilisation devices [114]. In [84], the PRIMATOM^{TM} system was used to perform CT guided repositioning of brain patients. Compared to target localization results achieved using a fixed stereotactic head frame, an accuracy on the order of $1mm$ was found for this technique.

The major advantage of CT-on-rails systems is that they can leverage all the development invested in conventional CT technology over the past 20 years, leading to unparalleled imaging quality. However, the cost of installing a CT gantry inside the treatment room is currently prohibitive for most hospitals. The need for multiple translations and rotations of the patient between imaging and treatment also reduces patient throughput and introduces additional sources of error.

2.4 Ultrasound

Ultrasound is an inexpensive, highly flexible, and high resolution imaging modality that can easily be adapted for use in the radiotherapy treatment room. It offers the advantages of having good soft-tissue contrast, ability to acquire images in real-time, and being noninvasive. These qualities have spurred the recent development of ultrasound-based IGRT systems.

Currently, a number of ultrasound-based target localisation systems are available commercially. These include the B-mode acquisition and targeting system (BAT) (NOMOS, Sewickley, PA), SonArray (Varian), and Restitu (Resonant Medical, Montreal, Canada). The use of this technology was first reported by Lattanzi *et al.* [61], who investigated daily positioning of prostate patients with the BAT. Presently, the most widely used method for daily prostate targeting is ultrasound [54]. Besides the prostate, the use of ultrasound-guidance for abdominal tumours has also been investigated [32]. In the subsections to follow, current existing ultrasound-based patient positioning systems will be described, as well as clinical experience in their use.

2.4.1 BAT

The BAT was the first ultrasound-based IGRT system introduced onto the market and remains the most popular system in clinical use. It consists of an ultrasound machine docked to the LINAC gantry. Before the commencement of daily treatment, 2D ultrasound images of the patient in the treatment position are acquired by the radiation therapist, and are displayed in real-time. The ultrasound probe position is tracked by a position-sensing arm which is calibrated to the LINAC isocenter. This allows the ultrasound image location relative to the LINAC isocenter, and hence the planning CT scan, to be known.

To facilitate set-up verification, manually segmented contours from CT during treatment planning are overlaid on top of the corresponding 2D ultrasound view. A touch pad on the display screen allows the CT contours to be moved so that they align as closely as possible with features seen in ultrasound. By sweeping the ultrasound probe, additional views of the anatomy can be captured and compared to CT contours. When the therapist is satisfied with the alignment of features, the couch movement required to bring the patient into the correct position is calculated

by the BAT software. The entire process of patient positioning, imaging, and alignment can be accomplished in 3 to 7 minutes [54], enabling daily on-line verification of patient position.

Extensive experience in using the BAT has been developed over the past few years. Initial clinical investigation has focused on evaluating its use for correcting prostate set-up errors [45, 78, 95, 106]. A review of prostate shifts from initial set-up marks reported in 9 different studies can be found in [54]. Authors generally gave favorable reports on the performance of the system, and most concluded that BAT localisation was clinically feasible and useful. However, the range of set-up corrections varies considerably between studies, and some reported non-trivial systematic deviations in BAT determined shifts [78, 106]. It is not known whether these discrepancies are due to inherent problems with the BAT system, uncertainties with ultrasound imaging, differences in bladder and bowel preparation, differences in immobilisation, or operator induced errors.

Relatively few studies have compared the accuracy of BAT patient positioning with another image localisation technique. In [60], Lattanzi *et al.* compared prostate shifts determined using BAT and repeat CT scanning and concluded the two systems to be functionally equivalent. Nevertheless, discrepancies of up to $7mm$ were seen in some patients. Dong *et al.* [23] compared BAT to prostate localisation using a CT-on-rails system. The mean systematic differences were relatively small, but standard deviations indicated large discrepancies in individual alignments. Comparing BAT to alignments based on portal imaging and implanted fiducials in the prostate, Langen *et al.* [58] and Van den Heuvel *et al.* [108] reported systematic mean differences of $0.2 - 2.7mm$ in each orthogonal direction, and larger random differences of $3.1 - 5.7mm$.

Recently, a number of studies have been performed in an attempt to resolve the measurable discrepancies in the BAT system as detailed above. Ultrasound image quality is an issue raised by a number of investigators. Chandra *et al.* [16] found 95% of transabdominal prostate ultrasound images to be of adequate quality for alignment, while this was the case for 83%, 73%, and 66% of the images in the studies of Morr *et al.* [78], Serago *et al.* [95], and Langen *et al.* [58].

In addition, uncertainties in manual contouring of anatomical features on CT scans directly translate to a systematic BAT positioning error. The prostate apex is known to be a difficult area to define on CT scans. A typical standard deviation of $4mm$ has been reported in the contouring of the prostate base and apex [50].

Inter- and intraoperator variability in performing image alignment has also been studied. Trichter *et al.* [106] and Serago *et al.* [95] found repeat BAT localisation peformed by the same user yielded results within $3-4mm$. Fuss *et al.* [31] compared alignments performed by a median of 5 users and found differences of less than $4.4mm$ in each orthogonal direction. In [16], Chandra *et al.* reported a $> 5mm$ difference between alignments performed by a therapist and a physician in 3% of cases. Other authors, however, found significant interoperator variability. Langen *et al.* [58] reported an average range in alignment difference between 8 users of $7mm$, $7mm$, and $5mm$ in the anterior-posterior, superior-inferior, and lateral directions, respectively. Enke *et al.* [24] found interoperator differences in using the BAT to be as much as $11.56mm \pm 3.7mm$.

Differences in the appearance of anatomical structures between CT and ultrasound images have been suggested as a source of error in BAT localisation and a contributing factor in the variability of manual image alignment results [58]. Prostate definition is known to vary between CT and ultrasound [80, 92]. The prostate volume measured from CT have been found to be consistently larger than ultrasound by a factor of approximately 1.5 [41].

Another source of error in the BAT system is that only translations are used to align CT contours and ultrasound images. In practice, differences in patient orientation between the simulation and treatment sessions are also possible. Attempting to register planar 2D images with the presence of out-of-plane rotations can lead to additional registration error.

The possibility that applied ultrasound probe pressure during imaging may displace underlying tissue has been investigated. In [95], ultrasound probe pressure was found to displace the prostate by an average of $3.1mm$, mainly in the posterior-inferior direction. This is in agreement with the work of Artignan *et al.* [4], who showed that by applying the probe pressure necessary for generating good quality images, the prostate was displaced by an average of $3mm$.

A potential source of systematic error in the BAT system is the calibration of the ultrasound probe position with respect to the LINAC isocenter. A quality assurance phantom [54] is used for maintaining system calibration. This phantom contains an spherical object with both CT and ultrasound contrast surrounded by a tissue-equivalent material. CT images of the phantom are taken with the maximum axial resolution possible. To detect system abnormalities, the phantom is positioned on the couch using alignment lasers and guide marks. Its position is then refined

by aligning its CT contours with ultrasound scans from the BAT system as usual. The recommendation for daily quality assurance is to accept a shift of less than $2mm$ when aligning the phantom.

Although early reviews of the BAT system were generally positive, recent studies have highlighted factors which may be detrimental to the accuracy of the system, and promote further research in this area. User variability in prostate localisation using the BAT is acknowledged as a real phenomenon, and the need for physicians to closely supervise training of the radiation therapist in using the BAT is recognised. The measurable differences between the BAT and other image-guidance techniques for positioning prostate patients suggest that appropriate margins for positioning uncertainty remain necessary.

2.4.2 SonArray

The SonArray system was developed at the University of Florida's McKnight Brain Institute in collaboration with Zmed (Holliston, MA), now a subsidiary of Varian. It is very similar to the BAT in functionality, and prompted NOMOS to file a patent lawsuit against Zmed. Zmed emerged victorious from the trial, demonstrating that their system was more effective in targeting tumours than the BAT. Unfortunately, there are no publications in the literature comparing the two systems.

To position patients for treatment using the SonArray system, freehand 3D ultrasound data of the treatment anatomy is acquired. The operator sweeps the ultrasound probe over the anatomical area of interest while the probe position is tracked using an array of infrared light emitting diodes (IREDs) rigidly attached to the probe. The IRED positions are determined by CCD cameras calibrated to the LINAC isocenter. This enables the 2D ultrasound slices to be reconstructed into a 3D volume and its position relative to the LINAC isocenter to be known.

To perform patient alignment, orthogonal planes of the reconstructed ultrasound volume is displayed, along with corresponding simulation CT contours at the same location. The radiation therapist manually shifts the CT contours so that they are in alignment with ultrasound features, much like the BAT system. Thus, only 3 DOF image registration is performed by the SonArray as

well. The major difference between the two systems is that the BAT does not explicitly reconstruct 2D ultrasound slices into a volume, but relies on the therapist to obtain sufficiently varied views of the anatomy to gain a 3D perspective.

The SonArray was approved for marketing by the FDA in 2000, but so far reports of its use are limited in the literature. A number of papers, however, detail the technical aspects of implementing the system. In [11], the probe calibration technique used to find the rigid-body transformation from ultrasound probe to ultrasound image is presented. The accuracy of optically tracked ultrasound in localising spherical targets inside a phantom was measured using a CT gold standard by Tomé *et al.* to be under $1mm$ in each orthogonal direction [101]. In addition, the system accuracy in detecting artificially induced shifts in a prostate phantom was found to be within $1mm$ in each axis.

The only existing report of clinical testing of the SonArray system is by Meeks *et al.* [74]. Unlike the BAT system, which was initially restricted in use to prostate cancer, a variety of treatment sites were considered using the SonArray at the outset. Meeks *et al.* reported on ultrasound-guided radiosurgery of 16 patients in sites including the liver, paravertebral/t-spine, sacral, lower neck, chest wall, hip, iliopsoas muscle, and arm. The average target misalignments detected by the SonArray were $4.8mm$, $3.6mm$, and $2.1mm$ in the anterior-posterior, lateral, and superior-inferior directions.

Unfortunately, no comparison of the accuracy of the SonArray to another image-guidance technique has ever been performed. The phantom study by Tomé *et al.* does not take into account a variety of error sources when data is acquired from a real patient, as already pointed out by a number of researchers using the BAT [58, 108]. These include user interpretation and registration of the ultrasound images and CT contours and displacement of the target due to ultrasound probe pressure.

2.4.3 Restitu

Very recently, an ultrasound patient positioning system which acquires ultrasound images during the simulation session as well as treatment was introduced by Resonant Medical (Montreal,

Canada). The freehand 3D ultrasound image at simulation serves as a reference for the patient anatomy used for treatment planning. This reference image is then compared with subsequent ultrasound images taken immediately prior to treatment in order to detect set-up error and day-to-day changes in the anatomy.

The advantage of the Restitu system is that patient alignment is achieved through intramodality image registration between ultrasound and ultrasound, rather than intermodality registration between CT and ultrasound, like the BAT and SonArray. This removes the uncertainties associated with comparing anatomy in different image modalities, one factor which has been cited as the cause for user variability of the BAT.

To perform patient positioning using the Restitu, a simulation ultrasound is first taken within a minute of the simulation CT while the patient remains in the same position. An optically tracked ultrasound probe calibrated to the simulation room lasers is swept across the region of interest on the patient's skin to collect a freehand 3D ultrasound of relevant anatomy.

To reposition the patient on the day of treatment, another freehand 3D ultrasound is acquired. This time, the optically tracked probe is calibrated to the LINAC isocenter. The treatment and simulation ultrasound scans are then registered using manually segmented contours of anatomical features from the two data sets. For prostate patients, the prostate and bladder are contoured. The simulation ultrasound can be contoured off-line, whereas the treatment ultrasound must be contoured by the therapist during the positioning procedure. To aid the segmentation process, extracted contours on one slice can be propagated automatically through other slices in the data set. The 6 DOF (3 translations and 3 rotations) registration of treatment and simulation contours is performed automatically using the iterative closest point (ICP) algorithm [7]. From the rigid-body transformation results of the registration, the target location with respect to the LINAC can be determined, and the couch shift necessary to bring the patient into correct treatment position is calculated.

It should be noted that the technical details of the Restitu system are not found in the scientific literature. The description above has been gleaned from promotional material and a presentation at the BCCA by the Resonant Medical chief executive officer. One conference abstract has been published by Resonant Medical comparing the Restitu and the BAT for positioning prostate

patients [20]. A mean difference of 0.9 (C.I.[2] 0.5, 1.3) *mm*, 0.1 (C.I. -0.5, 0.7) *mm*, and 6.0 (C.I¿ 5.4, 6.6) *mm* in orthogonal directions was found. In addition, when Restitu results were compared to repeat CT scanning, the mean differences were 0.2 (C.I. -0.4, 0.8) *mm*, -0.3 (C.I. -0.9, 0.3) *mm*, and 0.1 (C.I. -0.5, 0.7) *mm* in the same directions. These results suggest that alignments using the Resonant system are more accurate than the BAT when using repeat CT scanning as the gold standard.

2.5 Problem Statement

The previous sections have shown that a variety of approaches exist for implementing IGRT in clinical practice. All of these approaches have their strengths and weaknesses, and currently, no single one can meet the requirements of the ideal IGRT system described at the beginning of this chapter. Therefore, all the techniques described should have their own niche role in IGRT for the foreseeable future.

Ultrasound imaging, in particular, has a unique set of advantages over other modalities as the imaging technology in an IGRT system. This includes being:

- inexpensive.
- able to acquire images in real-time.
- non-invasive and non-harmful to the patient.
- able to image soft tissue.
- able to acquire 3D images.

Ultrasound's ability to capture organ motion in real-time means that it can be potentially used not only to verify patient positioning at the start of every treatment, but also to monitor organ motion during dose delivery. Recently, Hsu *et al.* [44] showed that it is possible to track phantom motion with B-mode ultrasound acquired by a probe mounted just outside the radiation field,

[2]C.I. = confidence interval

while a LINAC was in operation. In addition, the presence of the transducer on the phantom surface caused only a 2.6% change to the dose distribution inside the phantom volume. It is worthwhile to note that this approach would also negate the effects of ultrasound probe pressure on tissue displacement, as the probe remains in place for the duration of treatment.

Advancements in ultrasound imaging technology continues to develop. Dedicated 3D ultrasound probes are now able achieve an acquisition rate of 33 volumes per second, enabling real-time 3D imaging, or '4D' ultrasound[3] to become possible. In the future, probes with 2D array transducers could achieve even higher acquisition rates [99]. With 4D ultrasound imaging, it may be possible to monitor 3D intrafractional organ motion occurring during radiation delivery and correct for these in real-time with the approach of Hsu *et al.*. No other imaging modality can currently offer this capability. Therefore, ultrasound-guided patient positioning systems can be expected to play an important role in future radiotherapy applications.

In this thesis, a novel 3D ultrasound-based patient positioning system for radiotherapy is proposed. It is also shown that such a system can be practically implemented. To the author's knowledge, this is the only system to date which leverages the latest advancements in 3D ultrasound technology. Current existing systems such as the BAT are based on acquiring multiple 2D views of the anatomy. In contrast, the proposed system will utilise dedicated 3D probes to acquire data. This has a number of advantages, including:

- minimising the number of image acquisitions (one *cf.* multiple 2D images).
- ease of use (removes the need to manually sweep a 2D probe).
- faster 3D image acquisition.
- improved accuracy in 3D image reconstruction.

Another important advantage of the proposed system is its reduced reliance on operator input. This alleviates the subjective nature of patient alignment with current systems. In particular, the need for the error-prone processes of manual image registration and contouring of CT or ultrasound

[3] 4D in this case refers to 3 spatial dimensions, plus 1 time dimension.

images are not required. Instead, automatic pixel-intensity based image registration will be used to compare patient treatment and simulation anatomy.

The next chapter of this thesis will present the proposed 3D ultrasound patient positioning system in detail. The envisaged treatment protocol, as well as a comparison with existing ultrasound localisation systems in a common mathematical framework will be given. The accuracy of two key components of the proposed methods are then evaluated in Chapter 4 to aid error analysis of the entire system. Finally, in Chapter 5, the complete system is used to position a phantom for irradiation inside a LINAC. Using a novel validation method, the entire radiation therapy process, from simulation to treatment delivery, is simulated to verify the overall accuracy of treatment using the proposed patient positioning system. No previous work on image-guidance systems for radiotherapy has attempted to show this type of validation.

Chapter 3

System Overview

In this chapter, the hardware components of the proposed ultrasound patient positioning system will first be described. This will be followed by a summary of the envisaged radiotherapy treatment protocol when using the system. The process of localising the treatment isocenter inside the treatment room will then be described from a mathematical point of view using coordinate transformations. Finally, the method used by the proposed system for patient positioning will be compared to existing systems within this mathematical framework.

3.1 System Hardware

The basis of an ultrasound patient localisation system consists of an ultrasound imaging system coupled with an external position tracking device capable of localising the ultrasound probe in 3D. For the proposed system, the GE Voluson 730 Expert ultrasound (GE Healthcare, Waukesha, WI) is used for imaging, while the OPTOTRAK 3020 positioning system (NDI, Waterloo, Canada) is used for the purpose of probe localisation. These two components are described in further detail in the following subsections. The process of collecting data from both the ultrasound and OPTOTRAK is also presented.

3.1.1 Voluson 730

The GE Voluson 730 Expert ultrasound offers automatic 3D imaging capabilities with dedicated 3D probes. These probes are different from conventional 2D ultrasound probes in that they contain an internal mechanism which can physically pivot the transducer array through a predefined set of angles, as illustrated in Figure 3.1(a). This allows an entire series of 2D image slices in a fan-like

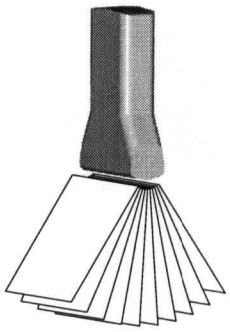

(a) Voluson 730 volume acquisition

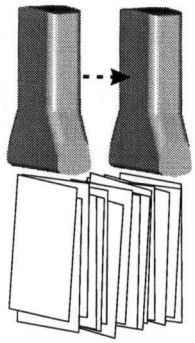

(b) Freehand volume acquisition

Figure 3.1: Volumetric imaging with a dedicated 3D probe (a), and with the freehand method (b). A fan-like pattern of 2D slices are collected automatically by the dedicated 3D probe while it remains still over the patient. In contrast, the probe must be manually swept over the patient in the freehand technique, and the slice locations are unconstrained. In order to reconstruct a 3D volume of data on a regular cubic lattice, the ultrasound data from the series of 2D slices collected is resampled. This means that the spatial resolution of the reconstructed volume will be non-uniform in both cases (a) and (b). This non-uniformity is the same for all reconstructed 3D volumes acquired using the Voluson 730, with decreasing resolution further away from the transducer. In contrast, the spatial resolution will be different for every reconstructed volume acquired using the freehand approach, since the relative positions of the 2D slices will not be the same in each acquisition.

pattern to be acquired while the probe remains stationary over the patient. By collecting multiple 2D images at different positions, a 3D volume of data can be constructed [26].

The automatic 3D ultrasound imaging[1] capabilities of the Voluson 730 represent a significant advance over freehand 3D ultrasound imaging[2] [91]. In this technique, a conventional 2D probe is manually swept over the surface of the patient in order to obtain multiple 2D views of the anatomy, as shown in Figure 3.1(b). No restrictions are placed on the probe's movement and the relative positions of the 2D slices are determined by tracking the probe using a position sensor.

One advantage of using dedicated 3D probes over freehand imaging is that the image acquisition procedure is much easier for the sonographer. As in conventional 2D ultrasound imaging, the probe is kept still on the patient as volumetric data is collected using dedicated 3D probes. In contrast, in freehand imaging, some additional skill is required on the part of the operator to constantly

[1]Hereafter simply referred to as '3D ultrasound'.
[2]Hereafter simply referred to as 'freehand ultrasound'.

maintain adequate probe contact with the patient's skin as it is swept over a region of interest, while at the same time avoiding significant deformation of the underlying tissue. Non-uniform tissue deformation due to varying probe pressure is a significant source of artifacts in freehand imaging [105].

Another advantage of 3D image acquisition using the Voluson 730 is that 2D slices are collected at known predefined positions, since the transducer array is mechanically swept. In contrast, the slice positions in freehand acquisition are unrestricted, and must be determined using additional probe tracking data and knowledge of the image location with respect to the probe, which must be found through calibration. In addition, data synchronisation (the matching of image frames to positional tracking information) is required. Therefore, the calculated position of every slice of data collected during freehand acquisition will be subject to tracking, probe calibration, and data synchronisation errors, which can reduce the accuracy of the reconstructed volume [104].

Finally, automatic 3D acquisition using dedicated probes also offer the possibility of real-time 3D, or 4D imaging. Indeed, the Voluson 730 is capable of acquiring up to 25 volume scans per second, depending on the image dimensions, number of focal points, and quality settings.

3.1.2 OPTOTRAK

The OPTOTRAK 3020 position sensor, shown in Figure 3.2, is a flexible and highly accurate instrument used in numerous and diverse fields including human motion studies, robotics, surgery and aeronautics. It consists of three one-dimensional CCDs paired with three lens cells mounted in a 1.1 m long stabilized bar. Within each of the three lens cells, infrared light from an OPTOTRAK IRED marker is directed onto a CCD and measured. Using the three measurements and known geometries of the CCDs, the 3D location of a marker is determined in real-time through stereo vision. The marker position is given relative to a predefined global OPTOTRAK coordinate system, the origin of which lies at the middle CCD center. At a distance of 2.5 meters, the OPTOTRAK has an RMS error of $0.1mm$ in the x and y (lateral) directions, and $0.15mm$ in the z (depth) direction [47].

By activating each IRED in sequence, the system can track multiple markers and identify each

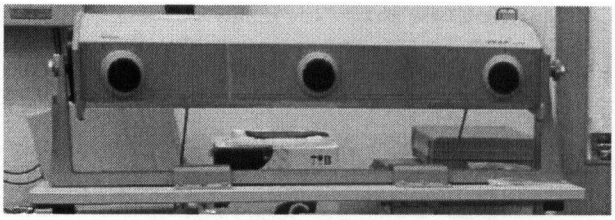

(a) OPTOTRAK 3020

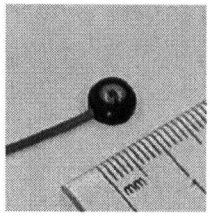

(b) IRED marker

Figure 3.2: The OPTOTRAK 3020 position sensor and an IRED marker.

one uniquely, even if it is out view. Multiple markers (three or more) placed on a rigid-body can be used to define a local coordinate system for that object. When such rigid-body configurations are tracked by OPTOTRAK, a 6 parameter result giving the object's 3D location and orientation is returned.

To make tracking of ultrasound probes possible in the proposed system, IREDs must be mounted rigidly to the probe. To avoid permanently attaching the markers and causing damage, mounting brackets were constructed out of sheet metal and fitted to the 3D probes of the Voluson 730, as shown in Figure 3.3. IRED markers were then fixed to the surface of the mounting bracket with hot glue. Care was taken in the construction of the mounting bracket to ensure that it remained as rigid as possible with the probe. Thin rubber padding on the probe surface was used to increase friction and produce a secure fit for the bracket.

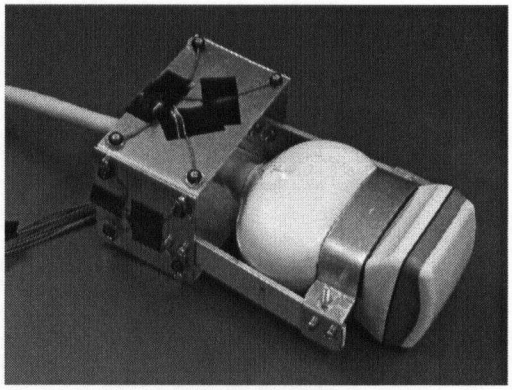

Figure 3.3: The RSP5-12 probe of the Voluson 730 fitted with a mounting bracket attached with IRED markers. The IRED locations are measured by OPTOTRAK and enables the probe location and orientation to be determined.

3.1.3 Combined System

To allow the ultrasound probe position to be tracked during image acquisition, the OPTOTRAK and Voluson 730 are controlled by a PC, as shown in Figure 3.4. The host PC is connected to the OPTOTRAK control unit by a coaxial cable through a peripheral component interconnect (PCI) interface. An application programming interface (API) is provided by NDI to facilitate communication between the PC and the OPTOTRAK system.

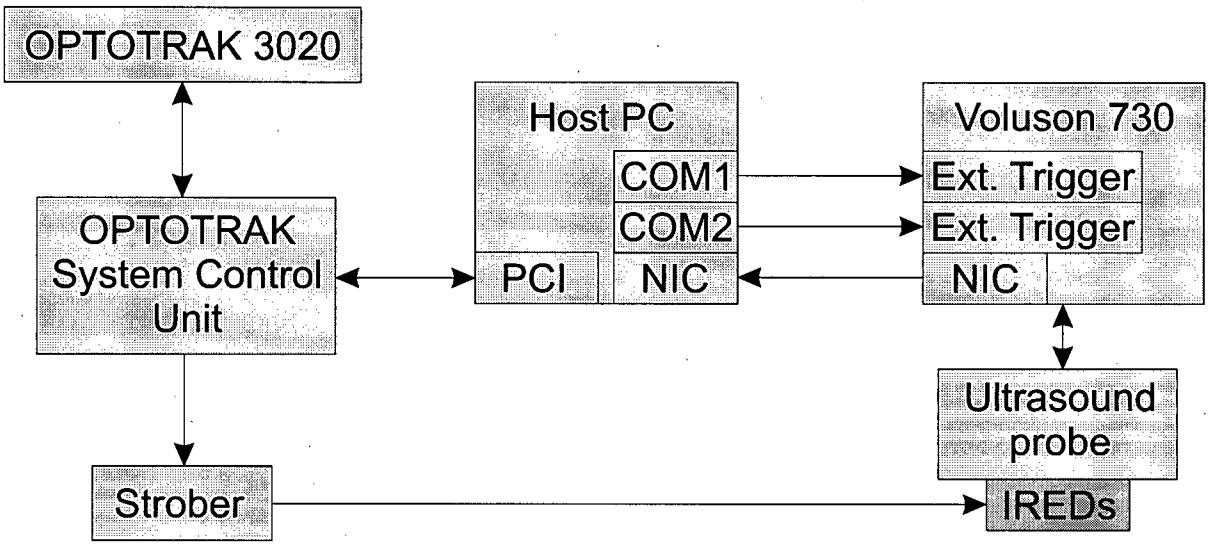

Figure 3.4: Control of both the OPTOTRAK 3020 and the Voluson 730 using a host PC. The arrows indicate the direction of data flow. The OPTOTRAK control unit is connected to the PC by a PCI interface. Image acquisition and transfer on the Voluson 730 is initiated by two external trigger inputs (ext. trigger). These control signals are generated using the PC's serial ports (COM1 and COM2). Ultrasound images are transferred from the Voluson 730 to the PC through network interface cards (NICs) using the DICOM protocol.

Image acquisition on the Voluson 730 is remotely controlled by the host PC using an external trigger input. The acquired image is transferred to the PC via an ethernet cable using the digital imaging and communications in medicine (DICOM) protocol. Image transfer is initiated by the host using another external trigger.

The control signals for the two triggers are generated by two serial ports on the host PC. By writing the appropriate output to the two serial ports, and issuing the correct API command

to the OPTOTRAK, both ultrasound image acquisition and OPTOTRAK measurement of the probe position can be initiated at approximately the same time. Since the probe position remains stationary during automatic 3D acquisition, there is no need to accurately synchronise the start of imaging and OPTOTRAK collection.

3.2 Treatment Protocol

The envisaged radiotherapy treatment protocol using the proposed ultrasound patient positioning system is as follows:

1. During CT simulation, IRED markers are placed on the patient's skin before the commencement of the CT scan in addition to BBs and skin markings. The IREDs appear in the CT image as fiducial markers.

2. Immediately after the CT scanning, simulation ultrasound volumes of relevant anatomy near the target isocenter are acquired. During this procedure, both the ultrasound probe and patient are tracked by the OPTOTRAK using the IREDs attached to the probe and patient.

3. During treatment planning, the simulation CT and ultrasound volumes are registered off-line. This allows the treatment plan, defined in CT coordinates, to be transferred into simulation ultrasound coordinates.

4. In each treatment session, the patient is set up as usual using skin marks and alignment lasers.

5. To verify correct patient positioning, a treatment ultrasound volume of the target anatomy is taken at approximately the same viewpoint as the simulation ultrasound. The probe position is measured with respect to the LINAC coordinate system by OPTOTRAK.

6. The treatment ultrasound is automatically registered to the simulation ultrasound, allowing the dose plan geometry and planned isocenter location to be transformed into the LINAC coordinate system. This gives a full 6 DOF description (3 translations and 3 rotations) of the target position with respect to the LINAC isocenter.

7. Differences between the planned isocenter location and the actual LINAC isocenter is determined, as well as differences in the planned and actual orientation of the patient.

8. Action is taken to correct for the detected patient positioning error before irradiation. This could be accomplished using couch shifts to correct for translational error, and couch, collimator, and gantry rotations to correct for orientation error [113].

To describe the process of the proposed ultrasound localisation scheme in full, a mathematical treatment of the patient positioning process is given in the next section.

3.3 System Description Using a Mathematical Framework

To begin, the concepts of coordinate systems and homogeneous transformation matrices are reviewed.

3.3.1 Mathematical Preliminaries

In this thesis, vectors will be defined as displacements in 3D space. Any vector can be expressed as a linear combination of three linear independent vectors which forms a basis or frame. For example, the canonical frame $\underline{C}$ can be defined by the 3×3 matrix

$$\underline{C} \equiv \begin{bmatrix} \underline{i} & \underline{j} & \underline{k} \end{bmatrix} = \begin{bmatrix} 1 & 0 & 0 \\ 0 & 1 & 0 \\ 0 & 0 & 1 \end{bmatrix}. \tag{3.1}$$

A vector $\underline{x}$ can then be expressed in the canonical frame by

$$\underline{x} = a_x\underline{i} + b_x\underline{j} + c_x\underline{k} = \begin{bmatrix} \underline{i} & \underline{j} & \underline{k} \end{bmatrix} \begin{bmatrix} a_x \\ b_x \\ c_x \end{bmatrix} = \underline{C}x \tag{3.2}$$

where $x \equiv [a_x \ b_x \ c_x]^T$ is the coordinates of $\underset{\sim}{x}$ in $\underline{C}$.

A coordinate system consists of a fixed point $\underset{\sim}{o}$ called the origin, and a reference frame such as the canonical frame $\underline{C}$. It allows other points to be defined as displacements from the origin using vectors in the reference frame. For example, point $\underset{\sim}{x}$ may be defined in the coordinate system $\{\underset{\sim}{o}, \underline{C}\}$ by

$$\underset{\sim}{x} = \underset{\sim}{o} + \underline{C}x \tag{3.3}$$

where x is the coordinates of $\underset{\sim}{x}$ in $\{\underset{\sim}{o}, \underline{C}\}$.

There are an infinite number of choices for frames[3] as well as origins, and thus there are an infinite number of possible coordinate systems. The same point may be expressed in different coordinate systems:

$$\underset{\sim}{x} = \underset{\sim}{o}_0 + \underline{C}_0{}^0x = \underset{\sim}{o}_1 + \underline{C}_1{}^1x \tag{3.4}$$

where ${}^0x$ is the coordinates of $\underset{\sim}{x}$ in $\{\underset{\sim}{o}_0, \underline{C}_0\}$ and ${}^1x$ is the coordinates of $\underset{\sim}{x}$ in $\{\underset{\sim}{o}_1, \underline{C}_1\}$. The vectors and origins of one coordinate system can be written with respect to another:

$$\begin{aligned} \underline{C}_1 &= \underline{C}_0{}^0C_1 \\ \underset{\sim}{o}_1 &= \underset{\sim}{o}_0 + \underline{C}_0{}^0d_1 \end{aligned} \tag{3.5}$$

where the columns of ${}^0C_1$ are the coordinates of the frame vectors $\underline{C}_1$ in frame $\underline{C}_0$. For right-handed orthonormal frames, this matrix represents a 3D rotation about an arbitrary axis. The entries in ${}^0d_1$ are the coordinates of the vector $\underset{\sim}{o}_1 - \underset{\sim}{o}_0$ (displacement between the two origins) in $\underline{C}_0$. From Equation 3.4,

$$\begin{aligned} \underline{C}_0{}^0x &= (\underset{\sim}{o}_1 - \underset{\sim}{o}_0) + \underline{C}_1{}^1x \\ &= \underline{C}_0{}^0d_1 + \underline{C}_0{}^0C_1{}^1x \end{aligned} \tag{3.6}$$

and therefore, the coordinate system change can be expressed as

$${}^0x = {}^0d_1 + {}^0C_1{}^1x. \tag{3.7}$$

[3]In this thesis, only right-handed orthonormal frames will be considered.

This can be rewritten in matrix form as

$$\begin{bmatrix} {}^0x \\ 1 \end{bmatrix} = \begin{bmatrix} {}^0C_1 & {}^0d_1 \\ 0^T & 1 \end{bmatrix} \begin{bmatrix} {}^1x \\ 1 \end{bmatrix} \tag{3.8}$$
$$\mathbf{{}^0x = {}^0T_1\,{}^1x}$$

where $\mathbf{{}^0T_1}$ is the 4×4 affine or homogeneous transformation matrix which completely specifies the affine coordinate system change from $\{\underline{o}_1, \underline{C}_1\}$ to $\{\underline{o}_0, \underline{C}_0\}$. It can be interpreted geometrically as a rotation about an arbitrary axis followed by a translation. The point representations $\mathbf{{}^0x}$ and $\mathbf{{}^1x}$ are known as homogeneous coordinates.

Representing coordinate changes as homogeneous transformation matrices has many advantages. Multiple coordinate system changes can be combined to form a single homogeneous matrix specifying the overall transformation:

$$\begin{aligned} \mathbf{{}^0x} &= \mathbf{{}^0T_1\,{}^1x} \\ \mathbf{{}^1x} &= \mathbf{{}^1T_2\,{}^2x} \\ \mathbf{{}^2x} &= \mathbf{{}^2T_3\,{}^3x} \\ \therefore \mathbf{{}^0x} &= \mathbf{{}^0T_1\,{}^1T_2\,{}^2T_3\,{}^3x} \\ \mathbf{{}^0x} &= \mathbf{{}^0T_3\,{}^3x} \end{aligned} \tag{3.9}$$

where $\mathbf{{}^0T_3 = {}^0T_1\,{}^1T_2\,{}^2T_3}$. Since $\mathbf{T}$ is always full rank, its inverse always exists, and provides a convenient method for finding the opposite transformation between two coordinate systems:

$$\begin{aligned} \mathbf{{}^0x} &= \mathbf{{}^0T_1\,{}^1x} \\ (\mathbf{{}^0T_1})^{-1}(\mathbf{{}^0x}) &= (\mathbf{{}^0T_1})^{-1}(\mathbf{{}^0T_1\,{}^1x}) \\ \mathbf{{}^1T_0\,{}^0x} &= \mathbf{{}^1x} \end{aligned} \tag{3.10}$$

where $\mathbf{{}^1T_0}$ is the inverse matrix of $\mathbf{{}^0T_1}$ and represents the transformation from the coordinate system $\{\underline{o}_0, \underline{C}_0\}$ to $\{\underline{o}_1, \underline{C}_1\}$.

3.3.2 System Description

The patient positioning process inside the radiotherapy treatment room can be viewed in mathematical terms as a coordinate transformation from the simulation CT coordinates, where the treatment plan is defined, to the LINAC coordinates, where the treatment plan is executed. Conventionally, this is achieved through the use of fiducial markers in CT scans to denote the axes of the LINAC. However, this method relies on some key assumptions:

- accurate alignment of skin marks to lasers denoting the LINAC axes.
- skin marks do not move during the course of treatment.
- internal organs do not move with respect to skin marks.

As mentioned in the previous chapter, these assumptions are met with varying degrees of accuracy, leading to errors in patient positioning for treatment. To improve positioning accuracy, the proposed ultrasound localisation system circumvents these assumptions using the sequence of coordinate transformations shown in Figure 3.5. These transformations are further described below:

$^{Pat}\mathbf{T}_{CT}$ The CT to patient transformation. This is calculated using the IRED locations on the patient's skin and in the CT scan to form a set of corresponding points in both coordinates.

$^{O}\mathbf{T}_{Pat}$ The patient to OPTOTRAK transformation. This is given by the locations of the IREDs on the patient measured by OPTOTRAK.

$^{P}\mathbf{T}_{O}$ The OPTOTRAK to ultrasound probe transformation. This is given by OPTOTRAK measured locations of the IREDs on the probe.

$^{U}\mathbf{T}_{P}$ The ultrasound probe to ultrasound image transformation. This is constant provided the mounting bracket remains rigidly secured to the probe. It can be pre-determined in an off-line calibration procedure.

$^{U'}\mathbf{T}_{U}$ The transformation between simulation and treatment ultrasound images of the target anatomy. This can be calculated using a suitable automatic image registration algorithm.

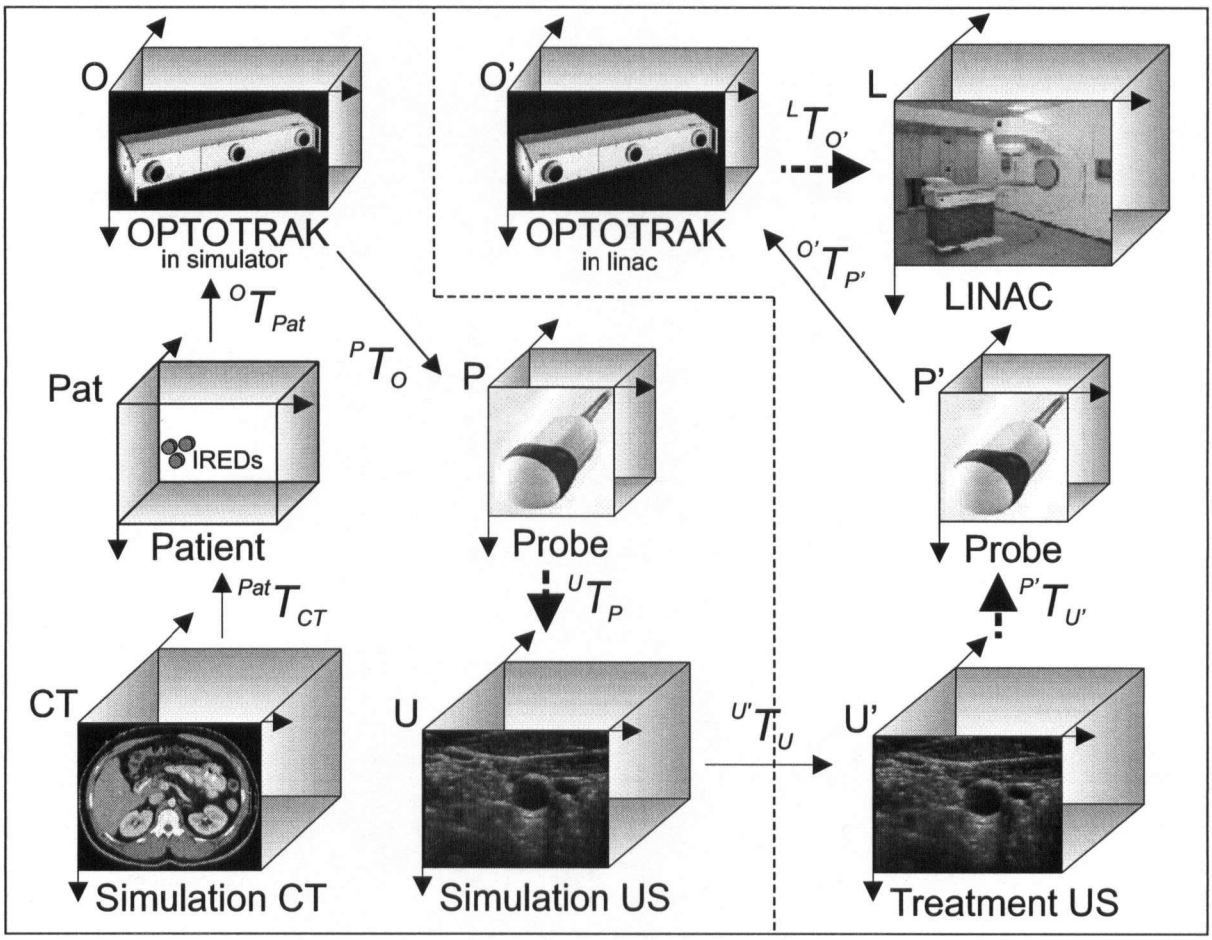

Figure 3.5: The series of coordinate transformations from the simulation CT to the LINAC coordinates when using the proposed system to position patients. Calibration parameters known *a priori* are shown by dashed arrows. Note that if the same probe is used for ultrasound imaging, ${}^{\mathbf{U}}\mathbf{T}_{\mathbf{P}} = ({}^{\mathbf{P}'}\mathbf{T}_{\mathbf{U}'})^{-1}$. The data collected during the simulation procedure and before each treatment fraction are shown in the left and right panels, respectively.

${}^{\mathbf{P}'}\mathbf{T}_{\mathbf{U}'}$ The ultrasound image to probe transformation for the treatment session. If the same probe is used as during simulation, this is the inverse of ${}^{\mathbf{U}}\mathbf{T}_{\mathbf{P}}$ above.

${}^{\mathbf{O}'}\mathbf{T}_{\mathbf{P}'}$ The ultrasound probe to OPTOTRAK transformation. This given by OPTOTRAK measurements inside the treatment room.

${}^{\mathbf{L}}\mathbf{T}_{\mathbf{O}'}$ The OPTOTRAK to LINAC transformation. This can be found by off-line calibration.

The chain of transformations in Figure 3.5 can be used to find the LINAC coordinates of any point in the simulation CT at the time of treatment. For example, the location of the planned isocenter ${}^{CT}\mathbf{x}_{iso}$ in the LINAC is given by

$$ {}^{L}\mathbf{x}_{iso} = {}^{L}\mathbf{T}_{O'}{}^{O'}\mathbf{T}_{P'}{}^{P'}\mathbf{T}_{U'}{}^{U'}\mathbf{T}_{U}{}^{U}\mathbf{T}_{P}{}^{P}\mathbf{T}_{O}{}^{O}\mathbf{T}_{Pat}{}^{Pat}\mathbf{T}_{CT}{}^{CT}\mathbf{x}_{iso}. \tag{3.11} $$

Similarly, the entire treatment plan, defined in CT coordinates, may be transformed into the LINAC coordinates. This enables discrepancies in the planned and actual location and orientation of the target at the time of treatment to be detected and corrected.

3.4 System Comparison With Existing Approaches

In this section, the proposed system will be compared with existing ultrasound-based patient positioning systems using the same mathematical framework as the previous section.

3.4.1 BAT/SonArray

Both of these systems have the same approach for finding the coordinate transformation from simulation CT to LINAC. Unlike the proposed system, the simulation ultrasound is omitted and the simulation CT is directly registered with the treatment ultrasound. This is done by manually matching contours outlined from the CT scan with features seen in the ultrasound image. The computation of the planned isocenter location in the LINAC coordinates ${}^{L}\mathbf{x}_{iso}$ is thus:

$$ {}^{L}\mathbf{x}_{iso} = {}^{L}\mathbf{T}_{O'}{}^{O'}\mathbf{T}_{P'}{}^{P'}\mathbf{T}_{U'}{}^{U'}\mathbf{T}_{CT}{}^{CT}\mathbf{x}_{iso} \tag{3.12} $$

where each of the transformations except ${}^{U'}\mathbf{T}_{CT}$ is the same as in Figure 3.5, and OPTOTRAK may be replaced by another position tracking system (e.g., articulated arm).

Note that the transformation ${}^{U'}\mathbf{T}_{CT}$ in Equation 3.12 has only a translational component and no rotations. This is because the user of these systems is only able to correct misalignments between CT and ultrasound scans using translational shifts in the manual image registration

process. Therefore, in the presence of any orientation error, it will actually be impossible for the therapist to obtain the correct image registration result. This means that not only will patient orientation inaccuracies remain uncorrected, but that errors to the translational component of the registration results are likely to be introduced.

In the previous chapter, the difficulties involved in performing manual registration of ultrasound and CT images were highlighted for the BAT system. These include differences in the appearance of anatomy in the two modalities, uncertainties in manual contouring of CT structures, and the subjective nature of the registration. This is the primary motivation for acquiring an additional ultrasound during simulation and performing automatic ultrasound to ultrasound image registration in the proposed system. An additional benefit of this scheme can be seen if one considers the introduction of a systematic error into the ultrasound imaging process. This systematic error can be denoted by the transformation matrix $\mathbf{T_{err}}$ and, for example, could represent a probe calibration error (error in determining the transformation ${}^{\mathbf{P}}\mathbf{T_U}$).

When $\mathbf{T_{err}}$ is applied to Equation 3.11 for the proposed system, the result is:

$$ {}^{\mathbf{L}}\mathbf{X_{iso}} = {}^{\mathbf{L}}\mathbf{T_{O'}}{}^{\mathbf{O'}}\mathbf{T_{P'}}(\mathbf{T_{err}}){}^{\mathbf{P'}}\mathbf{T_{U'}}{}^{\mathbf{U'}}\mathbf{T_U}{}^{\mathbf{U}}\mathbf{T_P}(\mathbf{T_{err}^{-1}}){}^{\mathbf{P}}\mathbf{T_O}{}^{\mathbf{O}}\mathbf{T_{Pat}}{}^{\mathbf{Pat}}\mathbf{T_{CT}}{}^{\mathbf{CT}}\mathbf{X_{iso}}. \tag{3.13} $$

It can be easily seen that if ${}^{\mathbf{U'}}\mathbf{T_U} = I$ (which implies ${}^{\mathbf{P'}}\mathbf{T_P} = I$ since ${}^{\mathbf{P'}}\mathbf{T_{U'}} = {}^{\mathbf{P}}\mathbf{T_U}$ for the same probe), where I is the identity matrix, then Equation 3.13 reduce to:

$$ {}^{\mathbf{L}}\mathbf{X_{iso}} = {}^{\mathbf{L}}\mathbf{T_{O'}}{}^{\mathbf{O'}}\mathbf{T_{P'}}{}^{\mathbf{P}}\mathbf{T_O}{}^{\mathbf{O}}\mathbf{T_{Pat}}{}^{\mathbf{Pat}}\mathbf{T_{CT}}{}^{\mathbf{CT}}\mathbf{X_{iso}} \tag{3.14} $$

showing that the exact location of ${}^{\mathbf{L}}\mathbf{X_{iso}}$ can be recovered by the proposed system. Even if ${}^{\mathbf{U'}}\mathbf{T_U} \approx I$, some error cancellation is achievable. In contrast, when $\mathbf{T_{err}}$ is applied to Equation 3.12, the result is:

$$ {}^{\mathbf{L}}\mathbf{X_{iso}} = {}^{\mathbf{L}}\mathbf{T_{O'}}{}^{\mathbf{O'}}\mathbf{T_{P'}}\mathbf{T_{err}}{}^{\mathbf{P'}}\mathbf{T_{U'}}{}^{\mathbf{U'}}\mathbf{T_{CT}}{}^{\mathbf{CT}}\mathbf{X_{iso}} \tag{3.15} $$

indicating that no cancellation of $\mathbf{T_{err}}$ is possible for the BAT and SonArray systems. Therefore, the proposed system is capable of reducing systematic ultrasound errors if the simulation and treatment ultrasound images contain similar image content. For ultrasound scanning of many

anatomical sites, the probe must be positioned at certain locations and orientations to produce good quality images. Therefore, in these situations, repeat scanning may indeed yield images containing similar anatomical features and geometries. In addition, the use of dedicated 3D ultrasound probes in the proposed system removes the need for the operator to manually sweep the probe across the skin, further promoting the reproducibility of ultrasound images used for registration.

The fact that the ultrasound probe remains in the same place during acquisition of 3D images using dedicated probes also means that possible tissue deformation due to probe pressure could potentially be reproduced if the same contact force is used during imaging. McGahan *et al.* showed that tissue displacement caused by probe pressure when using the BAT system could be corrected using translational shifts in the anterior-posterior direction [72]. In addition, Artignan *et al.* reported that prostate displacement was mainly in the anterior-posterior direction and was highly correlated to the amount of downward displacement of the probe from first contact with the skin [4]. These studies suggest that tissue deformation due to probe pressure could be approximated by a rigid-body transformation in the form of $\mathbf{T_{err}}$, and may be reproducible, which would subject this type of error to possible cancellation in the proposed 3D ultrasound patient positioning system, as shown in Equation 3.13.

3.4.2 Restitu

It is believed that the Restitu system uses the following series of transformations to determine ${}^{\mathbf{L}}\mathbf{X_{iso}}$:

$$ {}^{\mathbf{L}}\mathbf{X_{iso}} = {}^{\mathbf{L}}\mathbf{T_{O'}}{}^{\mathbf{O'}}\mathbf{T_{P'}}{}^{\mathbf{P'}}\mathbf{T_{U'}}{}^{\mathbf{U'}}\mathbf{T_{U}}{}^{\mathbf{U}}\mathbf{T_{P}}{}^{\mathbf{P}}\mathbf{T_{O}}{}^{\mathbf{O}}\mathbf{T_{Sim}}{}^{\mathbf{Sim}}\mathbf{T_{Pat}}{}^{\mathbf{Pat}}\mathbf{T_{CT}}{}^{\mathbf{CT}}\mathbf{X_{iso}} \tag{3.16} $$

where all terms are the same as in Figure 3.5, and OPTOTRAK may be replaced by another position tracking system. The exceptions are:

${}^{\mathbf{O}}\mathbf{T_{Sim}}$ The position tracker to simulator room coordinate transformation. The room coordinates are defined by the laser alignment system and this transformation can be pre-determined using an off-line calibration procedure.

$^{Sim}\mathbf{T}_{Pat}$ The patient to simulator room transformation. This is established by marking laser positions on the patient's skin.

$^{CT}\mathbf{T}_{Pat}$ The CT to patient transformation. This is accomplished by placing lead fiducial markers on skin markings and identifying the locations of these in the CT scan.

Similar to the proposed system, the Restitu acquires an additional simulation ultrasound and performs intramodality ultrasound-to-ultrasound registration to compare the treatment and simulation patient anatomy. However, a number of differences is also apparent.

During the simulation session, the body of the patient is not explicitly tracked by the Restitu system. Instead, markings and BB fiducials are placed on the skin before the CT scan to establish the patient's relationship with the alignment lasers. It is assumed that these can be accurately placed by the therapist, and that the patient can maintain a fixed relationship with respect to the lasers during CT and ultrasound acquisition. Any patient motion between the two scans results in an error in the implicitly registered simulation CT and ultrasound. This leads to a systematic error in the localisation of the target in the treatment room which affects every fraction of the treatment.

In contrast, IREDs are used to track both the patient and the ultrasound probe simultaneously during ultrasound image acquisition by the proposed system. Furthermore, the extra calibration parameter $^{O}\mathbf{T}_{Sim}$ used by the Restitu is not needed. Unlike BB fiducials, which must be precisely placed at the alignment laser markings, IREDs can be placed anywhere on the patient's body near the treatment site. Their locations in both the OPTOTRAK and CT coordinates are used to find the transformation from CT to OPTOTRAK. This in turn enables the CT to be spatially registered to the ultrasound scan. By tracking IREDs on the patient, patient motion between CT and ultrasound acquisition can be measured. This allows any error to be detected and possibly the rigid-body component of that motion to be corrected. If the motion has a large non-rigid component, this would be easily detected as a large registration error between IRED locations in CT and OPTOTRAK coordinate systems. In such a situation, repeat ultrasound or CT scans could be taken immediately.

Introducing a systematic ultrasound imaging error into Equation 3.16, the result is:

$$^{L}\mathbf{X_{iso}} = {}^{L}\mathbf{T_{O'}}{}^{O'}\mathbf{T_{P'}}(\mathbf{T_{err}})^{P'}\mathbf{T_{U'}}{}^{U'}\mathbf{T_{U}}{}^{U}\mathbf{T_{P}}(\mathbf{T_{err}^{-1}})^{P}\mathbf{T_{O}}{}^{O}\mathbf{T_{Sim}}{}^{Sim}\mathbf{T_{Pat}}{}^{Pat}\mathbf{T_{CT}}{}^{CT}\mathbf{X_{iso}}. \quad (3.17)$$

It can be seen from Equation 3.17 that error cancellation is possible with the Restitu, similar to the proposed system. However, volumetric ultrasound data is generated using a freehand approach by manually sweeping the probe in the Restitu system instead of a dedicated 3D probe. Therefore, the requirement that $^{U'}\mathbf{T_U} \approx I$ for error cancellation is less likely to be met in practice than the proposed system.

Finally, the method used by the Restitu and the proposed system for finding $^{U'}\mathbf{T_U}$, the registration between simulation and treatment ultrasound, is different. Although both systems perform full 6 DOF registration automatically, the Restitu uses limited manual contour data as input for the registration algorithm. This requires manual input to the registration process and introduces the possibility of user error and bias. Furthermore, the entire image information is not used in calculating the best registration. With the Voluson 730 and dedicated 3D probes, it is anticipated that ultrasound images of sufficient quality will be generated to allow automatic pixel-intensity based registration algorithms to be used in the proposed system. In addition, the greater likelihood of obtaining similar views of the anatomy with dedicated 3D probes will also aid registration of simulation and treatment ultrasound. This is because the appearance of anatomical features as well as the presence of artifacts in ultrasound are known to be viewpoint dependant [81]. In the next chapter, experimental results which demonstrates the feasibility of automatic registration of 3D ultrasound images acquired with the Voluson 730 will be presented.

Chapter 4

Feasibility Tests

In this chapter, two key components of the ultrasound patient positioning scheme proposed in Chapter 3 are evaluated. Firstly, the proposed method for registering simulation CT and ultrasound is implemented on a phantom to assess the accuracy of this approach. In addition, to determine whether automatic pixel-intensity based 3D ultrasound-to-ultrasound registration is possible, a correlation coefficient based method is used to rigidly register ultrasound images collected from the neck of a volunteer. These experiments are the first attempts at investigating the magnitude of error sources in the proposed 3D ultrasound patient positioning system under optimal conditions, and will aid in establishing the expected overall accuracy of the entire system. The methods and results of these experiments are presented in the following sections.

4.1 CT to Ultrasound Registration

In order to evaluate the accuracy of the proposed CT to ultrasound registration procedure, the series of transformations shown in Figure 4.1 was used to register CT and ultrasound images of a phantom object. In this case, the patient in Figure 4.1 is simply substituted by the phantom, while all other aspects of the registration process remains as depicted. Since the phantom is an immobile and incompressible object, this experiment represents the best-case scenario for registration accuracy and establishes the lower bounds in the accuracy of the proposed methods.

To validate the accuracy of the registration result, point features inside the phantom are identified in both the CT and ultrasound volumes. The locations of these features can then be compared between registered volumes to produce the target registration error (TRE) [28].

As previously described in Section 3.3.2, the proposed registration method involves the use of IRED markers as fiducials in CT and OPTOTRAK measurement of both the ultrasound probe

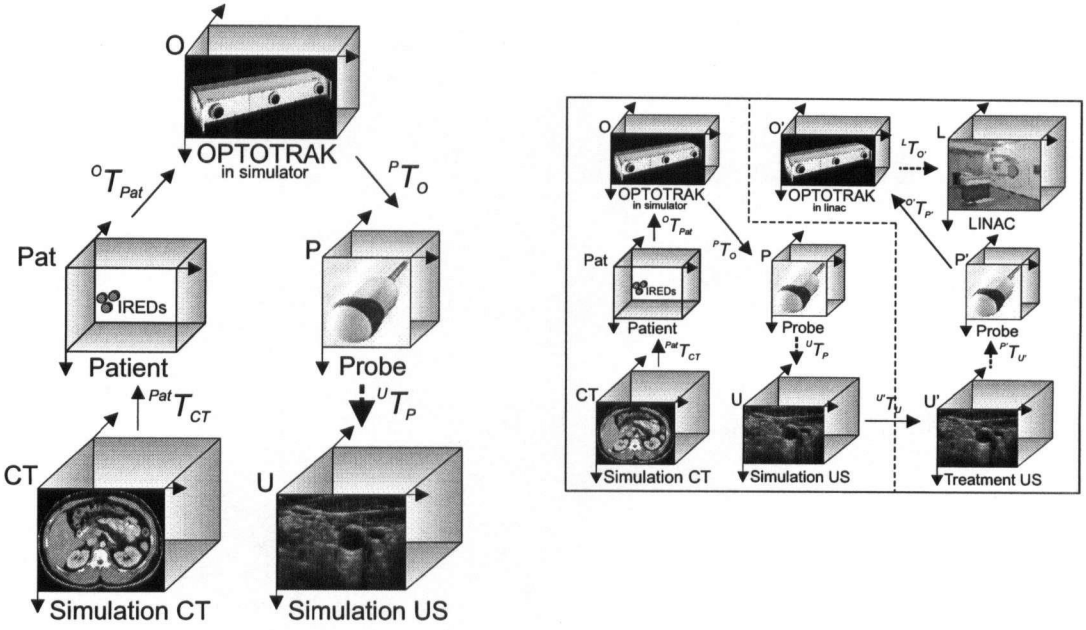

Figure 4.1: The series of coordinate transformations used by the proposed 3D ultrasound patient positioning system to register the simulation CT and ultrasound images. The accuracy of this procedure is evaluated in this section on a phantom patient. The entire series of coordinate transformations used to localise the patient inside the LINAC, previously shown in Figure 3.5, is displayed in the right-hand panel for comparison.

and patient position. To the author's knowledge, the direct use of OPTOTRAK IREDs as fiducial markers in CT for image registration has not been previously reported. Therefore, this aspect of the work presented herein is unique, and should be of interest in the wider field of image registration. Details of the experimental procedures used, as well as the results of this test, are described in the following subsections.

4.1.1 Phantom Construction

The phantom used in the registration experiment consists of a plexiglass box with dimensions of $192 \times 147 \times 132mm$ $(L \times W \times H)$ embedded inside a plastic case and rigidly secured with screws, as shown in Figure 4.2. Stainless steel jewellery wire of 0.015 inch diameter were strung across the walls of the plexiglass box forming 2 crosses horizontally, and 2 crosses vertically to

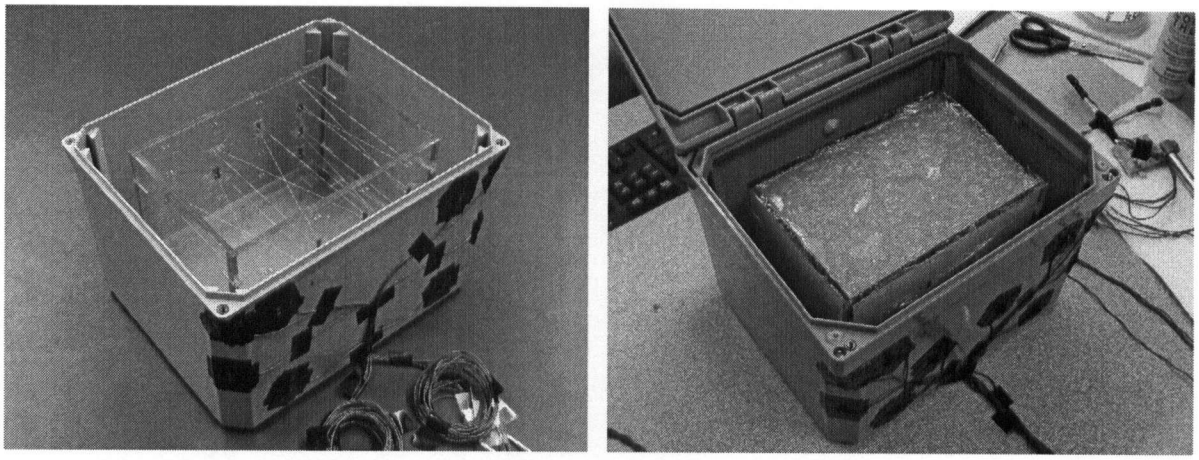

(a) Unfilled phantom.

(b) Filled phantom.

Figure 4.2: The phantom used in the CT to ultrasound registration experiment. It contains wire crosses to facilitate ultrasound probe calibration and speed of sound verification, and 8 IREDs attached outside. The plexiglass box is filled with an ultrasound tissue-equivalent material embedded with 43 aluminium BBs to act as point features. Ten lead BBs are secured to the plastic case using Blu-Tac^{TM} for calibrating IRED locations in CT, and can be seen in (b).

facilitate ultrasound probe calibration and phantom speed of sound verification (both described later). Eight IREDs were fixed to one side of the outer plastic case with tape to serve as CT fiducials and facilitate OPTOTRAK measurement of the phantom position. In addition, 10 lead BBs of $3.2mm$ diameter were secured to the walls of the outer plastic case with Blu-Tac^{TM} for calibrating the IRED locations in the CT image (described later).

The locations of the wire-ends at the walls of the plexiglass with respect to the IREDs on the case were accurately measured by touching the wire-ends with the tip of the stylus shown in Figure 4.3. At the same time, the IRED locations on both the case and stylus body were measured by the OPTOTRAK. From the IRED locations on the stylus, its tip location, and therefore the wire-end location, can be inferred. A single calibration procedure is required to determine the fixed relationship between the tip and IRED locations on the stylus. This involves pivoting the stylus on its tip through multiple planes while capturing IRED motion with OPTOTRAK. A more detailed description can be found in the OPTOTRAK Rigmaker manual [46].

To facilitate ultrasound imaging, the plexiglass box was filled with an ultrasound tissue-equivalent material once the wire-end locations had been recorded. The desirable physical and

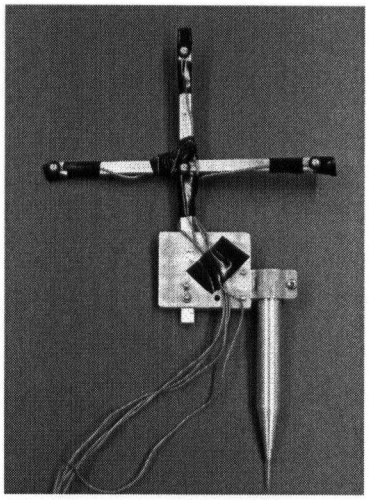

Figure 4.3: The stylus, which can be used by OPTOTRAK to measure the 3D location of any point. The fixed relationship between the locations of the IREDs and the tip of the stylus can be determined using a calibration procedure.

acoustic properties for such a material include [15]:

Acoustic attenuation coefficient $0.2 \pm 0.1 dBcm^{-1}$ at $1MHz$, approximate linear dependance on frequency.

Acoustic velocity $1540 \pm 20ms^{-1}$.

Internal scattering and reflection Negligible.

Density $1.05 \pm 0.1gcm^{-1}$.

Phase Solid.

Thermal stability Up to $65°C$.

Temporal stability Resistant to chemical (including ultrasound scanning gel) and bacterial/fungal action.

Repeatability of properties.

Ease of manufacture.

The choice of materials that meet the above criteria are generally limited to water-based gels (hydrocolloids). These alternate between solid and liquid states with changes in temperature, and are relatively easy to manufacture. Several authors have reported the use of gelatine gels derived from animal hide [15, 68]. Typically, these gels are doped with materials such as oil, alcohol, and graphite to independently control various acoustic parameters. Alternatively, gels based on agar extracted from seaweed have also been used. In [14], Burlew *et al.* showed that agar gels could be manufactured to exhibit many of the desired properties of an ultrasound tissue-equivalent material, including a speed of sound of $1540ms^{-1}$. Due to the simple formulation of this gel, it was chosen to fill the phantom.

The ultrasound tissue-equivalent gel consists of (by weight) 3% high gel strength agar (Sigma-Aldrich, St. Louis, MO), 8.6% n-propanol (Fisher Scientific, Hampton, NH), and 88.4% distilled water (Anachemia, Montreal, Canada). The concentration of n-propanol was used to regulate the acoustic velocity of the gel to $1540ms^{-1}$. Briefly, it was manufactured by heating all the ingredients to $90°C$ until a homogeneous and transparent solution was obtained. It was subsequently cooled to $45°C$, and then poured into the plexiglass box, where it was allowed to congeal. For a detailed description of gel manufacture, the reader is referred to Appendix A.

Before the gel solution completely coagulated, point features for validating registration accuracy in the form of 43 aluminium BBs of $1mm$ diameter were introduced randomly into the mixture. To prevent the BBs sinking to the bottom, the outer plastic case of the phantom was filled with ice water so that the bottom half of the plexiglass box was immersed in a water bath. Thus, coagulation of the lower portion of the gel solution was accelerated, and provided a solid base for the BBs to settle on.

Once the BBs were inserted into the gel, the ice water was pumped out of the outer case of the phantom. Coagulation of the entire gel volume was then allowed to take place inside a refrigerator. Upon hardening, the top of the gel was covered by a layer of saran wrap to prevent desiccation. This thin layer of plastic has negligible effect on ultrasound scanning and is left in place permanently. A view of the phantom filled with the ultrasound tissue-equivalent gel is shown in Figure 4.2(b).

An added benefit of having n-propanol in the gel is that it acts as a preservative to inhibit

bacterial and fungal growth. The phantom is kept inside the fridge when not in use, and desiccation of the gel has remained insignificant more than one year after manufacture.

4.1.2 Phantom Speed of Sound Verification

In ultrasound imaging, sound waves are used to interrogate the anatomy and form an image of its structure. The ultrasound transducer sends pulses of sound into tissue, where it is attenuated, scattered, and reflected back to the transducer. These echoes are then used to form an image of the underlying anatomy.

One of the fundamental assumptions inherent in ultrasound imaging is that all tissue have an identical acoustic velocity of $1540ms^{-1}$. This allows the time delay between echoes to be converted into distances on an image. This figure is based on the average acoustic velocity of human soft tissue, which ranges from $1460ms^{-1}$ to $1580ms^{-1}$ [18]. The variations in the actual acoustic velocity of tissue that the sound waves travel through can give rise to geometric errors in the reconstructed ultrasound image.

As a simple illustration of the effects of ultrasound speed of sound error, consider the case where the tissue cross-section shown in Figure 4.4 is imaged by ultrasound. Fat has an acoustic velocity of $1479ms^{-1}$ [18]. Therefore, the time delay between the transmission of a pulse from the top of the fat layer in a straight line downwards, and an echo to return to the transducer is

$$\begin{aligned} t &= \frac{d}{v} \\ &= \frac{2 \times 0.020}{1479} \\ &= 27\mu s. \end{aligned} \tag{4.1}$$

Assuming an acoustic velocity of $1540ms^{-1}$ when reconstructing the ultrasound image from echo

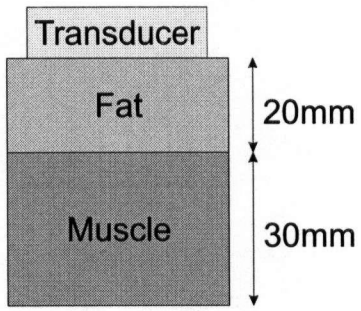

Figure 4.4: A cross-section of tissue containing a layer of fat on top of muscle.

data would then incorrectly place the depth of the fat/muscle interface at

$$\begin{aligned} d &= \frac{v \times t}{2} \\ &= \frac{1540 \times 27 \times 10^{-6}}{2} \\ &= 20.8mm, \end{aligned} \tag{4.2}$$

giving an error of $0.8mm$.

To minimise geometric inaccuracies in ultrasound images of the phantom due to speed of sound errors, the gel was prepared using the formula given [14] for achieving an acoustic velocity of $1540ms^{-1}$, as previously mentioned. After gel manufacture, its actual acoustic velocity was verified by comparing the physical distance between the center of the two vertical wire crosses in the phantom with their observed distance in an ultrasound image.

As perviously described, the physical locations of the wire-ends forming the two vertical crosses in the phantom were measured using the stylus. These locations are illustrated in Figure 4.5(a). From the wire-end locations, equations for the straight lines which intersect to form the crosses ($\overline{ad}, \overline{bc}, \overline{eh}, \overline{fg}$ in Figure 4.5(a)) can be derived. The 3D point with the least distance to the two lines which form a single cross is then taken as the center of that cross (x_1 and x_2 in Figure 4.5(a)). Finally, the 3D distance between the cross centers is calculated, and the result is

$$\|x_1 - x_2\|_{stylus} = 52mm. \tag{4.3}$$

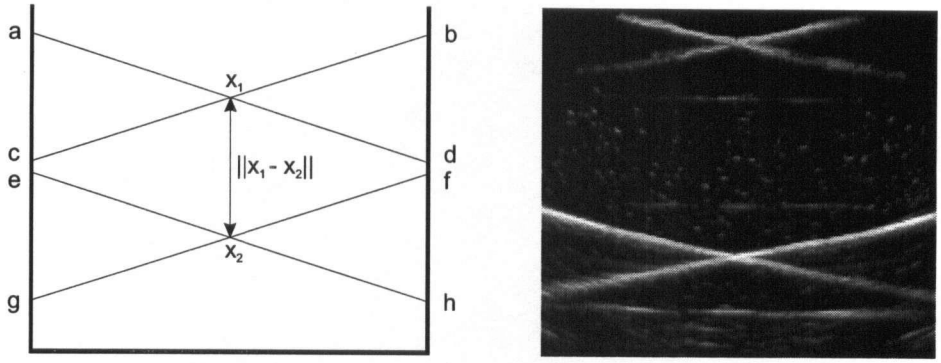

(a) (b)

Figure 4.5: The arrangement of vertical crosses inside the phantom (a) and their appearance in an ultrasound image (b). The wire-end locations marked a - g are measured using the stylus and used to calculate the distance between the cross centers x_1 and x_2. The same distance is measured directly from an ultrasound volume of the phantom.

The same two points x_1 and x_2 were identified in an ultrasound volume of the phantom taken using the Voluson 730. An axial slice of the volume containing the two crosses is shown in Figure 4.5(b). The cross centers were found by calculating the image weighted centroid in a surrounding region of interest (ROI). The 3D distance between the cross centers measured from ultrasound is

$$\|x_1 - x_2\|_{ultrasound} = 52.2mm. \tag{4.4}$$

Taking the stylus measured result as the actual distance between x_1 and x_2, the speed of sound in the phantom can be estimated:

$$\begin{aligned} v &= \frac{\|x_1 - x_2\|_{stylus} \times 1540}{\|x_1 - x_2\|_{ultrasound}} \\ &= 1533ms^{-1}. \end{aligned} \tag{4.5}$$

This represents an error of less than 0.5% from the nominal speed of sound assumed by ultrasound scanners. Therefore, the effects of speed of sound error on the geometric accuracy of ultrasound images of the phantom will be minimal.

4.1.3 Ultrasound Probe Calibration

Ultrasound probe calibration is the process of finding the rigid-body transformation from the ultrasound probe coordinate system to the ultrasound image coordinate system (${}^{\mathbf{P}}\mathbf{T}_{\mathbf{U}}$ in Figure 4.1). Various methods for performing ultrasound probe calibration exist in the literature, and have been reviewed [75]. Most of these techniques deal with calibration of 2D probes. Generally, a phantom with known geometric properties is scanned by a tracked ultrasound probe. The positions of the features as seen in the ultrasound images are then compared with their known locations. This, combined with knowledge of the location of the probe, enables the rigid body transformation between the probe and image to be solved.

Recently, Poon and Rohling [87] proposed three probe calibration methods for dedicated 3D ultrasound probes. These were tested on the same ultrasound system used throughout this study, the Voluson 730. The IXI-wire method was found to have a root-mean-squre (RMS) point reconstruction accuracy of $2.15mm$, and produced the most accurate results out of the three approaches. Therefore, this method was used for probe calibration in this study.

The IXI-wire calibration method utilises a phantom containing 2 layers of wires strung in the shapes of the letters 'IXI'. For convenience, these features are incorporated directly into the phantom used to test CT to ultrasound registration accuracy so that the same phantom can also be used for probe calibration. Although the exact dimensions of the wires are not identical to the ones used by Poon and Rohling, their configuration is essentially the same. The IXI-wires can be seen in the image of the unfilled phantom in Figure 4.2(a).

As mentioned previously, the wire-end locations forming the IXI shapes were measured using the stylus. This enables a virtual representation of the geometry of the wires with respect to the coordinate system defined by the IREDs on the phantom to be calculated. The virtual model of the IXI-wires is shown in Figure 4.6(a).

To calibrate the ultrasound probe, an ultrasound volume of the phantom is acquired while both the probe and phantom position is measured by OPTOTRAK. This gives the rigid-body transformation between the probe coordinate system $\{\underline{o}_P, \underline{C}_P\}$ and the phantom coordinate system $\{\underline{o}_{Pat}, \underline{C}_{Pat}\}$, denoted by ${}^{\mathbf{Pat}}\mathbf{T}_{\mathbf{P}}$. Next, the acquired ultrasound volume containing the IXI-wires is

rigidly registered to the virtual model of the phantom. This gives the transformation between the phantom coordinate system and the ultrasound volume coordinate system $\{\underline{o}_U, \underline{C}_U\}$, denoted by ${}^{\mathbf{Pat}}\mathbf{T}_{\mathbf{U}}$. This registration was performed using the Amira 3D visualisation toolkit (TGS Inc., San Diego, CA), which uses a gradient descent technique to maximise the image correlation coefficient [34]. The registration result of one calibration procedure is shown in Figure 4.6(b). Finally, the probe calibration matrix ${}^{\mathbf{P}}\mathbf{T}_{\mathbf{U}}$ can be calculated using:

$$ {}^{\mathbf{P}}\mathbf{T}_{\mathbf{U}} = ({}^{\mathbf{Pat}}\mathbf{T}_{\mathbf{P}})^{-1}\ {}^{\mathbf{Pat}}\mathbf{T}_{\mathbf{U}} \tag{4.6} $$

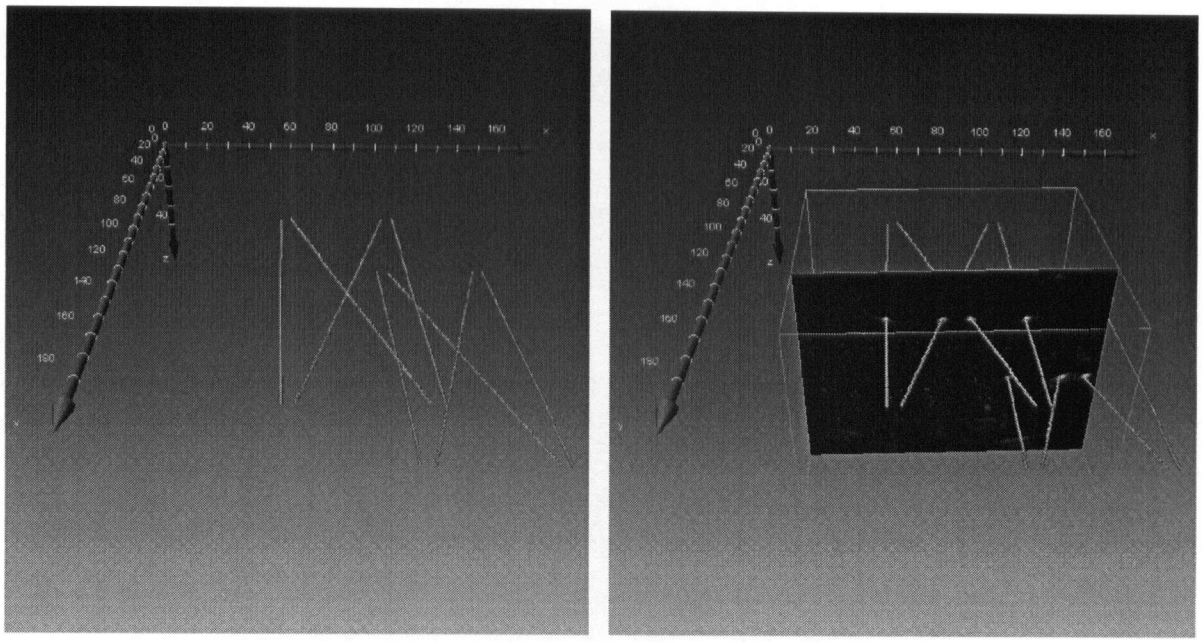

(a) IXI-wire model

(b) Calibration registration result

Figure 4.6: The IXI-wire model created from wire-end locations measured using the stylus (a). The model is created in the phantom coordinate system, established by IREDs attached to the side of the phantom. The axes of this coordinate system is shown for reference. The registration result between the IXI-wire model and an ultrasound volume of the phantom during one calibration procedure is shown in (b). Note that only one axial slice of the volume is displayed, but the entire volume is used to compute the registration. Images are rendered using Amira.

4.1.4 Data Acquisition

The phantom was scanned at the BC Cancer Agency (BCCA) using a PQ5000 CT simulator (Picker International, Cleveland, OH). The volume had dimensions of $350 \times 350 \times 267mm$, a slice thickness of $2mm$, slice spacing of $1.5mm$, and a pixel spacing of $0.6836mm$. The minimum slice thickness and spacing possible was used to reduce partial volume effects and ensure that BBs and IRED markers would be visible in the CT volume.

On the same day, the phantom was imaged using the Voluson 730 with the dedicated 3D RAB4-8P probe as shown in Figure 4.7. The ultrasound imaging parameters were optimised for image quality, including using the maximum number of focal spots available, the slowest frame rate, and harmonic imaging to reduce reverb artifacts from the metal wires and BBs inside the phantom. Nine ultrasound volumes were obtained with the probe at different positions in order to image the entire phantom. The dimensions of each volume was $109 \times 85 \times 96mm$ and the voxel size $0.55mm$.

During imaging, both the probe and phantom position were measured by the OPTOTRAK. These measurements allow the probe to OPTOTRAK coordinate transformation ${}^{\mathbf{P}}\mathbf{T}_{\mathbf{O}}$, and the OPTOTRAK to phantom coordinate transformation ${}^{\mathbf{O}}\mathbf{T}_{\mathbf{Pat}}$, to be determined. The relationship between these parameters and the overall CT to ultrasound registration scheme was shown on Figure 4.1.

4.1.5 IRED CT Offset

The only remaining parameter still required to complete the CT to ultrasound registration process is the transformation from CT coordinates to the phantom coordinates, ${}^{\mathbf{Pat}}\mathbf{T}_{\mathbf{CT}}$. To find this transformation, the locations of the IRED markers in the CT scan are extracted. The locations of the same markers on the phantom were measured by OPTOTRAK during ultrasound scanning, as described in the previous subsection. A least-squares minimisation of the 3D distances between all the pairs of corresponding markers would then give the best estimate for ${}^{\mathbf{Pat}}\mathbf{T}_{\mathbf{CT}}$. This minimisation is calculated using Horn's unit quaternion method [42].

The most convenient approach of finding the IRED locations in CT is to simply compute the

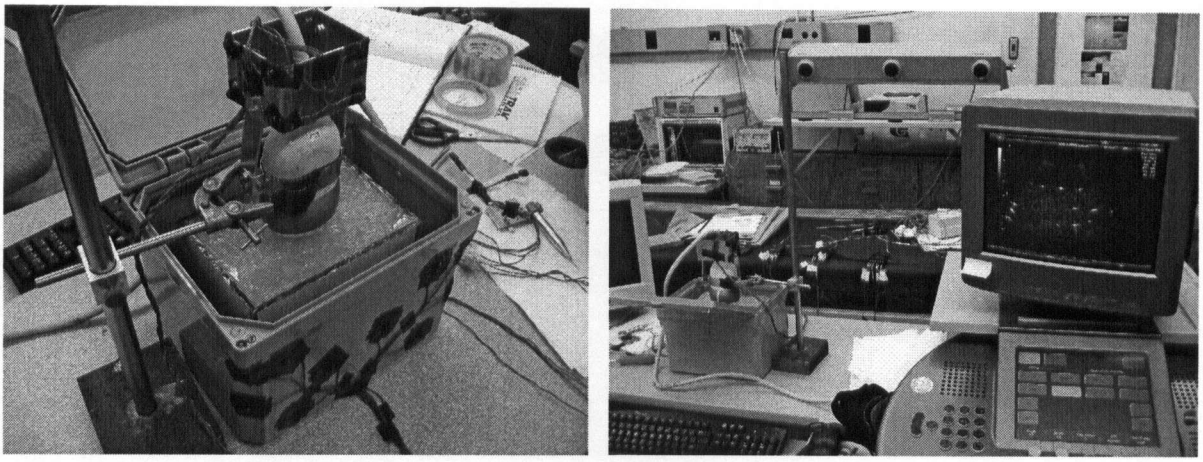

(a) (b)

Figure 4.7: Ultrasound scanning of the phantom. The ultrasound probe is held in place by a vice during volume acquisition (a). Both the probe and phantom positions are measured by the OPTOTRAK during scanning (b).

image centroid in a ROI surrounding the IRED. However, the centroid location may not be exactly the same as the IRED location measured by the OPTOTRAK. Therefore, the offset from the CT image centroid to the OPTOTRAK measured IRED location is determined through a calibration process.

The geometry of an IRED is shown in Figure 4.8. They are disk-like in shape with one axis of symmetry. Infra-red light is emitted from the top side of the IRED, so this side must be within the view of the OPTOTRAK cameras for the marker position to be measured. Previously, Flaccavento [29] has shown that the OPTOTRAK measured IRED location has negligible deviation from the axis of symmetry of the IRED. Therefore, the direction of the required offset is assumed to be along the IRED axis of symmetry.

To find the required offset, the image centroids of the ten additional lead BBs adhered to the phantom with Blu-Tac^{TM} were identified in the CT scan. The locations of these BBs with respect to the phantom IREDs were also determined by moving the tip of the stylus over their surfaces to generate a cloud of surface points. A least-squares sphere fitting algorithm [89] was then used to find the center of the BBs. A typical result of sphere fitting is shown in Figure 4.9.

Thus, the lead BB center locations in both the phantom and CT coordinates were determined.

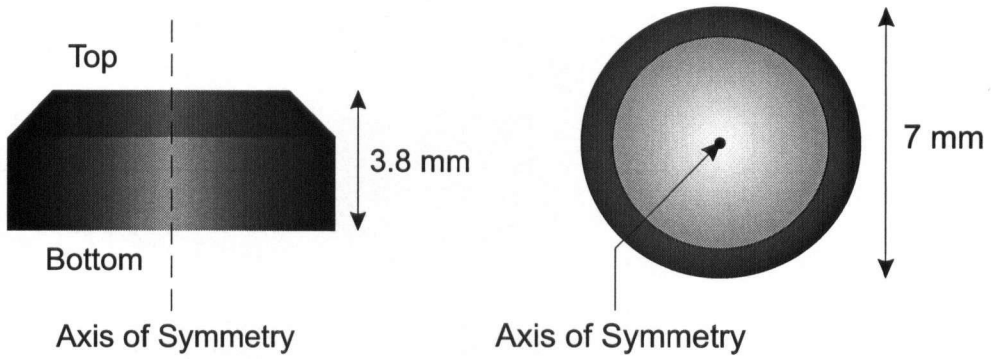

(a) Side view (b) Top view

Figure 4.8: OPTOTRAK IRED geometry.

They provide an additional set of corresponding points in the two coordinates systems, enabling ${}^{\mathbf{Pat}}\mathbf{T}_{\mathbf{CT}}$ to be calculated independently of using the IRED markers. The locations of the OPTOTRAK measured IREDs on the phantom can then be transformed into CT coordinates using ${}^{\mathbf{Pat}}\mathbf{T}_{\mathbf{CT}}$ and compared with their centroid locations to determine the required offset along the axis of symmetry.

The calibration result for one IRED is shown in Figure 4.10(a). The IRED axis of symmetry is estimated from its CT image by first thresholding to obtain the IRED voxels, and then using principal component analysis [34]. For a disk, the axis of symmetry corresponds to the principal axis with the smallest eigenvalue in the image covariance matrix. In addition, the positive direction of the axis of symmetry is defined to point from the base of the maker to the top. The IRED base can be easily distinguished from its top since it is always adjacent to another x-ray attenuating object, rather than exposed to air. Thus, the top side of the IRED will always be adjacent to voxels with lower intensity than the voxels adjacent to the bottom side.

Due to limitations in CT spatial resolution, and the small size of the IRED, the estimated IRED axis of symmetry will not pass through the OPTOTRAK measured IRED location exactly. Therefore, a residual calibration error will remain if an offset along the estimated IRED axis of symmetry is used to calibrate the IRED location. To minimise this residual calibration error, the calibration offset is chosen as the projection of the measured offset, defined as the vector from the IRED image centroid to its OPTOTRAK measured location, onto the IRED axis of symmetry,

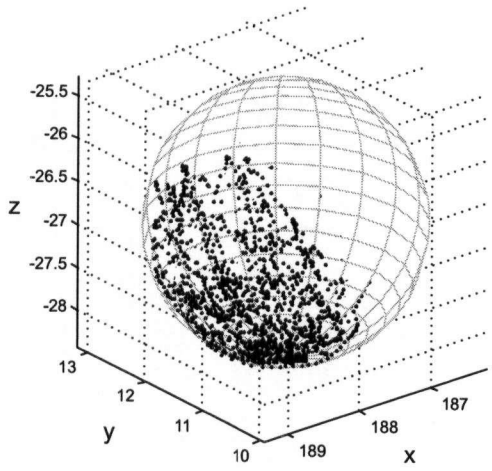

Figure 4.9: Result of fitting a sphere to the cloud of surface points generated by moving the tip of the stylus over a BB's surface. The number of points collected is 2252 and their locations are given in the phantom coordinate system. The least-squares fit sphere has a diameter of $3.1mm$, compared to the BB's physical diameter of $3.2mm$ measured with a caliper. The RMS error in the spherical fit over all 2252 data points in this case is $0.04mm$.

as shown in Figure 4.10(b). Provided the angle between the measured offset and the axis of symmetry is small, the residual calibration error will be small.

The required calibration offset along the axis of symmetry was calculated for all 8 IREDs on the phantom. The average offset, along with other calibration parameters for the 8 IREDs, are shown in Table 4.1. The average offset of $1.47mm$ is subsequently used to calculate the all the CT IRED locations. Thus, the location of any IRED in the CT volume is determined by:

- Finding the image centroid of the IRED.
- Estimating the axis of symmetry using principal component analysis.
- Inspecting the voxel values along the axis of symmetry to determine the positive direction of the axis.
- Applying an offset of $1.47mm$ along the positive direction of the axis of symmetry away from the centroid.

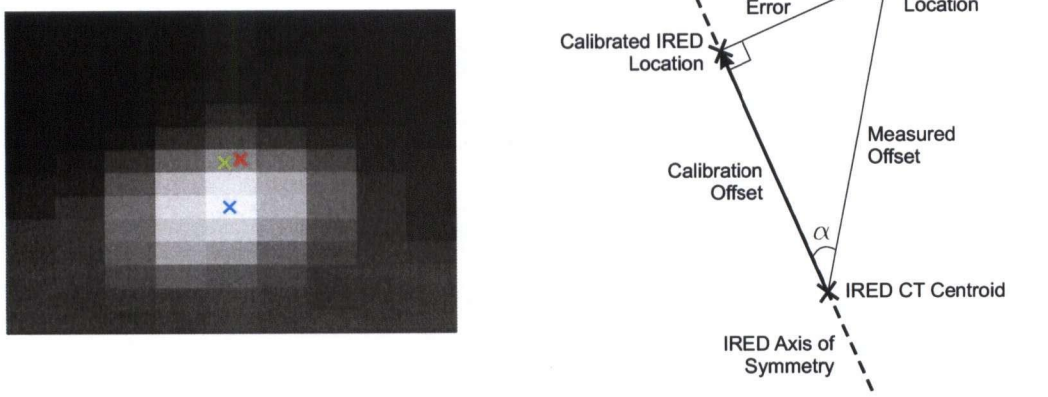

(a) IRED CT cross-section

(b) Relationship between calibration parameters

Figure 4.10: Calibration results for one IRED (a). The image centroid is marked with the blue cross, the OPTOTRAK measured IRED location with the red cross, and the calibrated IRED location with the green cross. Note that these points are projected onto the image plane for display. The relationship between calibration parameters are shown in (b). The calibration offset is found by projecting the measured offset onto the IRED axis of symmetry. As long as angle α remains small, the residual calibration error will remain small.

Table 4.1: Average calibration parameters for the 8 IRED markers on the phantom.

Measured Offset (mm)	Average $\alpha(°)$	Calibration Offset (mm)	Residual Error (mm)
1.63	25	1.47	0.66

Using the average calibration offset of $1.47mm$ to calculate all the IRED locations results in an average residual calibration error of $0.70mm$ for the 8 IREDs. This value is slightly larger than the average residual calibration error obtained when the optimum offset is chosen for each IRED, shown in Table 4.1. The CT IRED locations determined by the above procedure are used with the OPTOTRAK measured IRED locations in the phantom coordinate system to find the transformation ${}^{\mathbf{Pat}}\mathbf{T}_{\mathbf{CT}}$. Least-squares minimisation of the 3D distances between corresponding markers in this registration yielded an average residual error of $0.74mm$.

The transformation ${}^{\mathbf{Pat}}\mathbf{T}_{\mathbf{CT}}$ obtained using IREDs can be compared to the same transformation calculated independently using the lead BBs as fiducials, which was used to calibrate the CT

IRED locations. To do this, the rigid-body homogeneous transformation matrix ${}^{\mathbf{Pat}}\mathbf{T}_{\mathbf{CT}}$ is completely expressed using 6 parameters: 3 translations x, y, z, and 3 rotations φ, ϑ, ψ (roll-pitch-yaw angles) [93]. This comparison is shown in Table 4.2. It can be seen that differences between the registration parameters are well under $1mm$ and 1°.

Table 4.2: Comparison of ${}^{\mathbf{Pat}}\mathbf{T}_{\mathbf{CT}}$ registration results using IRED fiducials and lead BB fiducials. The homogeneous transformation matrix ${}^{\mathbf{Pat}}\mathbf{T}_{\mathbf{CT}}$ is expressed in terms of 3 translations and 3 rotations (roll-pitch-yaw angles).

Registration Parameter	IRED fiducials	BB fiducials	Difference
$x(mm)$	798.0	797.3	0.7
$y(mm)$	104.6	104.2	0.4
$z(mm)$	330.1	330.6	0.5
$\varphi(°)$	90.0	90.1	0.1
$\vartheta(°)$	-0.2	-0.6	0.4
$\psi(°)$	90.8	90.8	0.0

4.1.6 Results

Once the parameters ${}^{\mathbf{Pat}}\mathbf{T}_{\mathbf{CT}}$, ${}^{\mathbf{O}}\mathbf{T}_{\mathbf{Pat}}$, ${}^{\mathbf{P}}\mathbf{T}_{\mathbf{O}}$, and ${}^{\mathbf{U}}\mathbf{T}_{\mathbf{P}}$ were known, all 9 ultrasound volumes of the phantom were registered to its CT image using

$$ {}^{\mathbf{U}}\mathbf{T}_{\mathbf{CT}} = {}^{\mathbf{U}}\mathbf{T}_{\mathbf{P}}\,{}^{\mathbf{P}}\mathbf{T}_{\mathbf{O}}\,{}^{\mathbf{O}}\mathbf{T}_{\mathbf{Pat}}\,{}^{\mathbf{Pat}}\mathbf{T}_{\mathbf{CT}}. \tag{4.7} $$

The registration result for one of the ultrasound volumes is shown in Figure 4.11.

To validate the accuracy of the registration results, the locations of the 43 aluminium BBs embedded inside the phantom were identified in both CT and ultrasound. In CT, the image centroid of the ROI surrounding the BB was taken to be its location. In ultrasound, thresholding was necessary to remove the comet-tail artifacts extending from the BBs along the scan line of the image. Then, similar to CT, the filtered image centroid in a ROI surrounding the BB was taken as its location. Images of BB locations in CT and ultrasound are shown in Figure 4.12.

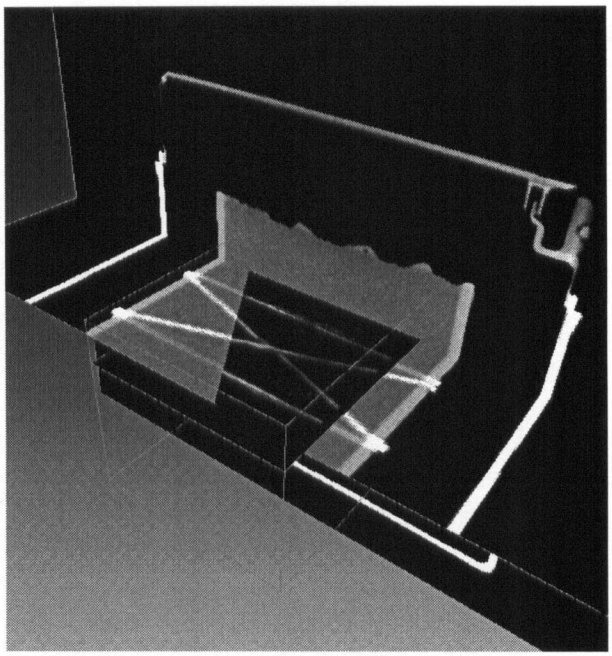

Figure 4.11: The registration result for one ultrasound volume of the phantom and its CT image. A coronal slice of the ultrasound volume is shown with a coronal slice of the CT volume in approximately the same position. One of the IXI-wire configurations inside the phantom used for calibrating the ultrasound probe can be seen in both CT and ultrasound.

The difference in corresponding BB locations in registered CT and ultrasound images is defined as the TRE. In the 9 ultrasound volumes of the phantom, a total of 151 BBs were able to be identified (multiple views of the 43 BBs inside the phantom were obtained). Some of these BBs are located laterally far away from the center of the ultrasound volume, where the ultrasound resolution is poorer compared to the center. An example is shown in Figure 4.12(c). Therefore, greater uncertainty in the calculated ultrasound locations of these BBs can be expected. As a result, separate TRE results have been compiled using BBs located less than half the volume width ($35mm$) away from the volume center laterally, and vice versa. These results are summarised in Table 4.3.

To further illustrate the impact of BB location in the ultrasound volume on TRE measurement, a plot of the TRE as a function of BB location is shown for all 151 identified targets in the 9 ultrasound volumes in Figure 4.13.

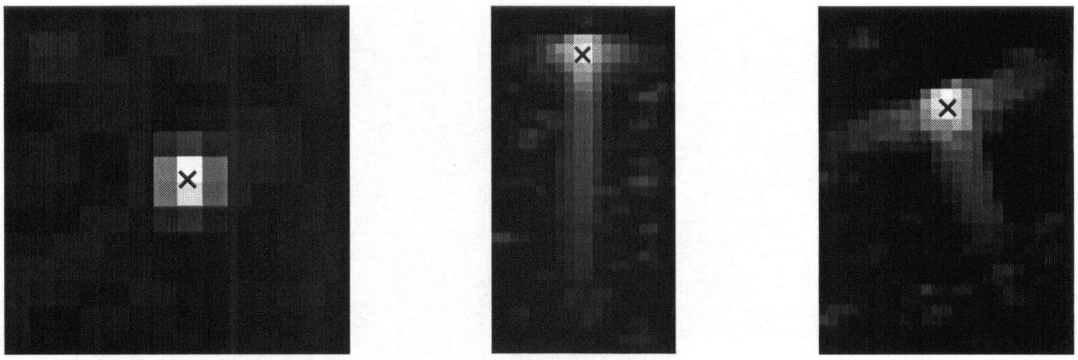

(a) BB appearance in CT

(b) BB appearance near ultrasound volume center

(c) BB appearance near ultrasound volume edge

Figure 4.12: Axial slices of CT and ultrasound in a ROI surrounding a BB. The appearance of two BBs, one near the center of the ultrasound volume, and one near its edge are shown to illustrate the non-uniform nature of spatial resolution within the ultrasound volume. Note the distinctive comet-tail artifact in the ultrasound images. This is caused by multiple reverberations (or 'ringing') of the sound wave inside the metal BB before returning to the transducer, resulting in delayed echoes. This artifact is removed by thresholding before calculating the BB location in the ultrasound image. The calculated BB center in CT and ultrasound is marked with the cross. Note that these points are projected onto the image plane for display.

Table 4.3: CT to ultrasound TRE results. All 9 ultrasound volumes of the phantom were registered to a single CT volume. All the BBs observed in the 9 ultrasound scans were identified and compared to their CT locations. Results for BBs located less than $35mm$ away from the center of the ultrasound volume laterally and further than $35mm$ away have been collated separately. The mean TRE in each axis of the phantom coordinate system are shown, along with the standard deviation. The RMS value of the overall 3D TRE is also shown.

BB Location	N	$\overline{TRE}(mm)$			$\sigma_{TRE}(mm)$			RMS 3D $TRE(mm)$
		x	y	z	x	y	z	
$< 35mm$	65	-0.50	-0.12	0.23	0.53	0.70	0.33	1.09
$> 35mm$	86	-0.55	-0.04	-0.37	1.35	1.23	0.47	2.00
All BBs	151	-0.53	-0.07	-0.11	1.08	1.04	0.51	1.67

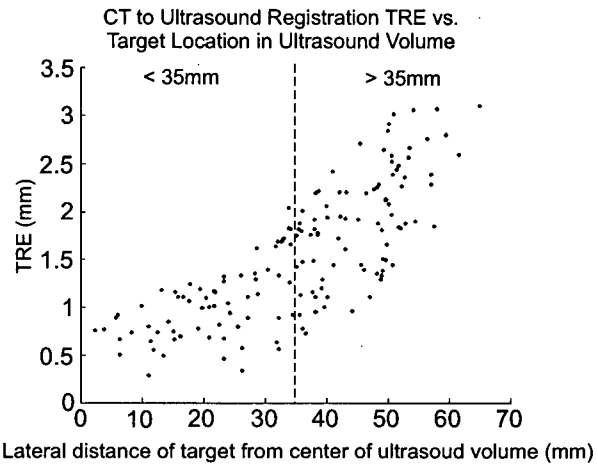

Figure 4.13: CT to ultrasound TRE for all 151 identified targets in 9 ultrasound volumes as a function of target location in the ultrasound volume. The dividing line separating targets less and more than $35mm$ away from the center of the ultrasound volume is shown.

4.1.7 Discussion

The mean TRE values in all 3 axis directions shown in Table 4.3 are very small and indicate the lack of systematic registration errors between the CT and ultrasound volumes. It can clearly be seen from Table 4.3 and Figure 4.13 that as the target location from the center of the ultrasound volume increases, the measured 3D TRE increases. This positive correlation was expected since the spatial resolution of the ultrasound image decreases laterally from the volume center, resulting in higher uncertainty in the calculated BB location.

This is further supported by the substantial increase in the TRE standard deviation in the x and y directions for the group of BBs further away from the ultrasound volume center in Table 4.3. The x and y directions of the phantom coordinate system roughly corresponds to the coronal (lateral) plane of the ultrasound volume, the direction in which the spatial resolution degrades most significantly.

The above observations suggest that the TRE for BBs located near the edge of the ultrasound volume is significantly affected by errors in finding the BB locations in ultrasound. These errors arise solely from the validation procedure, and are not indicative of the actual CT and ultrasound

registration accuracy. Thus, if only centrally located BBs (laterally within $35mm$ of the ultrasound volume center) are used to calculate the registration accuracy, a RMS 3D TRE of $1.09mm$ is obtained.

The main sources of error in the CT to ultrasound registration process includes calculating the IRED locations in CT and ultrasound probe calibration. As shown previously, an average residual error of $0.70mm$ remained in the calculated CT IRED locations. This is mainly due to errors in estimating the axis of symmetry of the IRED, resulting in an average angle of 25° between this axis and the vector from the IRED centroid to its OPTOTRAK measured location. However, the effect of this error on the registration accuracy of ${}^{\mathbf{Pat}}\mathbf{T}_{\mathbf{CT}}$ can be reduced if its direction is uniformly distributed, and a sufficient number of IREDs are used to establish point correspondences. As shown in Table 4.2, compared to using lead BBs as fiducials, a very similar result for the transformation ${}^{\mathbf{Pat}}\mathbf{T}_{\mathbf{CT}}$ was able to be obtained using the 8 IRED markers, despite the presence of the residual calibration errors in the IRED CT locations. Nevertheless, it may be desirable in future applications to attach the IRED to a larger base object to form a single marker in order to improve their visibility in CT and aid the determination of their orientation.

The other major source of error in the CT to ultrasound registration process is ultrasound probe calibration error. The accuracy of the probe calibration process used here has been previously evaluated by Poon and Rohling [87] using the same ultrasound system and probe. By comparing the 3D location of a small spherical bead identified in ultrasound images acquired using the OPTOTRAK tracked probe, and its location measured directly using OPTOTRAK, the point accuracy of the probe calibration parameter was measured. Over 100 trials, the RMS point accuracy was found to be $2.15mm$. These results would seem to suggest that the BB locations identified from ultrasound images in this experiment should also be subject to an error of this magnitude. However, the RMS 3D TRE for this experiment was $1.09mm$. This figure also includes errors in finding the CT to phantom registration ${}^{\mathbf{Pat}}\mathbf{T}_{\mathbf{CT}}$ and identifying the BB locations in CT.

One possible explanation for this discrepancy may be that the location of the bead used for Poon's calibration point accuracy tests is more difficult to identify accurately in ultrasound compared to the BBs used in this experiment. Another difference is the ultrasound coupling material used for the tests in [87] and in this experiment. This material was water at $37°C$ in the

former, and an agar-based gel in the latter. Water at $37°C$ is known to have a speed of sound of $1524ms^{-1}$ [9], which represents a 1% error from the $1540ms^{-1}$ assumed by the ultrasound machine. In comparison, the gel's measured speed of sound is $1533ms^{-1}$, which corresponds to an error of 0.5%. Thus, geometric distortion in ultrasound images of water at $37°C$ due to speed of sound error will be twice the magnitude of such errors for the gel.

A similar experiment to the one presented in this section was performed by Tomé *et al.* [101] to evaluate the accuracy of the SonArray ultrasound patient positioning system. In this study, an array of passive infra-red markers was attached to a phantom which was subsequently imaged using CT. The locations of spherical targets inside the phantom were identified with respect to the marker locations in the CT scan. This phantom was then positioned inside the radiotherapy treatment room using a CCD camera system similar to the OPTOTRAK, and the passive infra-red markers. By using the CT locations of the targets in conjunction with optical measurement of the phantom position, the target locations in the treatment room were determined. Finally, these target locations were verified by ultrasound scanning using the SonArray.

The experiment as described above essentially reproduces the CT to ultrasound registration scheme tested in this section, previously shown on Figure 4.1. One difference is that passive infra-red markers are attached to the phantom instead of IREDs, which are bigger and spherical instead of disk-shaped. Tomé *et al.* reported ultrasound target localisation errors of $0.2 \pm 0.7mm$, $0.9 \pm 0.6mm$, and $0.6 \pm 1.0mm$ (mean $\pm$ standard deviation) along each orthogonal axis. These figures are comparable with the TRE values of $-0.50 \pm 0.53mm$, $-0.12 \pm 0.70mm$, and $0.23 \pm 0.33mm$ in each axis[1] obtained in this experiment.

As mentioned previously, the CT to ultrasound registration results obtained in this experiment represent the lower bound accuracy of this technique, since it is tested on a rigid, incompressible phantom. With real patients, additional error in calculating the transformation between the simulation CT and the patient coordinates, ${}^{\mathbf{Pat}}\mathbf{T}_{\mathbf{CT}}$, will occur as a result of non-rigid patient motion between the simulation CT and ultrasound scans. With non-rigid motion, estimating ${}^{\mathbf{Pat}}\mathbf{T}_{\mathbf{CT}}$ by least-squares minimisation of corresponding IRED marker positions in CT and patient coordinates will no longer be optimal. More accurate registration results in this case may potentially be

[1]The axis directions used by Tomé *et al.* [101] and herein to report errors are arbitrary.

obtained using a modified optimisation criterion, such as the one proposed in [62].

The number and arrangement of the IRED markers on the patient will also have an effect on the accuracy of the transformation ${}^{\mathbf{Pat}}\mathbf{T}_{\mathbf{CT}}$, and hence the overall registration accuracy between the simulation CT and ultrasound. As the number of IRED markers used as point correspondences increases, the effect of measurement error associated with each marker location on the accuracy of ${}^{\mathbf{Pat}}\mathbf{T}_{\mathbf{CT}}$ will reduce, provided measurement errors are Gaussian distributed. Thus, in general, the accuracy of ${}^{\mathbf{Pat}}\mathbf{T}_{\mathbf{CT}}$ should improve with increased number of IRED markers. However, in practice, only a limited number of markers can be used due to time constraints in attaching them to the patient during the simulation session. In addition to the number of markers that can be placed, they also must be positioned on the patient close to the target location while not obstructing access by the ultrasound probe. In [65], Liu *et al.* showed that an optimal marker arrangement exists which can maximise the resulting TRE at a specific target location. It may be worthwhile to investigate whether the methods used in this study could be adapted to guide IRED marker placement in the proposed patient positioning system.

4.2 Ultrasound to Ultrasound Registration

One key difference between the proposed ultrasound patient positioning system and current existing systems is the method used to compare the anatomy at the time of treatment to the anatomy at simulation. In existing systems, this comparison is performed by matching contours of relevant features manually segmented from CT or ultrasound images. In the BAT and SonArray, contour registration is done manually, while the Restitu is believed to use the ICP algorithm [7].

As mentioned earlier, one of the advantages of the proposed system is that dedicated 3D ultrasound probes are used to acquire images of the patient. This allows image volumes with consistent size, slice spacing, and spatial resolution to be obtained. In contrast, volumes reconstructed from the freehand ultrasound acquisition technique employed by other systems are variable in their field of view and spatial resolution. The improvement in ultrasound image quality in the proposed system may enable automatic pixel-intensity based methods to be used in registering ultrasound volumes. This approach has a number of advantages compared to the contour-based registration

technique used by other systems:

- Segmentation of the image is not required.
- Manual input to perform the registration is not required.
- Registration accuracy is independent of user skill.
- Registration uses all available information from the image.

To investigate whether automatic pixel-intensity based registration of 3D ultrasound volumes of real anatomy is possible, an experiment is performed using ultrasound data acquired from the neck of a volunteer. The goal of this experiment is to simply demonstrate that 3D ultrasound images acquired using dedicated 3D probes of the Voluson 730 are of sufficient quality for this approach to be feasible. The algorithm used to perform the registration is of general applicability and has not been optimised for this particular application. The details and results of this experiment are described in the subsections below.

4.2.1 Experimental Methods

Multiple ultrasound volumes of a volunteer's neck are collected using the Voluson 730 while tracking the ultrasound probe position during imaging with the OPTOTRAK. The relationship between the coordinate systems involved during the data acquisition process are shown in Figure 4.14. The coordinate systems of two of the acquired ultrasound neck images are represented by U and U', and the corresponding probe positions by P and P'. The transformations from the probe positions to the the OPTOTRAK, ${}^{\mathbf{O}}\mathbf{T}_{\mathbf{P}}$ and ${}^{\mathbf{P}'}\mathbf{T}_{\mathbf{O}}$, are given by OPTOTRAK measurement, while the parameters ${}^{\mathbf{P}}\mathbf{T}_{\mathbf{U}}$ and ${}^{\mathbf{U}'}\mathbf{T}_{\mathbf{P}'}$ are determined through the probe calibration procedure. Therefore, the only unknown parameter is the transformation between the two ultrasound images, ${}^{\mathbf{U}'}\mathbf{T}_{\mathbf{U}}$.

The transformation ${}^{\mathbf{U}'}\mathbf{T}_{\mathbf{U}}$ is estimated by an automatic pixel-intensity based image registration algorithm (described later in Section 4.2.2) using the images U and U' as inputs. In addition, it is calculated independently using OPTOTRAK measurements of the probe position during

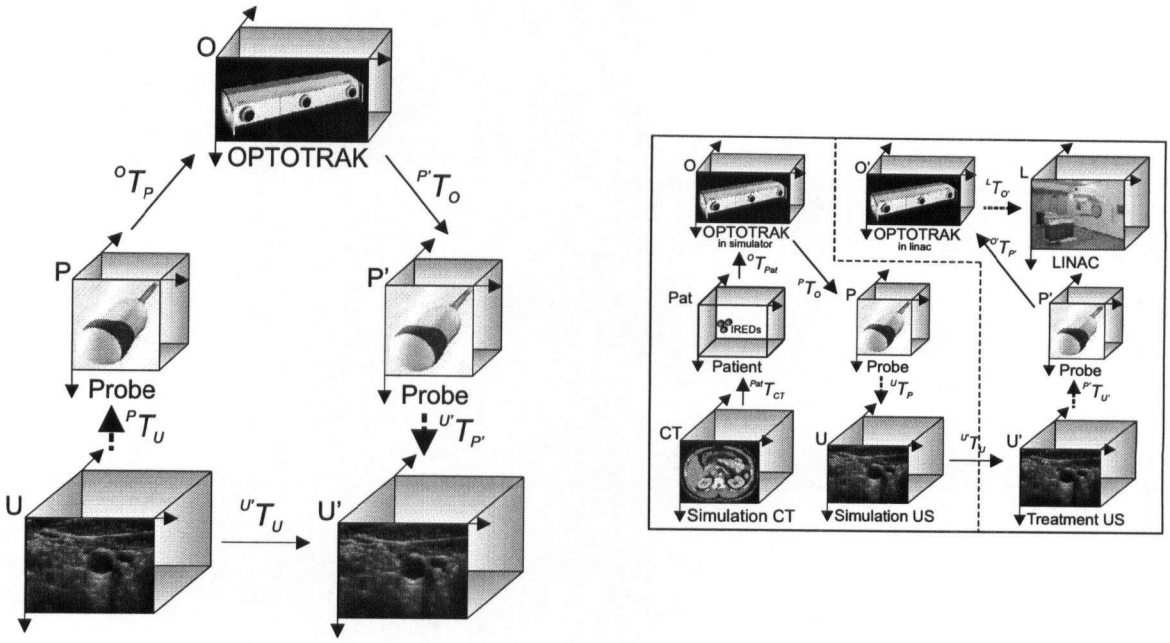

Figure 4.14: Coordinate systems involved during acquisition of multiple ultrasound scans of the immobilised subject. Two different ultrasound images are denoted by U and U', and the probe positions during acquisition by P and P'. Note that since the same probe is used to acquire all the images, ${}^{\mathbf{U'}}\mathbf{T_{P'}} = ({}^{\mathbf{P}}\mathbf{T_U})^{-1}$. As a reminder of how the ultrasound-to-ultrasound image registration step ${}^{\mathbf{U'}}\mathbf{T_U}$ fit into the overall proposed patient positioning scheme, the entire series of coordinate transforms used by the proposed system, previously shown in Figure 3.5, is displayed in the right-hand panel.

acquisition of the two images, and the following equation:

$$ {}^{\mathbf{U'}}\mathbf{T_U} = {}^{\mathbf{U'}}\mathbf{T_{P'}}\,{}^{\mathbf{P'}}\mathbf{T_O}\,{}^{\mathbf{O}}\mathbf{T_P}\,{}^{\mathbf{P}}\mathbf{T_U} \qquad \text{where } {}^{\mathbf{U'}}\mathbf{T_{P'}} = ({}^{\mathbf{P}}\mathbf{T_U})^{-1}. \tag{4.8} $$

Provided the subject being scanned remains motionless with respect to the OPTOTRAK coordinates between acquisition of the two ultrasound images, OPTOTRAK measurements should give a reliable 'ground truth' for the transformation ${}^{\mathbf{U'}}\mathbf{T_U}$. Thus, by comparing the results for ${}^{\mathbf{U'}}\mathbf{T_U}$ obtained using the automatic pixel-intensity based image registration algorithm, and using OPTOTRAK measurements, the accuracy of the image registration algorithm can be found.

In addition to neck images, ultrasound images of the probe calibration phantom previously described in Section 4.1.3 are acquired immediately after scanning the volunteer. This effectively

ensures that the probe calibration parameter, ${}^{\mathbf{P}}\mathbf{T}_{\mathbf{U}}$, is the same for both the phantom and neck images. The same image registration algorithm used to register the neck images is then used to find ${}^{\mathbf{U}'}\mathbf{T}_{\mathbf{U}}$ for the phantom images. As for images of the neck, the accuracy of the image registration algorithm for the phantom images is assessed by comparison with the ground truth calculated using OPTOTRAK measurements. Since ultrasound images of the calibration phantom contain clear features with high contrast, they represent idealised input for the image registration algorithm. Thus, the difference in performance of the image registration algorithm for idealised input (phantom images), and realistic input (neck images), can be assessed.

4.2.2 Image Registration Algorithm

Pixel-intensity based registration methods calculate the transformation between two images using pixel values alone. Theoretically, these are the most flexible of registration methods since they do not reduce images to relatively sparse extracted features, but utilise all available information to perform registration [70]. Another attractive feature of pixel-intensity based registration algorithms is that the amount of preprocessing and user-interaction required is much less than other methods, making them relatively easy to automate [28].

Suppose two images to be registered are denoted by A and B, and the sets of pixels in these images are $\{A(i)\}$ and $\{B(i)\}$. Furthermore, let A be designated as the reference image, and B as the model image. The goal of image registration is to find the transformation $\mathcal{T}$ which maximises the similarity between the reference image A and the transformed model image $B' = \mathcal{T}(B)$ in some sense.

In pixel-intensity based registration algorithms, a cost function is defined which measures the degree of similarity between two images, and $\mathcal{T}$ is calculated iteratively by optimising this function over the parameter space of $\mathcal{T}$. The cost function is evaluated for the set of pixels in the overlapping region of A and B' ($A \cap B'$). Since this is a function of $\mathcal{T}$, $A \cap B'$ changes as the algorithm iterates.

For registering 3D ultrasound images acquired using the Voluson 730 in this experiment, $\mathcal{T}$ is restricted to rigid-body transformations for simplicity. The parameter space of $\mathcal{T}$ therefore

contains 6 variables: 3 translations and 3 rotations. Although human tissue is non-rigid and subject to deformation in reality, rigid-body transformations have been most frequently used in image registration and is a valid first-order approximation in many applications [70].

The cost function used by the registration algorithm in this experiment is the image correlation coefficient (CC), defined in Equation 4.9. This similarity measure is invariant to linear changes in the image intensity and thus will be the ideal similarity measure if the intensities in images A and B are linearly related [28]. This requirement is sufficiently met in intramodality image registration, and makes the CC suitable for use in such applications. In ultrasound imaging in particular, the CC has been used extensively for speckle tracking applications such as blood flow estimation, elasticity imaging and spatial compounding, where images are registered using correlation of speckle noise patterns [10, 36, 98]. In IGRT, CC-based algorithms have been used to automatically register simulation and treatment CT images of the prostate [85, 100].

Algorithm 1 Correlation Coefficient

For images A and B with pixels i, find the transformation $\mathcal{T}$ to maximise:

$$CC = \frac{\sum_i (A(i) - \bar{A})(B(i) - \bar{B'})}{\sqrt{\sum_i (A(i) - \bar{A})^2 \sum_i (B'(i) - \bar{B'})^2}} \qquad \forall i \in A \cap B', \tag{4.9}$$

where $\bar{A}$ and $\bar{B'}$ are the mean values of pixels in image A and the transformed image B, respectively.

The commercially available software package Amira was used to perform CC-based registration of 3D ultrasound images in this experiment. This particular implementation uses a gradient-descent technique to optimise the CC. To speed up processing, a multi-resolution optimisation strategy is employed, whereby registration is first performed on a coarse resampling of the images, and the result successively refined by registration at finer resolutions.

4.2.3 Data Acquisition

The volunteer was asked to lie still in a supine position on a couch as shown in Figure 4.15. The head of the volunteer was immobilised using a thermoplastic mask typically used for positioning patients undergoing radiotherapy treatment of head-and-neck tumours. The mask was custom-

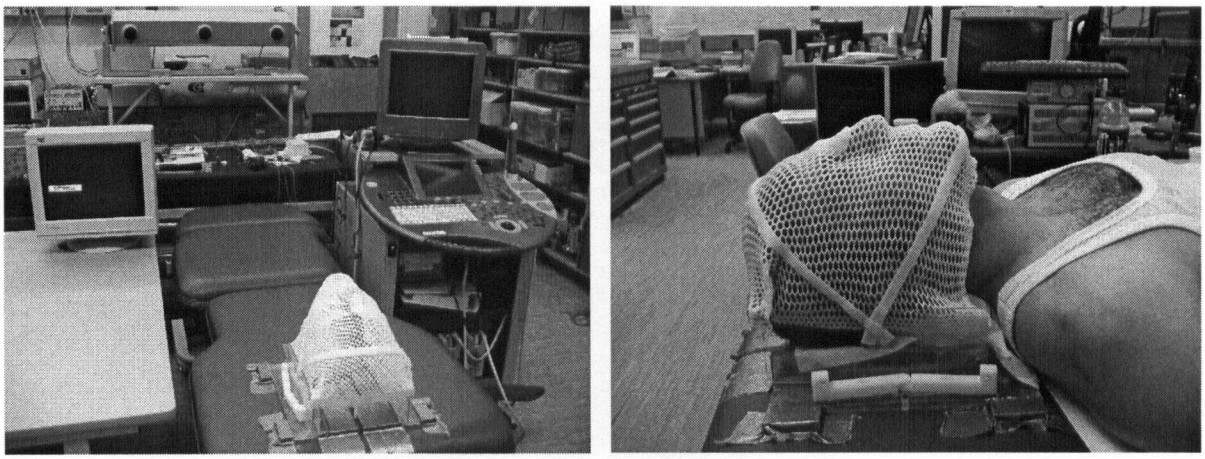

(a) (b)

Figure 4.15: Experimental set-up for acquiring ultrasound images from the neck of a volunteer. The couch is positioned in front of the OPTOTRAK and beside the Voluson 730 ultrasound machine (a). The subject is immobilised by a thermoplastic mask moulded to the contour of his face and clamped to a base plate during image acquisition (b). Note that in this image the clamp was released. The lower portion of the neck was left exposed to allow access by the ultrasound probe.

molded to the contours of the volunteer's face and head by radiation therapists at the British Columbia Cancer Agency (BCCA). This mask was secured to a base plate supplied by the BCCA by clamps on each side of the base plate. A standard polyurethane head support was rigidly fixed to the base plate to ensure proper positioning of the subject's head and neck.

The immobilised subject's neck was imaged using the small-parts RSP5-12 3D ultrasound probe of the Voluson 730. During image acquisition, minimal downward force was placed on the subject's neck by the ultrasound probe to ensure that tissue deformation is not significant. The volunteer was also asked to hold his breath during the 3D image acquisition process, which takes approximately 2 seconds. During ultrasound imaging, the position of the ultrasound probe was recorded by the OPTOTRAK.

In total, 17 images of the same side of the volunteer's neck was collected in a period of approximately 11 minutes. The ultrasound probe position was varied between scans, but the thyroid, common carotid artery (CCA), and internal jugular vein (IJV) were always kept within the image field-of-view. The image dimensions are $38 \times 27 \times 49mm$ with a voxel size of $0.25mm$.

Immediately after the neck images were obtained, the same probe was used to image the probe calibration phantom described in Section 4.1.1, shown previously in Figure 4.2. By using the technique described in Section 4.1.3, the calibration parameters were calculated for this probe. Twenty additional images of the phantom not used for calibration purposes were taken with varying probe positions so that the image registration algorithm could also be tested on the phantom images.

4.2.4 Results

A single slice of one of the acquired volumetric ultrasound images of the neck is shown in Figure 4.16. Features such as thyroid, CCA, and IJV are readily visible. The presence of numerous features in the image and its high spatial resolution are favorable factors for the application of pixel-intensity based image registration.

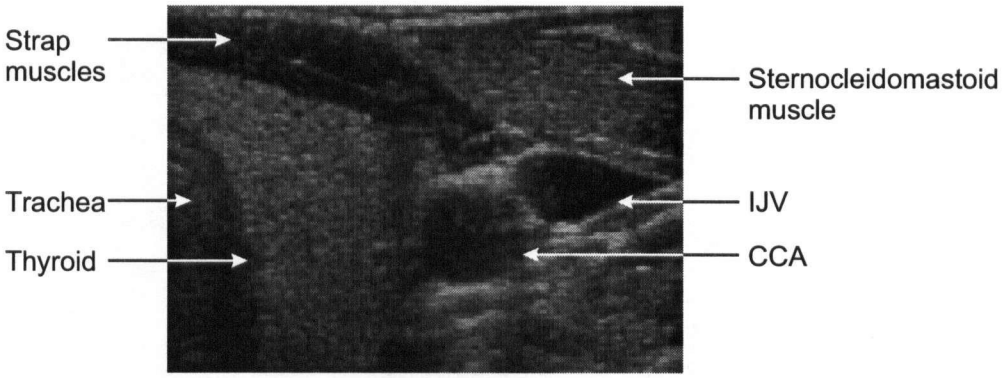

Figure 4.16: Axial slice of a volumetric ultrasound image of the neck acquired from the volunteer. Visible anatomic features are marked by arrows.

In total, 45 ultrasound-to-ultrasound image registrations were performed in Amira using different image pairs from the 17 scans collected. In each registration, one image was chosen as the reference, and one as the model to be transformed. To initialise the algorithm, the transformation

${}^{U'}\mathbf{T}_U$ determined from OPTOTRAK measurements using Equation 4.8 was applied to the model image as the starting point for registration. The image registration algorithm was performed on a dual-processor PC with two $2.8GHz$ Intel Xeon processors and $1GB$ of RAM. Results were typically obtained within one minute.

The image registration results for one pair of ultrasound volumes is shown in Figure 4.17. It can be seen that a residual misalignment between the images exists when the transformation ${}^{U'}\mathbf{T}_U$ determined from OPTOTRAK data is used to initialise the algorithm. After applying the image registration algorithm, an improvement in alignment can be observed, especially near the IJV. In all 45 registrations performed, the OPTOTRAK determined values for ${}^{U'}\mathbf{T}_U$ resulted in obvious misalignments between images. After performing image registration, a discernable improvement in image alignment was observed in 44 out of the 45 cases.

The final result for ${}^{U'}\mathbf{T}_U$ given by the registration algorithm was compared to its value deter-

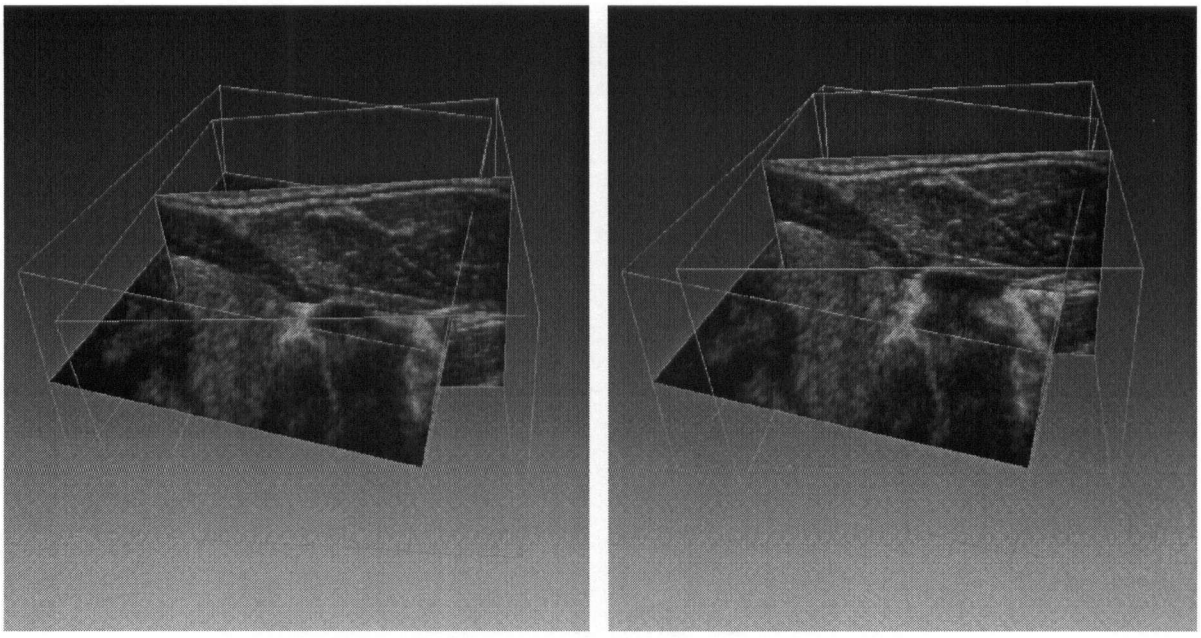

(a) Initial state (b) Final registration result

Figure 4.17: Automatic pixel-intensity based image registration results in Amira for one pair of neck ultrasound volumes. One coronal slice of the reference volume, and an axial slice of the model volume are shown. The algorithm was initialised using ${}^{U'}\mathbf{T}_U$ determined from OPTOTRAK measurements (a). The final result of the registration is shown in (b).

mined from OPTOTRAK measurements by using the so-called 'average corner-point deviation' (ACD). This is the average position deviation of the eight corner-points of the model ultrasound volume from their initial positions at the start of image registration to their final positions at the end of registration, as illustrated in Figure 4.18. A low value for ACD would therefore indicate good agreement between OPTOTRAK measurements and image registration results for ${}^{U'}\mathbf{T}_U$. The ACD values for all the registrations performed on the neck images are summarised in Table 4.4.

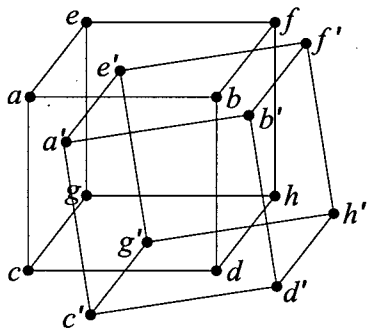

$$ACD = \tfrac{1}{8}(\|a' - a\| + \|b' - b\| + \|c' - c\| + \|d' - d\| + \|e' - e\| + \|f' - f\| + \|g' - g\|)$$

Figure 4.18: The ACD is the average displacement of the corner points of the model ultrasound volume from their initial positions $a - g$ determined from OPTOTRAK measurements, to their final positions $a' - g'$ after image registration in Amira.

The performance of the image registration algorithm was also tested on images of the calibration phantom acquired immediately after the neck images. As mentioned previously, images of the phantom contained clear features in the form of IXI-wires, which should aid the performance of the algorithm. In total, 37 registrations were performed using different pairs of the 20 phantom images. As previously, the OPTOTRAK determined transformation ${}^{U'}\mathbf{T}_U$ was used to initialise the algorithm. The results for one pair of images is shown in Figure 4.19. Image registration was found to improve the alignment of the phantom images in most cases. In other instances, the difference between the final registration result and the OPTOTRAK determined transformation were insignificant. A summary of the ACD values for all the phantom registrations is given in Table 4.4.

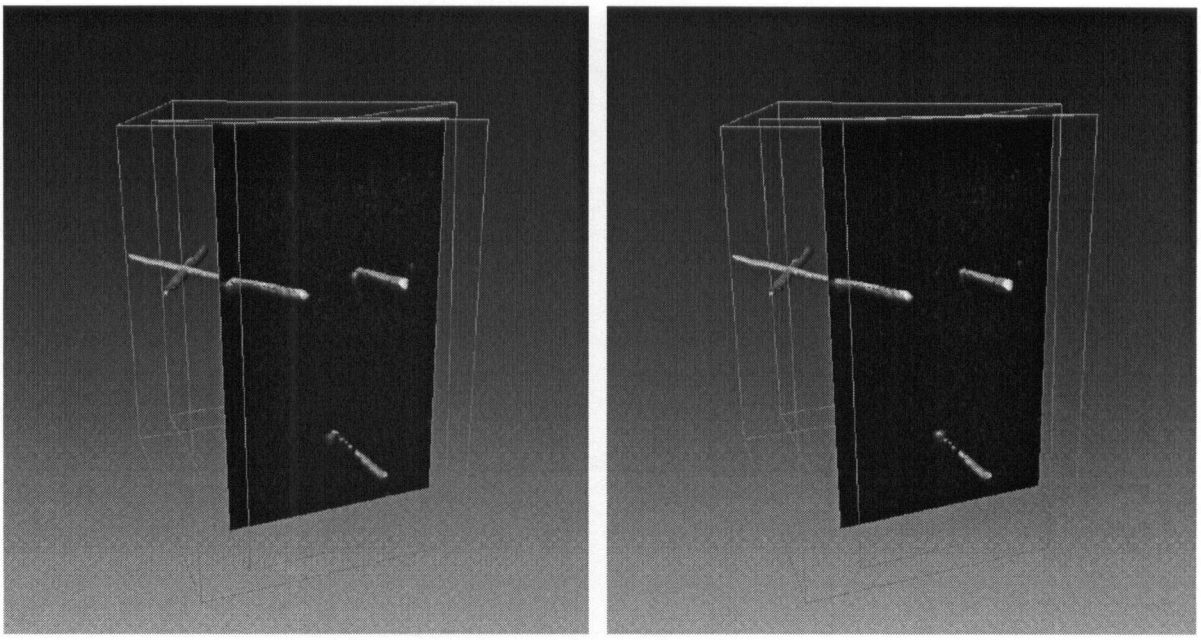

(a) Initial state (b) Final registration result

Figure 4.19: Automatic pixel-intensity based image registration results in Amira for one pair of calibration phantom ultrasound volumes. For ease of visualisation, an iso-surface rendering of the IXI-wires in the reference volume is shown, while an axial slice of the model volume is displayed. The algorithm was initialised using ${}^{U'}\mathbf{T}_U$ determined from OPTOTRAK measurements (a). The final result of the registration is shown in (b).

Table 4.4: A summary of ACD values for all image registrations performed on ultrasound volumes of the neck, and ultrasound volumes of the calibration phantom.

Image Type	Max ACD (mm)	Min ACD (mm)	RMS ACD (mm)
neck	5.62	1.16	2.83
phantom	1.25	0.25	0.62

4.2.5 Discussion

It was originally anticipated that OPTOTRAK measurements of the ultrasound probe position during image acquisition would provide a reliable estimate, or 'ground truth', for the registration result ${}^{U'}\mathbf{T}_U$ between the captured ultrasound images. The ACD would therefore be a measure of the image registration algorithm accuracy. However, this did not prove to be the case for the neck

images, as all the OPTOTRAK determined registration results were observed to have residual misalignment. Therefore, the pixel-intensity based image registration results were qualitatively assessed by visual inspection.

Indeed, a number of factors contribute to the ACD measure besides simply image registration error from Amira. Inaccuracies in determining any one of the transformations ${}^{\mathbf{P}}\mathbf{T}_{\mathbf{U}}$, ${}^{\mathbf{P}'}\mathbf{T}_{\mathbf{O}}$, or ${}^{\mathbf{O}}\mathbf{T}_{\mathbf{P}}$ in Equation 4.8 will result in an error in the calculation of ${}^{\mathbf{U}'}\mathbf{T}_{\mathbf{U}}$ from OPTOTRAK measurements, and hence most likely increasing the ACD. Recall that the OPTOTRAK measurement error is sub-millimeter [47]. Thus, the largest source of error amongst these terms is likely to be the probe calibration matrix ${}^{\mathbf{P}}\mathbf{T}_{\mathbf{U}}$, determined from the probe calibration procedure described in Section 4.1.3.

Another source of error in determining the registration result from OPTOTRAK measurements using Equation 4.8 is the implicit assumption that the subject being imaged remains stationary with respect to the OPTOTRAK. While every effort was made to ensure that the volunteer was immobilised during ultrasound scanning, elimination of all motion is not possible. The pulse of the volunteer is one motion which cannot be avoided. The contraction/expansion of the CCA during rapid heart beat is strong enough to cause significant deformation of the surrounding tissue. Breathing and swallowing can also cause movement of anatomy in the neck region. Finally, the pressure exerted by the ultrasound probe itself during imaging can can cause deformation of the underlying tissue.

The major sources of error contributing to the ACD measure for registering both the neck and phantom images are shown in Table 4.5. The RMS value of ACD for all the phantom images registered was $0.62mm$. This shows good consistency between the transformation ${}^{\mathbf{U}'}\mathbf{T}_{\mathbf{U}}$ derived from OPTOTRAK measurements and by image registration. The small ACD value indicates that both the probe calibration error and image registration error are low for the phantom images.

For the neck images, the RMS ACD was $2.83mm$, significantly higher than for the phantom. The same probe calibration parameters were used for both the phantom and neck images, so the probe calibration error cannot account for the increase in ACD for the latter. Therefore, the two remaining significant sources of error, subject movement and image registration, must be the causes for the increase.

Table 4.5: The major error sources contributing to the ACD measure for registration of neck and phantom ultrasound images. A tick indicates a contributing factor to the ACD result, and a cross a non-contributing factor.

Error source	neck	phantom
Subject movement	✓	✗
Probe calibration	✓	✓
Image registration	✓	✓

The image registration algorithm used to register images of the neck and phantom is the same. The accuracy of the registration result, however, will depend on the content of the images. The phantom images represent a somewhat idealised input for the image registration algorithm, since it contains clear features with high contrast, and low noise. The neck images, on the other hand, have less contrast and contains more noise. In addition, the phantom is incompressible, while the features in the neck images are deformable. Recall that the registration parameter ${}^{U'}\mathbf{T}_{U}$ is limited to 6 DOF rigid-body motion in the image registration algorithm. Therefore, it is reasonable to expect a degradation in the accuracy of the image registration results for the neck images. Unfortunately, the absence of ground truth for the registration results means that it is not possible to make a quantitative assessment of how much the increase in the ACD value for neck images is due to image registration error, and how much is due to subject motion.

While this section has shown that automatic pixel-intensity based registration of 3D ultrasound images acquired using the Voluson 730 is practically feasible, a number of issues must be considered before such as method can be implemented to position patients for radiotherapy treatment. One requirement of all iterative optimisation algorithms is an initial guess for the solution. In this experiment, the solution for the image registration parameter ${}^{U'}\mathbf{T}_{U}$ was estimated using OPTOTRAK measurements. Can an initial guess for ${}^{U'}\mathbf{T}_{U}$ be formulated in the framework of the patient positioning system proposed in this thesis?

It turns out that the answer is yes. Recall from Section 3.3.2 that the chain of transformations from the simulation CT coordinates to the LINAC coordinates on the day of treatment is given

by:

$$^{L}\mathbf{T}_{CT} = {}^{L}\mathbf{T}_{O'}{}^{O'}\mathbf{T}_{P'}{}^{P'}\mathbf{T}_{U'}{}^{U'}\mathbf{T}_{U}{}^{U}\mathbf{T}_{P}{}^{P}\mathbf{T}_{O}{}^{O}\mathbf{T}_{Pat}{}^{Pat}\mathbf{T}_{CT}. \tag{4.10}$$

Let $\{\underline{o}_{iso}, \underline{C}_{iso}\}$ be the local coordinates of the treatment plan, with the origin at the planned isocenter. Additionally, let $^{CT}\mathbf{T}_{iso}$ be the transformation from CT to treatment plan coordinates defined during treatment planning. Then, the treatment plan coordinates with respect to the LINAC at the time of treatment is given by:

$$^{L}\mathbf{T}_{iso} = {}^{L}\mathbf{T}_{O'}{}^{O'}\mathbf{T}_{P'}{}^{P'}\mathbf{T}_{U'}{}^{U'}\mathbf{T}_{U}{}^{U}\mathbf{T}_{P}{}^{P}\mathbf{T}_{O}{}^{O}\mathbf{T}_{Pat}{}^{Pat}\mathbf{T}_{CT}{}^{CT}\mathbf{T}_{iso}. \tag{4.11}$$

The goal of the patient positioning system is to ensure that the coordinate system of the LINAC and the treatment plan are coincident at the time of treatment. An appropriate initial guess for $^{U'}\mathbf{T}_{U}$ can be formed by assuming that the patient is initially in perfect alignment for treatment. That is,

$$^{L}\mathbf{T}_{iso} = I \qquad \text{where } I = \text{the identity matrix.} \tag{4.12}$$

Then, Equation 4.11 becomes

$$I = {}^{L}\mathbf{T}_{O'}{}^{O'}\mathbf{T}_{P'}{}^{P'}\mathbf{T}_{U'}{}^{U'}\mathbf{T}_{U}{}^{U}\mathbf{T}_{P}{}^{P}\mathbf{T}_{O}{}^{O}\mathbf{T}_{Pat}{}^{Pat}\mathbf{T}_{CT}{}^{CT}\mathbf{T}_{iso} \tag{4.13}$$

and rearranging gives the initial guess for image registration as

$$^{U'}\mathbf{T}_{U} = {}^{U'}\mathbf{T}_{P'}{}^{P'}\mathbf{T}_{O'}{}^{O'}\mathbf{T}_{L}{}^{iso}\mathbf{T}_{CT}{}^{CT}\mathbf{T}_{Pat}{}^{Pat}\mathbf{T}_{O}{}^{O}\mathbf{T}_{P}{}^{P}\mathbf{T}_{U}. \tag{4.14}$$

An important concept in automatic pixel-intensity based image registration algorithms is the notion of *capture range* [28]. It is the portion of the parameter space of $\mathcal{T}$ in which the local optimum of the cost function corresponds to the correct registration solution. Thus, provided the initial guess for $\mathcal{T}$ is within the capture range, the registration can be expected to converge to the correct solution.

The capture range depends on the field-of-view, and the content of the images being registered, and cannot be determined *a priori*. Nevertheless, it is important to have an estimate of the image

registration algorithm's capture range in order to know the conditions under which it can be expected to work and fail. This would be useful, for example, in determining the tolerance on how accurate the patient needs to be positioned inside the LINAC initially so that the initial guess for ${}^{U'}\mathbf{T}_{U}$ from Equation 4.14 lies within the registration algorithm capture range. Rough guidelines can be established once the specific treatment site and ultrasound imaging parameters are known by registering typical images using different initial guesses. In the treatment work-flow, it is also important that the radiation therapist visually verifies the automatically registered ultrasound images to prevent incorrect solutions outside the capture range to be used to position the patient.

The registration algorithm used in this experiment has not been optimised for the specific task of registering neck images. Thus, there is ample room for customisation of the algorithm once a specific treatment site is chosen. Simple site specific preprocessing could include thresholding to remove irrelevant anatomical features or extracting smaller regions of interest. Non-rigid image registration techniques such as those being developed for neurosurgery [27] could also be explored to improve registration accuracy.

The series of neck ultrasound images used for this experiment was acquired over a short period of time. However, in clinical use of the proposed ultrasound patient positioning system, ultrasound images of the patient acquired over a period of different days, and indeed weeks, have to be registered. If appreciable changes in the anatomy occurs in that period (e.g., due to tumour response to the treatment), then it may no longer be sensible (or possible) to attempt to register the ultrasound taken during latter treatment sessions to the original simulation ultrasound image. In this case, it may be still possible to use an ultrasound image taken during an intermediate treatment session, when changes in the anatomy are not so significant, as a surrogate simulation scan with which to compare ultrasound images from latter treatment sessions.

Chapter 5

Whole System Test

In order to evaluate the overall accuracy of the proposed ultrasound patient positioning system, an experiment was devised whereby the entire process of radiation therapy, from simulation to irradiation, was carried out on a phantom. This phantom represents an idealised patient in behaving as a rigid-body, being incompressible, and having features which can be clearly observed in ultrasound without significant artifacts or noise. Therefore, this experiment attempts to measure the lower bound positioning accuracy of the proposed system.

The proposed treatment protocol outlined in Section 3.2 was used to position the phantom inside the LINAC for 'treatment' after initial set-up using alignment lasers. In addition, a freehand ultrasound image acquisition method, combined with contour-based ultrasound image registration, was also used to determine the target locations. This freehand localisation technique is similar to existing ultrasound patient positioning systems, especially the Restitu. Although many aspects still differ, it allows direct comparison of the target localisation accuracy resulting from the use of dedicated 3D ultrasound probes versus freehand imaging for acquiring anatomical data. Furthermore, an additional independent measurement of the target location prior to treatment was provided by OPTOTRAK. Thus, the positioning accuracy was able to be compared among four different target localisation methods: the proposed 3D ultrasound-based system, a freehand ultrasound approach, direct OPTOTRAK measurement, and the conventional method of using lasers and set-up marks.

The novel aspect of this experiment is that a unique method is used to verify the accuracy of the phantom positioning results inside the LINAC. After the phantom is positioned for treatment by the proposed system, it is irradiated using a predefined treatment plan. The actual dose delivered to the phantom by the LINAC is recorded by a radiosensitive gel in the phantom. By observing changes in the gel's physical property, the location of the delivered dose can be determined and

compared to the planned dose, thereby closing the loop on the entire treatment process using the proposed system. No previous work on other IGRT systems has shown this type of validation. The details and results of this experiment are presented in the following sections.

5.1 Phantom Construction

The phantom used in this experiment is shown in Figure 5.1. It consists of a plastic box containing the ultrasound tissue-equivalent gel previously described in Section 4.1.1. Embedded inside this background material are 3 balloons containing the same gel plus a high concentration of cellulose to act as hyperechogenic features in ultrasound. Unlike the phantom used throughout Chapter 4, wires were not utilised as ultrasound features for this phantom because the small number of contour points available from thin wires do not mimic contours of real organs needed for image registration in the freehand ultrasound localisation method. On the side of the box, 8 IREDs are attached to facilitate CT to ultrasound registration as described in Section 4.1. The contents of this box are scanned by ultrasound to position the phantom.

Four bottles of radiosensitive gel are securely strapped to the side of the box. This gel is a type of polymer gel dosimeter developed for verifying 3D dose distributions produced by 3D-CRT and IMRT radiotherapy systems in quality assurance tests [71]. These consist of a gel matrix doped with a monomer which polymerise and cross-link when exposed to ionising radiation, thus storing 3D dose information permanently. Various forms of polymer gels have been studied, and new variants are in development in an active field of research [13, 22, 39, 102]. These studies have shown that polymer gels possess many desirable properties for 3D dosimetry, including accuracy, temporal stability, and approximate linear response to dose.

Most types of polymer gels must be manufactured in a sealed environment in the absence of oxygen, as its presence in the gel inhibits the polymerisation reaction. Therefore, the dosimeter gel formulation chosen for this study is a 'normoxic' type which can be readily manufactured under atmospheric conditions. This gel was described by Jirasek *et al.* in [51]. It consists of (by weight) 5% gelatin (300 Bloom, Sigma-Aldrich), 89% distilled water (Anachemia), 3% acrylamide as the monomer, 3% bis-acrylamide as the cross-linker (both of electrophoresis grade, Sigma-

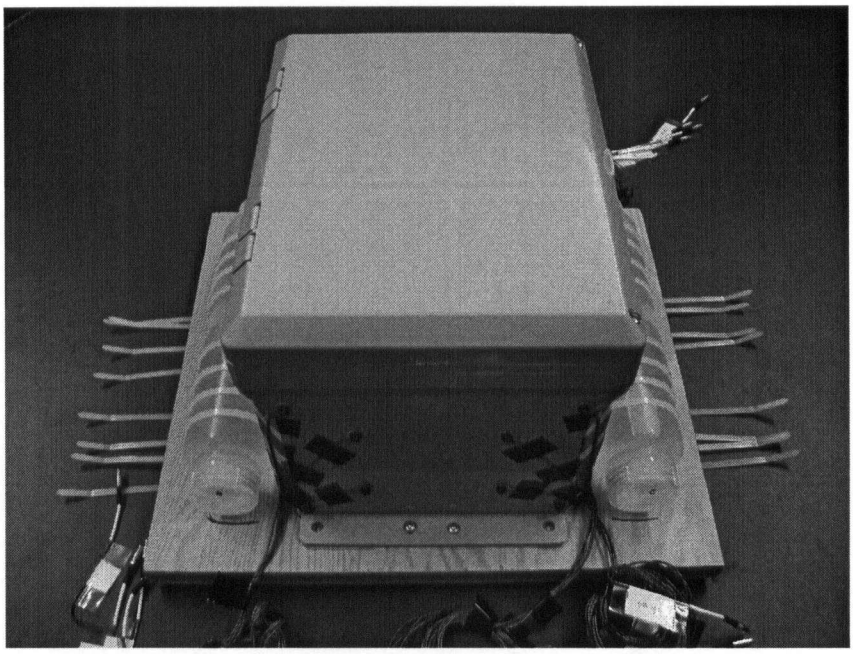

Figure 5.1: The phantom used to test the overall 3D ultrasound patient positioning system accuracy. The large box contains the ultrasound tissue-equivalent material and 3 embedded balloons to act as features in ultrasound. The lid of the box can be opened to allow access by the ultrasound probe. The four polypropylene NALGENE® bottles contain the polymer gel and are rigidly secured to the wooden base with cable ties. Eight IRED markers are taped to the side wall of the box.

Aldrich), and $5mM$ tetrakis hydroxymethyl phosphonium chloride (THPC) (Sigma-Aldrich) as an anti-oxidant. Details of its manufacture is given in Appendix B.

Although the addition of THPC to the polymer gel inhibits the presence of free oxygen molecules in the gel, its anti-oxidant properties decreases with time as more oxygen diffuses into the gel from outside its container walls. Therefore, on the day of treatment, fresh bottles of polymer gels were made approximately 6 hours prior to irradiation and were strapped to the wooden base of the phantom in place of the gels rendered inactive by prolonged exposure to oxygen. This time frame was shown in [51] to give stable dose response results. The need to replace the polymer gel is one reason why it could not be housed together with the ultrasound tissue-equivalent gel in the same plastic box of the phantom. The polymer gel also happens to be toxic, and impractical to manufacture in large quantities, unlike the tissue-equivalent material.

5.2 Target Localisation Methods

The four target localisation methods tested in this experiment are described in the following subsections.

5.2.1 3D Ultrasound Localisation

The proposed treatment protocol for 3D ultrasound-based patient positioning outlined in Section 3.2 was used to position the phantom inside the LINAC for irradiation. The main steps performed are summarised here.

Simulation 3D Ultrasound Acquisition

For convenience, the simulation 3D ultrasound scan of the phantom was acquired in the lab instead of inside the CT simulator, as for a real patient. The 3D RAB4-8P probe of the Voluson 730 was used for imaging, while both the probe and phantom positions were tracked simultaneously by OPTOTRAK. The 3D image field-of-view covered the three hyperechogenic balloons inside the box, as shown in Figure 5.2. In addition, the ultrasound probe calibration matrix ${}^{U}\mathbf{T_P}$ was determined using the method described in Section 4.1.3.

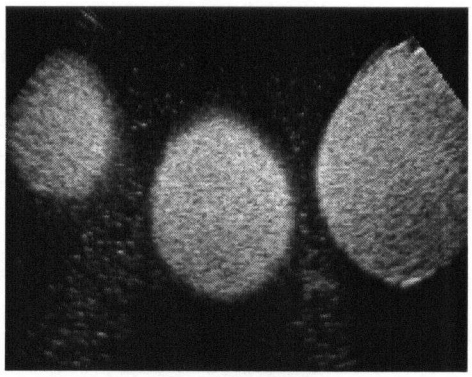

Figure 5.2: An axial slice of the simulation 3D ultrasound volume of the phantom showing the 3 hyperechogenic balloons.

Simulation CT to 3D Ultrasound Registration

After ultrasound scanning, the phantom was transported to the BCCA and the simulation CT was performed using a PQ5000 CT simulator (Picker International). Before the CT scan, alignment laser projections on three sides of the plastic box were marked to facilitate initial repositioning of the phantom during treatment, and 3 lead BBs were placed at the laser crosshairs as CT reference points, as for a real patient. CT imaging parameters were $1.5mm$ slice thickness, $1s$ scan time, $130kV$ tube voltage, and $200mA$ tube current.

The simulation CT and 3D ultrasound scans of the phantom were registered using the methods previously described in Section 4.1. The IREDs taped to the side of the plastic box were used to find the transformation between the CT volume and the OPTOTRAK coordinates during ultrasound scanning. The 3D ultrasound volume was transformed into the same OPTOTRAK coordinates using OPTOTRAK measurements of the probe position during scanning, and the probe calibration matrix. The registered volumes are shown in Figure 5.3.

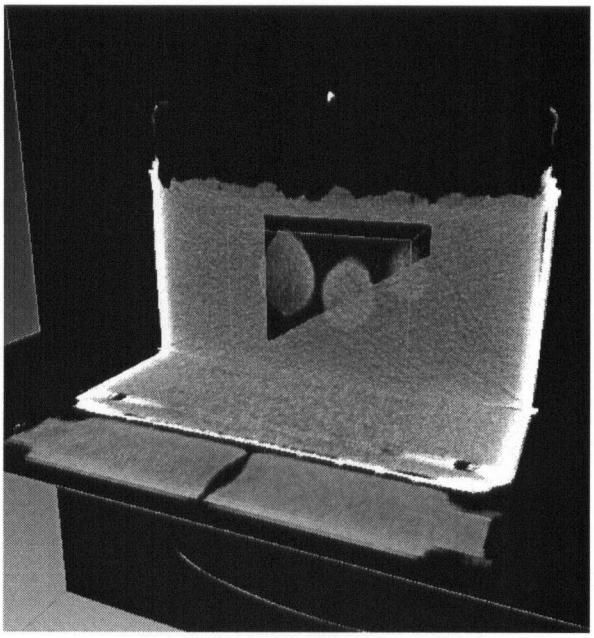

Figure 5.3: Simulation CT and 3D ultrasound image registration results for the phantom. An axial slice of the 3D ultrasound volume in approximately the same position as one axial slice of the CT volume is displayed.

3D Ultrasound-to-Ultrasound Registration

To find the target location in the LINAC immediately before irradiation, another 3D ultrasound of the phantom is acquired while the probe position is tracked by an OPTOTRAK inside the treatment room. This treatment ultrasound was automatically registered with the simulation ultrasound using the pixel-intensity based image registration algorithm described in Section 4.2.2. The target location in the LINAC coordinates was then determined by substituting the result of this registration, ${}^{U'}\mathbf{T}_{U}$, into Equation 3.11.

5.2.2 Freehand Ultrasound Localisation

In addition to testing the overall accuracy of the 3D ultrasound-based patient positioning method proposed in this thesis, a freehand 3D image acquisition technique was implemented using the Voluson 730 and the OPTOTRAK. This enables the phantom position inside the LINAC to be independently determined using freehand ultrasound data and a contour-based image registration method, similar to existing ultrasound patient positioning systems. Although the phantom is ultimately positioned for treatment using the proposed 3D ultrasound-based method in this experiment, off-line retrospective comparison of target localisation results of this method and the freehand ultrasound-based localisation technique is still possible.

The freehand localisation approach implemented for this experiment uses the exact same series of coordinate transforms as the proposed system, previously shown in Figure 3.5 and Equation 3.11, for localising the target inside the LINAC. However, the simulation and treatment ultrasound images are not acquired using the automatic 3D ultrasound imaging technique like the proposed system. Instead, freehand ultrasound is used. In addition, simulation and treatment ultrasound volumes are not registered using automatic pixel-intensity based registration methods as in the proposed system. Rather, the iterative closest point (ICP) algorithm is used to register the contours of features extracted from the freehand images. Details of the freehand localisation method used is given below.

Freehand Image Acquisition Method

Recall from Section 3.1.1 that freehand 3D images are reconstructed from multiple 2D slices at different locations acquired by manually translating a 2D ultrasound probe. To acquire freehand data using the Voluson 730, the central slice of the volumes acquired continuously as the probe is translated were used as the 2D images forming the freehand data set.

In order to reconstruct volumetric information from the 2D image slices collected during freehand acquisition, their positions relative to each other must be known. This can be calculated by using OPTOTRAK measurements of the probe position during acquisition of each image and knowledge of the probe calibration parameter, which can be determined using the methods outlined in Section 4.1.3. However, recall from Section 3.1.3 that the start of ultrasound imaging and OPTOTRAK measurement in the combined system is not synchronised. This did not pose a problem when the probe remained still during normal automatic 3D image acquisition with the system. However, with probe movement, OPTOTRAK measurements of its position must be synchronised with image acquisition times. Therefore, a calibration procedure is performed to measure the delay from the start of OPTOTRAK measurement to the start of Voluson 730 image acquisition.

OPTOTRAK and Ultrasound Data Synchronisation

The time delay between the initiation of OPTOTRAK and ultrasound data collection in the combined system was measured by applying the freehand scanning technique described in the previous subsection on an ultrasound fetus phantom. However, instead of translating the probe at constant speed across the surface of the phantom as usual, an impulse motion was generated by first keeping the probe stationary, and then applying a short rapid translation.

In the series of acquired images, the first displaying a change in image content was identified as corresponding to the start of the probe translation, as shown in Figure 5.4. If this image is the $N_U{}^{th}$ frame in the sequence of images acquired, and the frame rate is f_U, then the time delay Δt_U

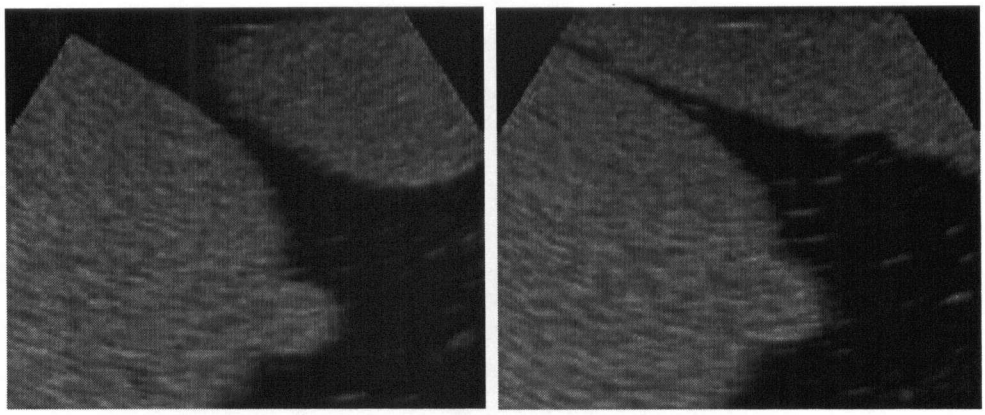

Figure 5.4: Determining the start time of the probe translation from acquired ultrasound images. The image acquired while the probe was initially stationary is shown in (a). The first image to display a significant change in content from (a) corresponding to the start of probe movement is shown in (b).

between the start of ultrasound acquisition and application of the translation impulse is given by

$$\Delta t_U = \frac{N_U - 1}{f_U}. \tag{5.1}$$

During freehand imaging, the OPTOTRAK is capable of measuring the probe position at a sampling rate of $f_O = 250Hz$. The probe displacement between measurement samples can be calculated, and plotted as shown in Figure 5.5. The sample number N_O corresponding to the start of the translation impulse is estimated using double-thresholding. If N_l is the sample number when the probe displacement reaches the low threshold D_l, and N_h is the sample number when the high threshold D_h is reached, then N_O can be estimated using linear extrapolation to find the zero-crossing of the line connecting (N_l, D_l) and (N_h, D_h). The time delay Δt_O between the start of OPTOTRAK acquisition and application of the translation impulse is given by

$$\Delta t_O = \frac{N_O - 1}{f_O}. \tag{5.2}$$

Finally, the time delay needed to synchronise OPTOTRAK and ultrasound data Δt_{sync} can be

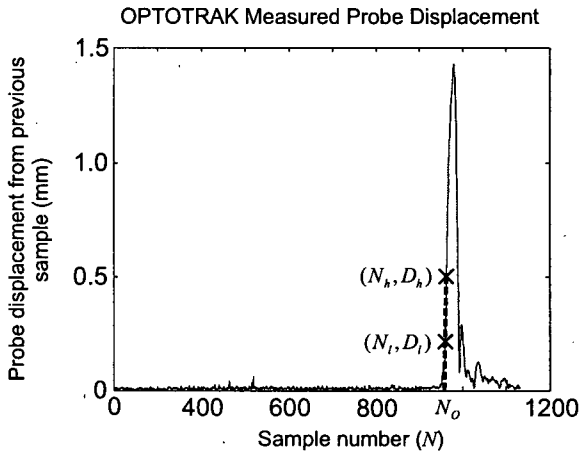

Figure 5.5: Determining the start time of the probe translation from OPTOTRAK measurement of probe position. The OPTOTRAK measurement sample N_O corresponding to the start of probe movement is detected using two thresholds $D_l = 0.2mm$ and $D_h = 0.5mm$ on the measured probe displacement, and linear extrapolation.

calculated using

$$\Delta t_{sync} = \Delta t_O - \Delta t_U. \tag{5.3}$$

Measurement of the synchronisation delay Δt_{sync} was repeated 20 times, and a value of $1.5 \pm 0.1s$ (mean $\pm$ standard deviation) was obtained. The mean value of 1.5 seconds was used to synchronise OPTOTRAK and ultrasound data for freehand image acquisition throughout the remainder of this chapter.

Simulation Freehand Ultrasound Acquisition

As for the simulation 3D ultrasound, a freehand ultrasound of the phantom was acquired in the lab prior to CT imaging using the methods described in the preceding Sections. Relevant features in each slice of the freehand data set were contoured to facilitate contour-based image registration. In the phantom images, the edges of the balloons could be easily extracted by thresholding, as shown in Figure 5.6(a). The extracted contour points on each slice were then transformed to a common coordinate system using OPOTOTRAK measurements of the probe position during freehand scanning and probe calibration parameters determined *a priori*. The

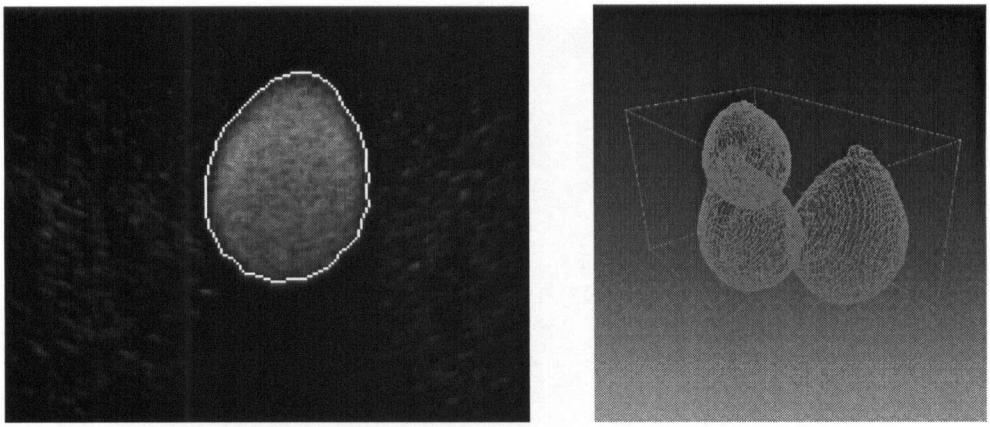

(a) Contour extracted from one slice (b) Contours from all slices

Figure 5.6: One slice of the simulation freehand ultrasound volume of the phantom (a). The contour extracted from this slice is shown as the white outline. The contours extracted from all the slices in this data set transformed to a common coordinate system (b).

common coordinate system chosen was the coordinates of the first slice. The extracted contours from all slices of the simulation freehand ultrasound volume in this common coordinate system are shown in Figure 5.6(b).

Simulation CT to Freehand Ultrasound Registration

As for the simulation 3D ultrasound, the simulation freehand ultrasound was registered to the CT image of the phantom using the methods previously described in Section 4.1. The result of this registration is shown in Figure 5.7.

Freehand Ultrasound-to-Ultrasound Registration

The target location inside the LINAC can be found by acquiring another freehand ultrasound of the phantom inside the treatment room. Like the proposed 3D ultrasound-based method, this treatment freehand image is registered to the simulation freehand ultrasound using a rigid-body transformation. Unlike the proposed system, however, this transformation is found by registering the contours extracted from the two freehand ultrasound images using the ICP algorithm [7]. The result of this registration can then be used in Equation 3.11 to find the target location.

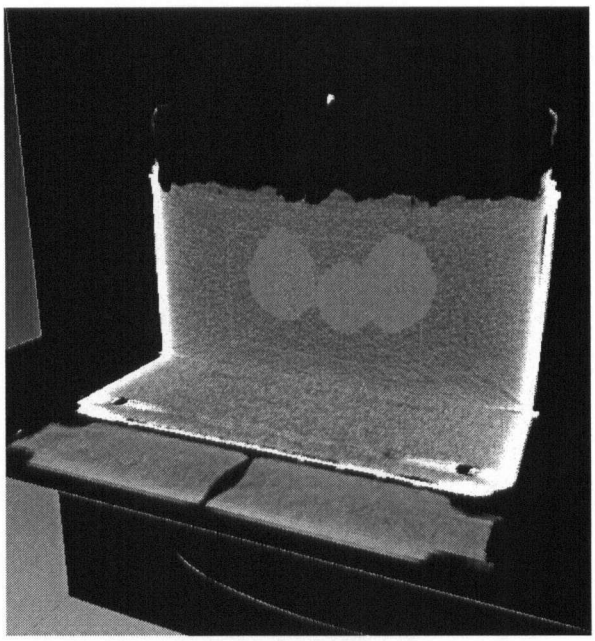

Figure 5.7: Simulation CT and freehand ultrasound image registration results for the phantom. The contours extracted from the freehand ultrasound data is overlayed on top of the registered CT volume.

5.2.3 OPTOTRAK Localisation

If the IRED markers placed on the phantom for the simulation CT are left intact for the treatment session, then the OPTOTRAK used to measure the ultrasound probe position inside the LINAC can also be used to directly measure the phantom position prior to treatment delivery. This provides yet another independent target localisation technique which can be compared to the proposed 3D ultrasound-based method in offline analysis.

To localise the target isocenter inside the LINAC using this approach, the series of coordinate transforms in Figure 5.8 and in the following equation can be applied:

$$^{\mathbf{L}}\mathbf{x}_{\mathbf{iso}} = {}^{\mathbf{L}}\mathbf{T}_{\mathbf{O'}}{}^{\mathbf{O'}}\mathbf{T}_{\mathbf{Pat}}{}^{\mathbf{Pat}}\mathbf{T}_{\mathbf{CT}}{}^{\mathbf{CT}}\mathbf{x}_{\mathbf{iso}}. \tag{5.4}$$

The terms $^{\mathbf{L}}\mathbf{T}_{\mathbf{O'}}$ and $^{\mathbf{Pat}}\mathbf{T}_{\mathbf{CT}}$ in Equation 5.4 are the transformation between the LINAC and OPTOTRAK coordinates, and the transformation between the patient and the simulation CT

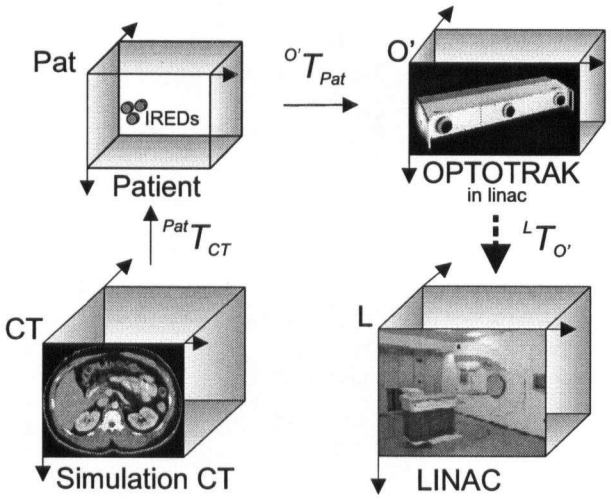

Figure 5.8: The series of coordinate transformations from the simulation CT to the LINAC coordinates when using the OPTOTRAK to directly measure the patient (in this case a phantom) position in the treatment room.

coordinates, as defined previously in Section 3.3.2 for the proposed system. The term $^{O'}\mathbf{T}_{\mathbf{Pat}}$ is simply the direct measurement of the patient (in this case the phantom) position inside the LINAC with OPTOTRAK.

Comparing Equation 5.4 with the proposed ultrasound target localisation method summarised in Equation 3.11, it can be seen that direct OPTOTRAK measurement of the phantom position inside the LINAC allows the chain of transformations

$$^{O'}\mathbf{T}_{\mathbf{Pat}} = {}^{O'}\mathbf{T}_{P'}{}^{P'}\mathbf{T}_{U'}{}^{U'}\mathbf{T}_{U}{}^{U}\mathbf{T}_{P}{}^{P}\mathbf{T}_{O}{}^{O}\mathbf{T}_{\mathbf{Pat}} \tag{5.5}$$

in the proposed system to be circumvented. With fewer terms required to calculate $^{L}\mathbf{x}_{\mathbf{iso}}$, and therefore fewer sources of error, it is reasonable to expect that direct OPTOTRAK localisation of the target should be more accurate than using the proposed ultrasound system. Of course, it should be noted that direct OPTOTRAK measurement of the phantom position is only possible in this experiment as the IRED markers are not removed from the phantom after simulation. In clinical practice, the IREDs will not be able to be permanently fixed to the body of a real patient, and would be removed after the simulation procedure.

5.2.4 Laser Positioning

The conventional radiotherapy method of employing alignment lasers in the treatment room and set-up marks on the patient was also used to position the phantom for treatment in this experiment. As for the freehand ultrasound and OPTOTRAK target localisation methods, the accuracy of this technique can be assessed by comparing positioning results with those obtained using the proposed 3D ultrasound-based system, once the accuracy of the latter is determined by polymer gel dosimetry.

To facilitate laser positioning in the treatment room, recall from Section 5.2.1 that the three laser crosshair locations on the phantom before simulation CT imaging were marked. At the exact same locations, three BBs were placed to establish a reference for these points in the simulation CT image. These three points are used to define the treatment plan coordinate system as illustrated in Figure 5.9. The position of targets are then defined with respect to these coordinates.

To position the phantom for irradiation of any target location, the set-up markings placed on the phantom during simulation are first aligned with the laser projections in the treatment room. This brings the treatment plan coordinates into alignment with the LINAC coordinates. To bring the target location into alignment with the LINAC isocenter (LINAC coordinate system origin), the offset to the target location is implemented by manually shifting the motor-driven couch.

5.3 Treatment Planning

Treatment planning was performed using the Eclipse treatment planning system (Varian Medical Systems) at the BCCA. The locations of the three lead BBs placed on the phantom during simulation were identified in the simulation CT to establish the treatment plan coordinate system as was depicted in Figure 5.9.

Four target isocenters were selected in the treatment plan, each near the middle of one of the four polymer gel bottles. This requires the phantom to be positioned four times during treatment so that each target can be irradiated in succession. Note that these target locations are substantially outside the field of view of the simulation ultrasound image, which only covers

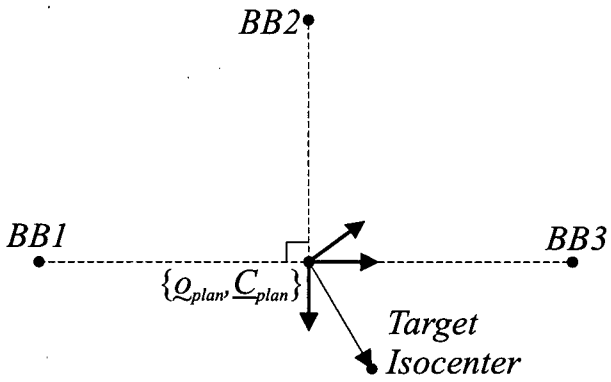

Figure 5.9: Establishment of the treatment plan coordinates using the three BBs (BB1-3) placed on the box of the phantom during simulation. The treatment plan origin is taken to be the intersection of the orthogonal lines connecting the three BB locations. Any target isocenter can be defined relative to this origin by an offset vector.

the balloons inside the box on the phantom. Ideally, the targets should be directly imaged with ultrasound. However, as mentioned in Section 5.1, it was impractical to incorporate the polymer gel into the part of the phantom which is able to be imaged by ultrasound. Nevertheless, locating the targets using ultrasound images of the box remains valid, since the target locations are defined consistently with respect to fiducials on the box, which is a rigid, permanent part of the phantom.

Each isocenter was given the three field treatment plan shown in Figure 5.10. The $6MV$ beam from the Varian 21EX LINAC in treatment unit 6 at the BCCA was chosen to deliver the radiation with square fields $30mm$ wide. The 3D dose distribution produced by the fields are calculated by the treatment planning algorithm based on a number of input parameters. These include beam geometry, energy, phantom geometry, electron density of the phantom material (estimated from CT pixel intensity), and measured properties of the beam produced by the selected treatment unit. The calculated dose distribution is displayed as isodose contours in Figure 5.10. The dose value of the contours are given relative to the dose delivered to the isocenter, which is set to a value of $15Gy$.

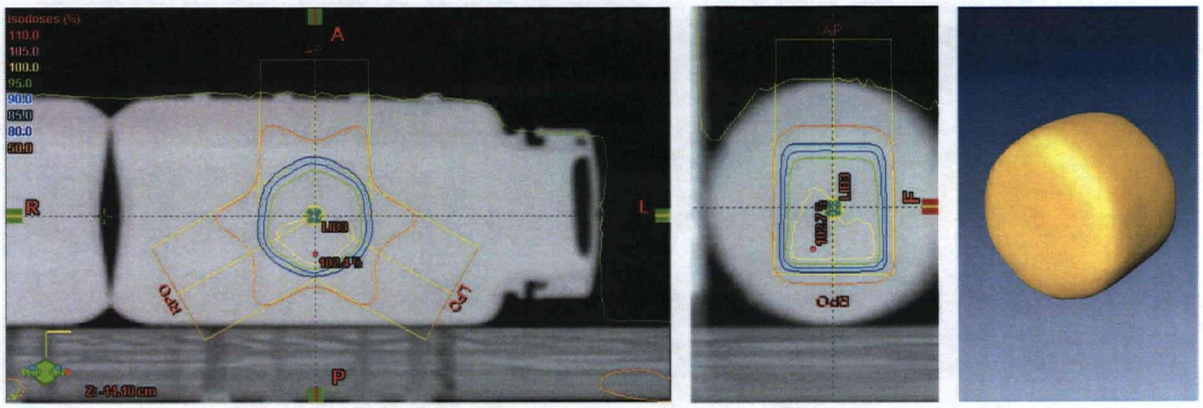

(a) Axial view (b) Sagittal view (c) 80% Isodose

Figure 5.10: The planned field arrangement and calculated dose distribution surrounding one of the target isocenters. Orthogonal cross-sections of the simulation CT are shown in (a) and (b). The planned isocenter is labelled 'LIB3', and the three fields AP (anterior-posterior), LPO and RPO (left- and right-posterior-oblique, respectively) are shown. Also displayed is the calculated isodose distribution produced by the fields. The 3D 80% isodose contour is rendered in (c) by Amira.

5.4 OPTOTRAK to LINAC Calibration

On the day of treatment, the Voluson and OPTOTRAK were set-up inside the treatment room. The OPTOTRAK was positioned against the wall at the inferior end of the LINAC couch while the Voluson was placed at the side of the couch. Before treatment, the transformation between the OPTOTRAK coordinate system and the LINAC coordinate system (${}^{L}\mathbf{T}_{O'}$ in Figure 3.5) was determined through a calibration procedure.

The calibration procedure involved placing the phantom on the couch so that the alignment lasers in the treatment room were projected onto the sides of the box on the phantom. The lateral and overhead laser crosshair locations on the box, which correspond to points on the LINAC axes, were measured with respect to the OPTOTRAK coordinates by using the stylus previously shown in Figure 4.3. By shifting the couch and hence the point of intersection between the lasers and the box walls, 10 different points along the left-right and anterior-posterior axes of the LINAC coordinate system were sampled using the stylus. These points were projected onto the least-squares fit plane and the best fit orthogonal axes were solved using constrained least-squares, as

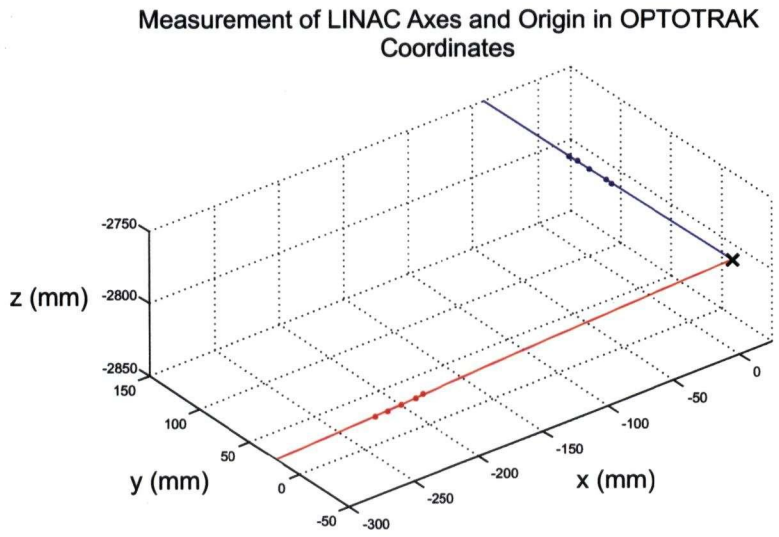

Figure 5.11: Determining the LINAC axes in the OPTOTRAK coordinate system. The location of 5 points along the LINAC left-right (x) axis in the OPTOTRAK coordinate system are measured using the stylus and plotted as the blue dots. Similarly, the measured locations of 5 points along the anterior-posterior (y) axis are plotted as red dots. The least-squares fit for the orthogonal x and y axes of the LINAC are plotted as the blue and red lines, respectively. The LINAC z axis is found by taking the cross-product of unit vectors in the x and y directions. The point of intersection of the all the axes is taken as location of the LINAC origin, or isocenter, and is marked by the black cross.

shown in Figure 5.11. These axes were taken to be the LINAC frame in OPTOTRAK coordinates, and their point of intersection the LINAC origin, or isocenter location.

5.5 Treatment Delivery

For each target, the following steps were performed to administer the planned dose:

1. The phantom is initially positioned by aligning set-up marks made during simulation with lines projected onto the phantom by the laser alignment system inside the treatment room. This brings the LINAC isocenter into alignment with the treatment plan origin.

2. The offset from the plan origin to the desired target isocenter is implemented using manual controls to shift the motor-driven couch. This brings the LINAC isocenter into alignment with the planned isocenter.

3. Due to inaccuracies in positioning the phantom using set-up marks and the alignment lasers, the LINAC isocenter will not be precisely at the planned isocenter location. To exacerbate this effect, an artificial set-up error is introduced by shifting the couch. The additional simulated set-up error induced for the four targets are shown in Table 5.1.

4. To reposition the phantom correctly for treatment, the lid of the box was opened and the treatment ultrasound scan of the balloons acquired. In addition, a freehand ultrasound volume was taken for off-line analysis.

5. The treatment ultrasound volume is automatically registered with the simulation ultrasound in Amira using the pixel-intensity based registration algorithm described in Section 4.2.2.

6. The series of transformations in Equation 3.11 is used to find the location of the target isocenter in the LINAC coordinate system, ${}^{\mathbf{L}}\mathbf{x}_{\mathbf{iso}}$. The required shift to bring the planned isocenter to the same location as the LINAC isocenter is then given by $-{}^{L}\underline{x}_{iso}$.

7. The required shift $-{}^{L}\underline{x}_{iso}$ determined using the proposed ultrasound positioning system is implemented by translating the couch. The LINAC isocenter should now be in alignment with the planned isocenter.

8. As a final consistency check, the position of the phantom is measured directly by the OPTOTRAK using the IREDs still attached to the wall of the box. This measurement is recorded for off-line analysis.

9. The three field treatment plan is delivered by the LINAC to the polymer gel bottle.

Table 5.1: The couch shift used to simulate a set-up error after the target is positioned at isocenter using alignment lasers. Shifts are given in LINAC coordinates.

Target	Simulated Error (mm)		
	x	y	z
1	5	0	0
2	0	0	5
3	0	5	0
4	5	5	5

5.6 Gel Response Readout

Upon exposure to radiation, the polymerisation reaction causes a density change to occur in the polymer gel [103]. This density change can be detected by CT imaging as a change in the gel's Hounsfield unit (HU), or CT pixel value. In practice, the change in the gel's HU is small. For the gel formulation used in this experiment, Jirasek *et al.* measured an approximate linear dose response of $0.32 HU Gy^{-1}$ [51]. This means that at the target isocenter, where the delivered dose was set to $15 Gy$, a change of only $4.8 HU$ can be expected. The low dose sensitivity of the gel means that special care must be taken to optimise CT scanning parameters in order to observe the subtle HU changes in the gel.

Originally, it was intended that the same PQ5000 CT simulator at BCCA used to acquire the simulation CT also be used for imaging the gel response. However, the performance of this scanner proved unsatisfactory for this purpose, due to large inaccuracies in measured HU values. Therefore, the gels were imaged using a different scanner, the Toshiba Aquilion 64 multi-slice CT (Toshiba Medical Systems, Japan) at Canada Diagnostic Centers (Vancouver, BC), a private diagnostic imaging facility.

To extract dose information from the gel and optimise image quality, a CT imaging protocol following the guidelines set in [40] was used. To begin, lead BBs were taped to the gel bottles as CT fiducials. Then, the entire phantom was scanned to establish references for the location of these BBs with respect to the IREDs on the box. This allows the gel bottle positions to be known

with respect to the permanent part of the phantom, and hence the target isocenter locations.

Then, each gel bottle was removed one at a time from the phantom and placed on a styrofoam cradle securely taped to the CT table. The styrofoam cradle ensured that all the bottles were placed in the same position within the CT bore and remained in the same place during CT scanning. Each gel bottle was scanned individually, and orientated so that its axis of symmetry was in approximate alignment with the CT gantry axis of rotation to reduce the presence of imaging artifacts. The CT imaging parameters used to scan the bottles were $0.5mm$ slice thickness, $0.335mm$ pixel size, $135kV$ tube voltage, $350mA$ tube current, and $0.5s$ scan time. To improve image SNR, each bottle was scanned 5 times, and the images were averaged. In addition to the 4 irradiated bottles, a bottle of unirradiated gel was also scanned using the same imaging parameters. The average image of the unirradiated bottle was subtracted from the average image of each irradiated bottle to perform background subtraction and form a difference image of the change in gel HU after irradiation.

The difference image near one of the targets is shown in Figure 5.12. Aside from the bright pixels around the edges of the bottle due to slight misalignment of the irradiated and unirradiated bottles used to calculate the difference image, the bright cluster of pixels corresponding to the location where the gel received the highest dose can clearly be seen.

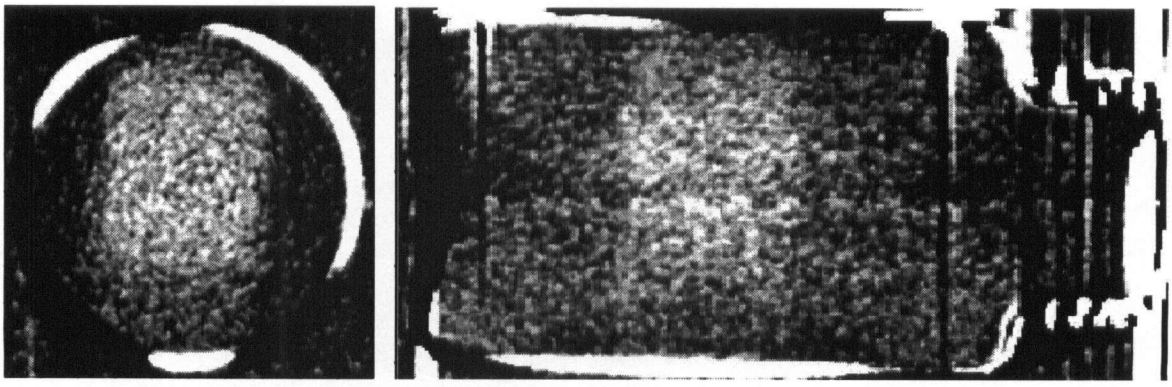

(a) Axial view (b) Sagittal view

Figure 5.12: The difference image near one of the targets showing changes in polymer gel HU after irradiation. The data is windowed from 0 to 10 HU. The white outlines around the edge of the bottle correspond to differences in HU due to slight variations between the shapes of the bottles used to generate the image.

5.7 Results

The target localisation results for the four methods tested in this experiment are presented in the following subsections.

5.7.1 3D Ultrasound Localisation

The automatic pixel-intensity based registration results between the simulation and treatment 3D ultrasound images for localisation of one of the targets is shown in Figure 5.13. The shift required to bring the phantom to the correct treatment position in this case was determined to be $-{}^{L}\underline{x}_{iso} = -[5.3\ 5.4\ 7.6]^{T} mm$ by the proposed system. Since the couch position could only be specified with a finite resolution, shifts could only be implemented to the nearest millimeter in this experiment. Thus, for this target, a correction shift of $-[5\ 5\ 8]^{T}$ was implemented before the phantom was irradiated. The required correction shifts determined by the proposed ultrasound positioning system for all the targets are shown in Table 5.2. These correction shifts should be approximately the opposite of the simulated error shifts in Table 5.1. The remaining difference reflects the disagreement between the laser and 3D ultrasound target localisation results.

Table 5.2: The couch shift required to bring the phantom to the correct treatment position as determined by the proposed 3D ultrasound patient positioning system for all the targets. Note that the correction shift could only be implemented to the nearest millimeter in practice. Shifts are given in LINAC coordinates.

Target	Correction Shift (mm)		
	x	y	z
1	-5.7	0.4	-1.2
2	0.4	1.4	-7.2
3	-2.1	-6.8	-2.2
4	-5.3	-5.4	-7.6

To evaluate the accuracy of positioning the phantom using 3D ultrasound for a particular target isocenter, the 3D dose plan for that target was transferred from the simulation CT coordinates, $\{\varrho_{sim}, \underline{C}_{sim}\}$, to the coordinates of the corresponding difference image, $\{\varrho_{diff}, \underline{C}_{diff}\}$, using

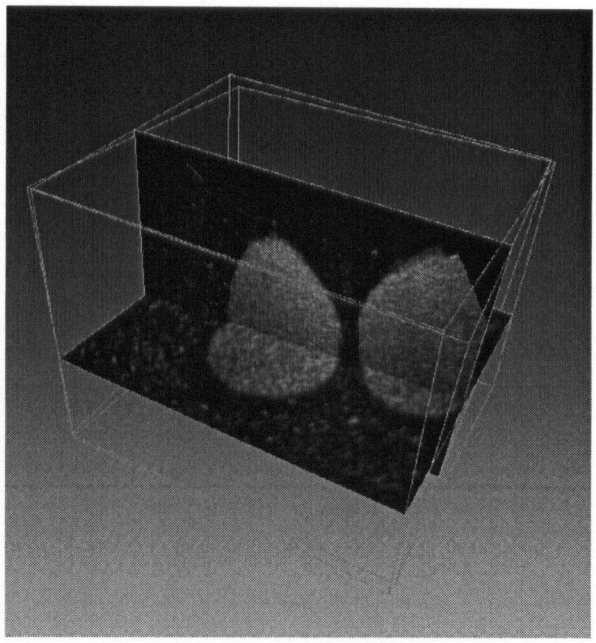

Figure 5.13: The automatic registration results in Amira between simulation and treatment ultrasound images for localising one of the targets. A coronal slice of the simulation ultrasound, and an axial slice of the treatment ultrasound is shown.

$$^{\mathbf{sim}}\mathbf{T}_{\mathbf{diff}} = {}^{\mathbf{sim}}\mathbf{T}_{\mathbf{post}}{}^{\mathbf{post}}\mathbf{T}_{\mathbf{diff}}, \tag{5.6}$$

where $^{\mathbf{sim}}\mathbf{T}_{\mathbf{post}}$ is the transformation from the simulation CT to the post-irradiation CT of the entire phantom, and $^{\mathbf{post}}\mathbf{T}_{\mathbf{diff}}$ is the transformation from the post-irradiation CT to the difference image of the gel bottle containing the target. $^{\mathbf{sim}}\mathbf{T}_{\mathbf{post}}$ was calculated using the IRED locations in both CT images as corresponding points, while $^{\mathbf{post}}\mathbf{T}_{\mathbf{diff}}$ was similarly found using the BB fiducials placed on the bottles. The difference image previously shown in Figure 5.12 with the planned isocenter location and the 80% isodose contour overlayed on top is displayed in Figure 5.15(a).

Next, the actual irradiated isocenter was calculated by registering the 3D dose plan, given by the treatment planning software in a 3D matrix, with the difference image using the same automatic pixel-intensity based registration algorithm used to register 3D ultrasound images, which was described in Section 4.2.2. Thresholding was performed on the difference image before

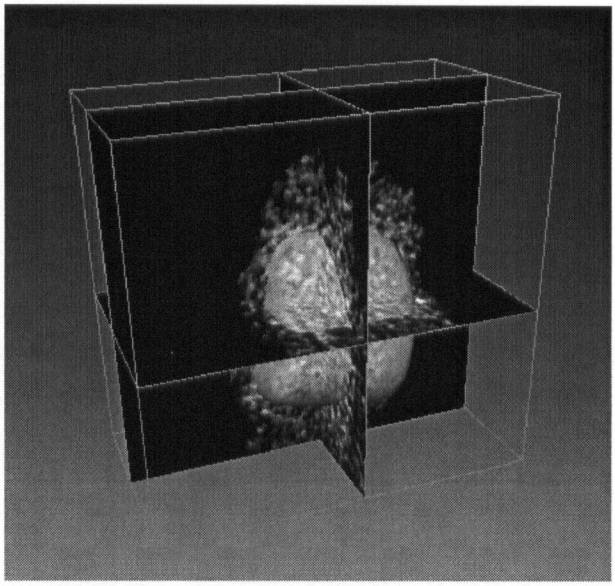

Figure 5.14: Image registration of the difference image for one target and its planned dose in Amira. For ease of visualisation, the 80% isodose surface of the dose plan is shown, along with orthogonal cross-sectional slices of the difference image near the target after preprocessing to remove pixels not corresponding to dose information.

registration to remove pixels which do not correspond to dose information. In addition, the planned isocenter location, as shown in Figure 5.15(a) for one target, was used to initialise the algorithm. As this should be close to the irradiated isocenter location, the possibility of mis-registration is low. The result of the registration for one target is shown in Figure 5.14. The location of the registered isocenter was taken to be the irradiated isocenter location, and this is overlayed on top of the difference image in Figure 5.15(b), along with the registered 80% isodose contour.

Finally, the accuracy of the proposed 3D ultrasound patient positioning system in positioning the phantom for irradiation of the target was determined by calculating the 3D Euclidean distance between the planned and irradiated isocenter locations. The results for all 4 targets are presented in Table 5.3.

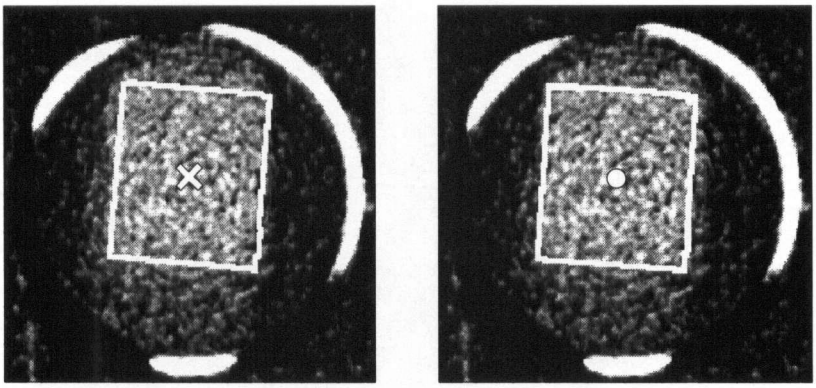

(a) Planned isocenter (b) Irradiated isocenter

Figure 5.15: The planned isocenter location projected onto an axial slice of the difference image for one target is marked with the cross in (a). The planned 80% isodose contour intersection with the slice is also shown in (a) as the white outline. The irradiated isocenter location determined by registering the dose plan and difference image is projected onto the same slice and is marked with the dot in (b). The registered 80% isodose contour is also shown in (b) as the white outline.

Table 5.3: The accuracy of the proposed 3D ultrasound patient positioning system in positioning the phantom for irradiation of the 4 targets. The error vector is the distance between the planned and irradiated isocenter locations in LINAC coordinates.

Target	Error Vector (mm)			Error
	x	y	z	Magnitude (mm)
1	-0.8	1.2	-0.8	1.6
2	1.5	-0.4	-1.2	2.0
3	-1.4	-2.4	-2.2	3.6
4	0.9	-1.9	-2.1	2.9
Mean	–	–	–	2.5

5.7.2 Freehand Ultrasound Localisation

Freehand ultrasound collected before the phantom was shifted into treatment position using 3D ultrasound data was registered off-line to the simulation freehand ultrasound using contours extracted from both scans. This registration was performed using the ICP algorithm, and the results for one target is shown in Figure 5.16. This registration result, and Equation 3.11 were used to find the shift required to bring the phantom into the correct treatment position. The difference

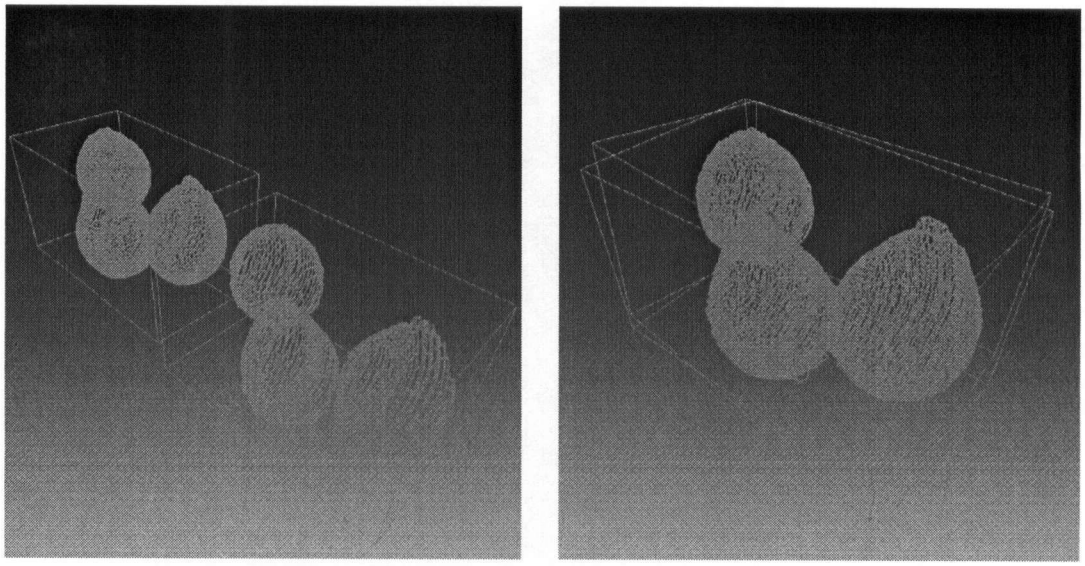

(a) Initial state (b) Final registration result

Figure 5.16: The contours extracted from freehand ultrasound data taken during simulation and during treatment before the phantom was shifted into the treatment position are shown in (a). The contours after registration using the ICP algorithm (b).

in the correction shifts determined by 3D ultrasound and freehand localisation approaches were then applied to the irradiated target location to simulate the result of irradiating the phantom using the freehand correction shift. The simulated freehand localisation results are shown for one target in Figure 5.17(b). The freehand positioning accuracy for all targets are shown in Table 5.4.

Table 5.4: The accuracy of the freehand ultrasound approach in positioning the phantom for irradiation of the 4 targets. The error vector between the planned and simulated irradiated isocenter locations for freehand ultrasound localisation are shown in the LINAC coordinates.

Target	Error Vector (mm)			Error Magnitude (mm)
	x	y	z	
1	-0.8	-1.0	1.3	1.9
2	1.1	2.7	-2.5	3.8
3	-0.6	-0.3	-3.5	3.5
4	-0.7	-1.1	-1.6	2.1
Mean	–	–	–	2.8

5.7.3 OPTOTRAK Localisation

The OPTOTRAK target localisation method detailed in Section 5.2.3 was used to measure the residual positioning error of the phantom after it was shifted to the treatment position using the 3D ultrasound determined correction shifts in Table 5.2. Similar to the analysis performed for the freehand localisation technique, this residual error was applied to the irradiated target location obtained using the 3D ultrasound correction shift to simulate the result of using the OPTOTRAK to position the phantom for irradiation. The simulated OPTOTRAK phantom positioning results are shown for one target in Figure 5.17(c). The OPTOTRAK positioning accuracy for all targets are shown in Table 5.5.

Table 5.5: The accuracy of using the OPTOTRAK to position the phantom for irradiation of the 4 targets. The error vector between the planned and simulated irradiated isocenter locations for OPTOTRAK localisation are shown in the LINAC coordinates.

Target	Error Vector (mm)			Error
	x	y	z	Magnitude (mm)
1	0.6	1.6	0.6	1.9
2	1.1	-1.4	0.0	1.8
3	0.3	-0.2	-1.8	1.8
4	0.7	-1.3	-1.0	1.8
Mean	–	–	–	1.8

5.7.4 Laser Positioning

The accuracy of using the patient alignment lasers and set-up marks to position the phantom initially before implementation of the simulated positioning error was also derived. Similar to the analysis for the freehand and OPTOTRAK positioning methods, the difference between the simulated error and the implemented correction shifts determined by 3D ultrasound (both shown in Table 5.1), was found for all targets. This difference was subtracted from the error vector for 3D ultrasound localisation given in Table 5.3 to find the positioning error that would be expected from using the patient alignment lasers alone. These results are shown in Table 5.6.

Table 5.6: The accuracy of using the laser alignment system to position the phantom for irradiation of the 4 targets. The error vector between the planned and simulated irradiated isocenter locations for laser positioning are shown in the LINAC coordinates.

Target	Error Vector (mm)			Error
	x	y	z	Magnitude (mm)
1	0.0	0.9	0.4	1.0
2	1.0	-1.9	0.9	2.3
3	0.7	-0.7	-0.1	1.0
4	1.2	-1.5	0.6	2.0
Mean	–	–	–	1.6

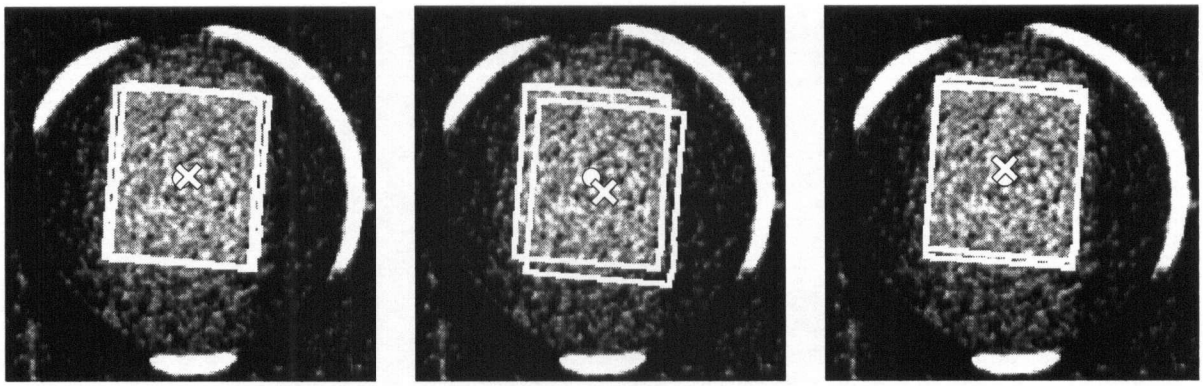

(a) 3D Ultrasound positioning results

(b) Simulated freehand ultrasound positioning results

(c) Simulated OPTOTRAK positioning results

Figure 5.17: Phantom positioning results for Target 2 is shown in one axial slice of the difference image. The planned and irradiated isocenter locations are projected onto the slice and are marked using the cross and dot, respectively. The planned and irradiated 80% isodose contours are also shown using white outlines. The difference between freehand and 3D ultrasound determined correction shifts are applied to the difference image position in the calculation of ${}^{\mathbf{sim}}\mathbf{T}_{\mathbf{diff}}$ using Equation 5.6. The planned dose was transferred to the difference image coordinates using the modified ${}^{\mathbf{sim}}\mathbf{T}_{\mathbf{diff}}$ in order to simulate the positioning results for the freehand localisation approach shown in (b). This was also done to simulate the OPTOTRAK positioning results shown in (c).

5.8 Discussion

The target localisation accuracy of the optical guidance methods tested (*i.e.,* laser and OPTOTRAK) were better overall than ultrasound guidance with the proposed system using either 3D or freehand data. This was not surprising, because the number of error sources for the laser and OPTOTRAK methods are significantly less than ultrasound guidance. Nevertheless, the extra sources of inaccuracy involved with ultrasound target localisation only amounted to $\sim 1mm$ of additional error in practice compared to optical guidance. In addition, the positioning accuracy of the proposed system using 3D ultrasound data was found to be comparable to using freehand data. The sources of error for each target localisation technique tested are discussed in the following subsections. The effects of the phantom used on the experiment outcome is also addressed, as well as a comparison of this study with previous research.

5.8.1 3D Ultrasound Localisation

The most significant sources of error in the proposed 3D ultrasound patient positioning system include simulation CT and ultrasound registration (${}^{\mathbf{U}}\mathbf{T}_{\mathbf{CT}}$), OPTOTRAK to LINAC calibration (${}^{\mathbf{L}}\mathbf{T}_{\mathbf{O'}}$), ultrasound probe calibration (${}^{\mathbf{U}}\mathbf{T}_{\mathbf{P}}$), and 3D ultrasound-to-ultrasound registration (${}^{\mathbf{U'}}\mathbf{T}_{\mathbf{U}}$). In addition, limitations in the accuracy of the couch movements used to implement the correction shifts determined using 3D ultrasound also contributed to the overall phantom positioning error.

${}^{\mathbf{U}}\mathbf{T}_{\mathbf{CT}}$ Error

The method for registering simulation CT and ultrasound scans was previously evaluated in Section 4.1 on a similar phantom, and a RMS registration error of $1.09mm$ can be expected in this case as well.

${}^{\mathbf{L}}\mathbf{T}_{\mathbf{O'}}$ Error

The method used to calibrate the OPTOTRAK to the LINAC is limited by the accuracy of the alignment lasers in marking the exact location of the LINAC isocenter, and the width of the

laser beam, which determines the uncertainty in the crosshair location. The alignment lasers in this experiment has a maximum deviation of $2mm$ from the true isocenter location in each axis direction from quality assurance measures [56], and is $0.5mm$ wide. In the worst case scenario, this gives a maximum error of $\sqrt{3 \times 2.25^2} = 3.9mm$ in measuring the isocenter location using the lasers.

${}^{U}\mathbf{T_P}$ Error

The probe calibration error is incorporated twice in the calculation of the target location by the proposed system: once during simulation, and once during the treatment session (see Figure 3.5 or Equation 3.11). Its effect during simulation is included in determining the overall simulation CT to ultrasound registration accuracy. Since the overall RMS accuracy of this procedure was found to be $1.09mm$, the probe calibration error can be expected to be less than this figure for the treatment session as well. Additionally, the result of the ultrasound-to-ultrasound registration ${}^{U'}\mathbf{T_U}$ for all 4 targets were close to the identity matrix, as shown in Appendix C. Thus, as previously illustrated in Equation 3.13 in Section 3.4, it is possible for some cancellation of systematic probe calibration error to occur.

${}^{U'}\mathbf{T_U}$ Error

The automatic 3D ultrasound-to-ultrasound image registration method used in this experiment was previously applied on a cross-wire phantom in Section 4.2. It was able to achieve a RMS registration accuracy of $0.62mm$ when compared to independent OPTOTRAK measurements. Since the phantom imaged in this experiment contains similar material and well defined features with high contrast, a comparable image registration accuracy can be expected.

Couch Movement Error

Since the couch position could only be specified with a resolution of $1mm$, a maximum positioning error of $\sqrt{3 \times 0.5^2} = 0.87mm$ due to the limited couch resolution is possible.

Overall Error

Summing the estimated magnitude of all the major error sources described previously, the worst-case 3D ultrasound target localisation error is

$$\begin{aligned} \textit{Overall Error} &= {}^{\mathbf{U}}\mathbf{T}_{\mathbf{CT}}\ \textit{Error} + {}^{\mathbf{L}}\mathbf{T}_{\mathbf{O'}}\ \textit{Error} + 2 \times {}^{\mathbf{U}}\mathbf{T}_{\mathbf{P}}\ \textit{Error} \\ &\quad + {}^{\mathbf{U'}}\mathbf{T}_{\mathbf{U}}\ \textit{Error} + \textit{Couch Error} \\ &= 1.09 + 3.9 + 2 \times 1.09 + 0.62 + 0.87 \\ &= 8.66mm \end{aligned} \tag{5.7}$$

These error magnitudes are not additive unless they all happen to be in the same direction. Fortunately, the chances of this occurring are slim in practice. The magnitudes of the ${}^{\mathbf{L}}\mathbf{T}_{\mathbf{O'}}$ and couch errors are also the maximum possible. Indeed, the mean 3D ultrasound target localisation error was found to be $2.5mm$, well below the estimated upper bound in Equation 5.7.

5.8.2 Freehand Ultrasound Localisation

Comparing Tables 5.3 and 5.4, it can be seen that the freehand ultrasound target localisation error is only slightly larger than that obtained using 3D ultrasound. Indeed, the exact same error sources ${}^{\mathbf{U}}\mathbf{T}_{\mathbf{CT}}$, ${}^{\mathbf{L}}\mathbf{T}_{\mathbf{O'}}$, ${}^{\mathbf{U}}\mathbf{T}_{\mathbf{P}}$, and couch movement inaccuracy, affect both methods. However, the freehand localisation method implemented in this study is subject to a number of additional sources of error, due entirely to the ultrasound image acquisition and registration technique used. The most significant of these include volume reconstruction error, OPTOTRAK to ultrasound machine synchronisation, and contour extraction error.

Volume Reconstruction Error

Recall from Section 3.1.1 that the slice positions in freehand ultrasound imaging is unrestricted and unknown, unlike 3D ultrasound volumes acquired using dedicated probes. In order to reconstruct volumetric data from the slices, their positions relative to each other must be calculated using OPTOTRAK measurements of the probe position during image acquisition and knowledge of the

probe calibration parameter. Thus, errors in both of these measurements will lead to inaccuracies in the calculated positions of the slices, and hence the location of features in the reconstructed volume. Moreover, every single slice of the freehand data set is affected by these errors.

The most significant cause of volume reconstruction error in this case will be probe calibration error, as OPTOTRAK measurements are accurate to within $0.15mm$ [47]. As mentioned previously, probe calibration is expected to have an RMS error of no more than $1.09mm$. Although the same probe calibration parameter is used to calculate the position of all the slices, the effect of this error on reconstruction accuracy is dependant on the location and orientation of the probe, which will not be the same for every slice. Furthermore, it is practically impossible for these reconstruction errors to be systematically repeated in multiple acquisitions, as the probe is manually swept in freehand imaging. Therefore, freehand volume reconstruction error cannot be cancelled in the manner previous depicted in Equation 3.13 in Section 3.4. In contrast, when imaging is performed using the dedicated 3D ultrasound probe, any volume reconstruction error is repeatable, and therefore subject to possible cancellation, as the acquisition process is automated.

OPTOTRAK and Ultrasound Data Synchronisation Error

As mentioned in Section 5.2.2, a time delay is required for synchronising OPTOTRAK measurements of the probe position with ultrasound image acquisition times during freehand imaging. An error in this synchronising delay causes an erroneous probe position to be associated with each slice of the freehand data set. To investigate the effect of this error, the localisation accuracy for each target was recalculated using the same freehand ultrasound data, but slightly different values for the synchronisation delay Δt_{sync}, as shown in Figure 5.7.

The results from Table 5.7 suggests that the true delay is in fact closest to the value of $1.5s$ used throughout this experiment, as this still gives the lowest overall target localisation error. Thus, the contribution of data sychnronisation inaccuracy on the overall freehand ultrasound localisation error is expected to be small.

Table 5.7: Freehand ultrasound target localisation accuracy using different delays to synchronise OPTOTRAK and ultrasound data. For convenience, the results shown previously in Table 5.4, obtained using the delay value of $1.5s$ determined in Section 5.2.2, are repeated here.

Target	Error Magnitude (mm)			
	$\Delta t_{sync} = 1.4s$	$\Delta t_{sync} = 1.5s$	$\Delta t_{sync} = 1.6s$	$\Delta t_{sync} = 1.7s$
1	4.7	1.9	3.1	1.1
2	5.8	3.8	4.5	2.5
3	5.5	3.5	1.6	6.7
4	4.2	2.1	3.0	3.9
Mean	5.1	2.8	3.1	3.6

Contour Extraction Error

An extra step which is performed in registering freehand ultrasound images in this experiment is the extraction of contours from the image slices (outlining the boundary of relevant features). Registration of freehand images are performed using these contours, rather than the entire image data, like the proposed 3D ultrasound-based approach. Therefore, inaccuracies in the contour extraction process will contribute to errors in the freehand registration result ${}^{U'}\mathbf{T}_{U}$.

Contouring of the phantom ultrasound images in this experiment was able to be achieved automatically using thresholding, since the balloons provided clear features with high contrast. Nevertheless, discrepancies in contours extracted from different freehand images will occur due to image noise, non-uniform image spatial resolution, and differences in slice location and orientation. In ultrasound images of real anatomy, automatic contour extraction is not likely to be possible due to poor contrast and image noise.

The magnitude of the error involved in the automatic contour extraction process used in this experiment is hard to quantify. However, the residual distance between closest matching contour points after registration of the simulation and treatment freehand ultrasound images is a reflection of the difference in the contours extracted from both images. The RMS value of this residual error for all contour points is shown for the registrations performed in Table 5.8. Note that this measure also includes error in the reconstructed contour shapes due to volume reconstruction and

Table 5.8: The RMS registration error between closest matching contour points after registering the simulation and treatment freehand ultrasound using the ICP algorithm to localise the 4 targets.

Target	RMS Error (mm)
Target 1	1.31
Target 2	1.26
Target 3	1.61
Target 4	0.98
Mean	1.29

data synchronisation error.

Overall Error

Similar to the 3D ultrasound target localisation scheme, the worst-case error for freehand target localisation is given by Equation 5.7 as well. The expected magnitude of all the individual error sources in this equation are identical for both approaches, except for the ${}^{U'}\mathbf{T}_U$ error. As stated before, in the freehand method, ${}^{U'}\mathbf{T}_U$ is subject to additional errors due to inaccuracies in volume reconstruction, data synchronisation, and contour extraction. However, comparing the overall target localisation results for the two approaches, it can be seen that only a small amount of extra error is induced by the freehand method.

As was shown previously, the data synchronisation error may not be significant in this experiment. However, considerable variations in the contour locations still exist due to reconstruction and contour extraction error, as shown in Table 5.8. It is important to note that even with the presence of such errors, it is still possible for an accurate registration result for ${}^{U'}\mathbf{T}_U$ to be obtained, as long as the errors are sufficiently small and uniformly distributed in all directions over all the contour points. Thus, freehand contour-based registration was able to achieve a similar accuracy as 3D pixel-intensity based registration in this experiment.

5.8.3 OPTOTRAK Localisation

The major sources of error in using the OPTOTRAK to position the phantom includes the OPTOTRAK to LINAC calibration procedure (${}^{\mathbf{L}}\mathbf{T}_{\mathbf{O}'}$), and transformation from the phantom to CT coordinates (${}^{\mathbf{Pat}}\mathbf{T}_{\mathbf{CT}}$). The error in ${}^{\mathbf{L}}\mathbf{T}_{\mathbf{O}'}$ is the same as for the 3D ultrasound-based localisation method, which was previously described in this Section. The transformation ${}^{\mathbf{Pat}}\mathbf{T}_{\mathbf{CT}}$ is a component of the simulation CT to ultrasound registration error (${}^{\mathbf{U}}\mathbf{T}_{\mathbf{CT}}$) for 3D ultrasound-based localisation, which was previously evaluated to have a RMS target registration error (TRE) of $1.09mm$. Thus, the worst possible OPTOTRAK target localisation error is given by

$$\begin{aligned} \textit{Overall Error} &= {}^{\mathbf{L}}\mathbf{T}_{\mathbf{O}'}\ \textit{Error} + {}^{\mathbf{Pat}}\mathbf{T}_{\mathbf{CT}}\ \textit{Error} \\ &= 3.9 + 1.09 \\ &= 4.99mm \end{aligned} \tag{5.8}$$

Again, the actual errors shown in Table 5.5 are considerably lower than the worst-case scenario, as the errors in Equation 5.8 are the maximum possible, and are not additive unless they are in the same direction. Note that couch movement error is not included in the target localisation accuracy results for the OPTOTRAK, as for the other methods. This is because the OPTOTRAK was used to measure the residual positioning error after the phantom is shifted to its final position before being irradiated.

5.8.4 Laser Positioning

The accuracy of the conventional laser positioning method depends on the accuracy of the alignment lasers, drawing of the set-up marks during the simulation procedure, manual alignment of the set-up marks with the lasers during treatment, and couch movement.

As mentioned previously in this discussion, the alignment lasers are accurate to within $2mm$ in each axis in marking the true LINAC isocenter location. In addition, they are $0.5mm$ wide. Therefore, in the worse-case scenario, a maximum error of $\sqrt{3 \times 2.25^2} = 3.9mm$ can occur with the laser indicators.

Errors in manual labelling of the set-up marks and aligning these to the laser positions largely depends on the diligence of the experimenter, and every effort was made to minimise these errors. During simulation, laser projections on the phantom were carefully marked using a fine-point marker. In the treatment room, these marks were aligned with the laser system in the room as accurately as possible. However, residual errors due to differences in the couch sag and laser positions in the simulator and treatment rooms are still possible.

Finally, couch shifts are required to implement the displacement from the treatment plan origin, as labelled by the set-up marks, to the actual target location. As mentioned earlier, the motor-driven couch is only able to move in $1mm$ increments. Thus, a maximum error of $0.87mm$ in the phantom position due to finite couch precision is possible.

Thus, assuming the set-up marks on the phantom are accurately drawn and aligned with the positioning lasers inside the treatment room during set-up, the maximum possible positioning error is given by

$$\begin{aligned} Overall\ Error &= Laser\ Error + Couch\ Error \\ &= 3.9 + 0.87 \\ &= 4.77mm \end{aligned} \tag{5.9}$$

From Table 5.6, the mean target localisation error using the lasers was $1.6mm$, considerably less than the worst-case scenario depicted in Equation 5.9. In practice, the laser and couch movement errors are likely to be smaller than the maximum possible values of $3.9mm$ and $0.87mm$, respectively. The low laser target localisation error obtained in this experiment also suggest that inaccuracies due to manual labelling of the set-up marks and aligning them to the lasers were not significant.

5.8.5 Phantom Effects on Experimental Results

In this experiment, the effect of any ultrasound-to-ultrasound image registration error on the accuracy of the target localisation results may be amplified by the lever-arm effect. Recall that the target locations are not within the ultrasound image field of view, since the polymer gel bottles

are adjacent to the box used for ultrasound scanning. The mean distance from the center of the simulation ultrasound volume to the four targets within the gel bottles is $160mm$. Even with a registration error of 1° between the simulation and treatment ultrasound volumes, the misalignment at this distance away would be $2.8mm$. In conventional use of the proposed 3D ultrasound patient positioning system, the target isocenter would be directly imaged using ultrasound. However, this was not possible with the phantom in this experiment. This means the target localisation accuracy results obtained for the proposed system are the worst-case scenario in terms of geometry. Note that this effect also applies to the freehand ultrasound localisation results. However, since the target localisation error was relatively low for both the 3D and freehand ultrasound methods and well within the expected upper bounds, it seems that this effect did not have a significant impact on the overall results.

Nevertheless, it is important to recognise that the phantom used in this experiment represents an idealised patient, and that the positioning accuracy achieved by the various methods tested still represent lower bounds. The automatic pixel-intensity based 3D ultrasound-to-ultrasound registration results obtained correspond to the best-case scenario for image registration, as there were many clear features present in the ultrasound image. In addition, artifacts such as refraction and speed of sound error were not present as would likely be for a real patient[1]. The presence of clear features with high contrast also enables the extraction of contours from freehand ultrasound images of the phantom to be performed automatically by thresholding. In ultrasound images of real anatomy, contours are usually drawn manually, which increases the likelihood of further errors.

The phantom is also incompressible, unlike real tissue. Thus, non-rigid organ motion was not present to impair the performance of the image registration algorithm, which assumes a rigid transformation between images. Moreover, a potentially significant source of error in practice for freehand ultrasound is caused by tissue deformation from probe pressure as it is manually swept over the area of interest to be imaged. If this deformation is non-uniform in different slices of the freehand data acquired, then the locations of features in the reconstructed volume will appear to

[1]Note that if these imaging errors were reproducible, their effect can in fact be cancelled by the proposed 3D ultrasound system, as shown in Equation 3.13 in Section 3.4.

be out of alignment. Since the phantom imaged in this experiment is incompressible, this weakness of the freehand target localisation technique is not exposed in this study. In comparison, the probe remains stationary over the patient during 3D image acquisition with a dedicated 3D ultrasound probe. Thus, if the applied probe pressure is reproducible, then localisation error due tissue deformation can potentially be cancelled according to Equation 3.13 in Section 3.4.

Internal organ motion and skin mark migration in real patients will also introduce errors into optical guidance methods, including using alignment lasers and optical cameras to track the patient. This is where image guidance techniques, such as the proposed ultrasound patient positioning system, offer a significant clinical advantage. Ultrasound imaging can enable the internal anatomy surrounding the target isocenter to be directly visualised, whereas optical guidance techniques can only localise external fiducials on the surface of the patient at some distance from the treatment target. Since a rigid phantom is positioned in this experiment, the full advantage of ultrasound over laser and OPTOTRAK localisation methods is not fully exploited. Hence, even though more accurate target localisation results were obtained using optical guidance than ultrasound-based methods in this experiment, the presence of internal organ motion in real patients means that the former will not necessarily be more accurate in clinical practice.

5.8.6 Comparison to Previous Studies

Studies of target localisation accuracy and quality assurance of ultrasound patient positioning systems for radiotherapy have not been widely reported in the literature, even though there has been a proliferation of these systems in clinical usage. Tomé *et al.* described the procedures used for acceptance testing of the SonArray system in [101]. Similar to the experiment performed here, the process of radiotherapy was simulated on a phantom attached with a fiducial array of passive infra-red markers for the Polaris (NDI) optical position sensor system. This phantom was positioned inside the LINAC under optical-guidance using the Polaris in the same way as the OPTOTRAK localisation method tested in this study. An artificial set-up error was induced by moving the couch and was measured using the Polaris. Then, this set-up error was determined using the SonArray ultrasound target localisation system. It was found that on average, the

magnitude of the shift determined using ultrasound localisation agreed to within $1mm$ of the shifts measured using optical-guidance along each axis.

Comparing the target localisation accuracy results between the proposed system in Table 5.3, and using the OPTOTRAK in Table 5.5, it can be seen that the results of the current study are only slightly larger than that of Tomé *et al.*. However, unlike Tomé *et al.*, the experiment described herein does not use optical-guidance as the 'ground truth' for target localisation accuracy. Instead, the phantom is positioned like a real patient in the treatment room with respect to an absolute frame of reference (that of the LINAC isocenter). Furthermore, the phantom is irradiated, and changes in its material properties are compared with the treatment plan to close the loop on the entire treatment process in order to verify the accuracy of the proposed ultrasound positioning system, as well as optical-guidance using the OPTOTRAK.

Thus, the entire process of radiotherapy treatment, including simulation imaging, treatment planning, patient positioning at the time of treatment, and irradiation, is simulated in this experiment. Errors such as couch movement inaccuracy, inaccurate calibration of the optical camera system to the LINAC, and accuracy of the LINAC itself in delivering the prescribed dose are included in the target localisation error, giving a more realistic measure of the overall expected treatment accuracy. No previous study on IGRT systems has attempted to show this type of start-to-end validation. The general experimental methodologies concerning the use of polymer gel dosimetry described in this Chapter can be adopted for quality assurance testing of other IGRT systems as well.

Chapter 6

Conclusions and Future Work

This chapter begins with a review of the proposed 3D ultrasound-based patient positioning system which highlights its benefits, as well as the main contributions of this thesis. Next, conclusions derived from the experimental results presented in Chapters 4 and 5 are given. Finally, suggestions for future research directions based on the work presented in this thesis is discussed.

6.1 System Summary

In this thesis, a novel 3D ultrasound-based patient positioning system for improving the accuracy of radiation delivery in radiotherapy treatment has been described. This system uses a dedicated 3D probe to acquire a 3D ultrasound image of the patient anatomy during the simulation session immediately after CT scanning. This simulation ultrasound image is then registered to the simulation CT to enable transfer of planned dose information, defined in the simulation CT coordinates, to the simulation ultrasound. Before the commencement of daily treatment, the patient's position in the LINAC is verified by acquiring a 3D ultrasound image of the treatment anatomy. This treatment ultrasound is automatically registered to the simulation ultrasound to enable localisation of the planned isocenter in the LINAC coordinates. This allows any discrepancies between the LINAC isocenter and planned isocenter location to be detected and corrected before the patient is irradiated.

Compared to other ultrasound-based patient positioning systems in use, the proposed system has a number of significant advantages:

1. 3D ultrasound images are acquired using dedicated 3D probes. This makes the 3D image acquisition and reconstruction process easier, faster, and more repeatable than the freehand ultrasound imaging techniques used by other systems.

2. An ultrasound image is taken during the simulation session in the proposed treatment protocol, like the Restitu system. This additional ultrasound scan enables the patient anatomy at the time of treatment and simulation to be compared using the same imaging modality (ultrasound). Unlike the Restitu, however, the proposed system explicitly registers the simulation CT and ultrasound images, and thus has some capability (rigid-body) of coping with patient motion between the two scans.

3. The effect of systematic 3D ultrasound imaging errors on the proposed system accuracy may be reduced if ultrasound images acquired in a repeatable manner with similar views of the anatomy are compared to localise the target.

4. The proposed system uses automatic pixel-intensity based image registration algorithms to register simulation and treatment ultrasound scans. This removes the need for manual contouring or alignment of images, and means that positioning accuracy of the proposed system is not dependant on operator skill, unlike current existing approaches.

The major contributions of this thesis include:

1. Describing the patient positioning problem in radiotherapy treatment using coordinate transformations so that different target localisation methods can be compared in a common mathematical framework. This allows sources of error in different systems to be readily identified, and gives insight on how their effect on the overall system accuracy may be reduced.

2. Proposing a method for registering CT and ultrasound images taken during simulation without the use of image content directly. This obviates the need to solve the difficult problem of intermodality image-based CT and ultrasound registration. The accuracy of this method was verified using CT and ultrasound images of a phantom. Furthermore, it was shown that OPTOTRAK IREDs can be directly used as fiducial markers in CT images, a capability not previously exploited for image registration applications.

3. Demonstrating the feasibility of using an automatic pixel-intensity based image registration algorithm to register 3D ultrasound images of a volunteer's neck acquired with the Voluson 730 ultrasound system.

4. Using a novel validation method incorporating polymer gel dosimetry, which allows the entire process of radiotherapy to be simulated on a phantom, to measure the overall accuracy of the proposed patient positioning system. In addition, the accuracy of positioning the phantom using OPTOTRAK optical guidance, using a freehand ultrasound localisation approach, and using the conventional method of alignment lasers and set-up markings, were able to be determined by comparing positioning results with the proposed system. No previous study on IGRT systems has attempted to simulate the entire radiotherapy treatment process as comprehensively and show a comparable level of validation as the work presented herein.

6.2 Conclusions

In this thesis, it has been shown that a 3D ultrasound-based patient positioning system for IGRT can be implemented using the Voluson 730 ultrasound and the OPTOTRAK position sensor. The method proposed for registering CT and 3D ultrasound images taken during the simulation session was verified to have an RMS TRE accuracy of $1.09mm$ on a phantom. For a real patient, this registration accuracy may be impaired by non-rigid patient motion between CT and ultrasound imaging. The degree of non-rigid movement will vary between patients and treatment sites, and could be further investigated in future work.

Automatic pixel-intensity based registration of 3D ultrasound images was found to be feasible for images acquired using the Voluson 730 from the neck of a volunteer. In the absence of ground truth, the registration results were verified by manual inspection. In 44 out of 45 image pairs registered, no obvious misalignment was observed. The algorithm used to perform registration of the neck images was not specifically customised for this application. Therefore, these findings suggest that with further site-specific processing, pixel-intensity based image registration methods have the potential to achieve accurate automatic alignment of 3D ultrasound images acquired with the Voluson 730.

The accuracy of the proposed system in positioning a rigid phantom for irradiation of 4 target locations was validated using polymer gel dosimetry. The positioning error for the 4 targets were all under $4mm$ with an average of $2.5mm$. Despite introducing a number of extra sources of error

into the target localisation process, the overall accuracy of the proposed 3D ultrasound patient positioning system was only $\sim 1mm$ worse than the optical phantom positioning methods tested, including the conventional radiotherapy technique of using alignment lasers and set-up marks. In clinical practice, the magnitude of interfractional organ motion at most treatment sites is likely to exceed the additional error ($\sim 1mm$) introduced by 3D ultrasound target localisation [57]. Since ultrasound guidance is capable of compensating for internal organ motion, using the proposed 3D ultrasound-based system to position patients for treatment should still present a significant improvement over the current established methods in radiotherapy.

In addition, using 3D ultrasound data and pixel-intensity based image registration to position the phantom gave comparable results to using freehand data and contour-based registration. However, the real advantages of using 3D ultrasound for target localisation was not fully exploited in this experiment. In a real patient, tissue deformation under applied probe pressure and the need to contour the outlines of anatomical features present additional challenges for a freehand ultrasound-based target localisation system.

6.3 Future Work

Many avenues of research following the work presented herein are possible. These include making improvements to methods presented in this thesis so that the proposed system can be implemented clinically, adapting the experimental methodology presented in Chapter 5 to assess the accuracy of other IRGT systems, and validating the accuracy of the proposed system on real patients.

6.3.1 Clinical Implementation of the Proposed System

A number of issues must be addressed before the 3D ultrasound-based patient positioning system proposed in this thesis can be implemented clinically:

1. As mentioned in Section 4.1.5, the small size of the IRED markers can lead to inaccuracies in determining their exact location in the simulation CT scan. Therefore, attaching the IRED bodies to a larger base before placing them on the patient to aid the identification of

their orientation, and hence exact location in CT, can be explored. Alternatively, passive spherical markers used by the Polaris tracking system could be evaluated as fiducials in CT.

2. The maximum number of IREDs that can be placed on the patient without excessively extending the time needed for the simulation procedure should be determined. There may also be an optimal arrangement for the markers which will minimise the registration error at the target [65].

3. Once a suitable treatment site to be localised using the proposed system is identified, a pixel-intensity based image registration algorithm for automatic registration of 3D ultrasound images of anatomy at that site should be developed. The performance characteristics of this algorithm (e.g., speed, capture range) on typical images should be evaluated.

4. The effects of tissue deformation caused by ultrasound probe pressure during imaging on the accuracy of 3D ultrasound patient positioning has not been investigated in this thesis. As mentioned in Section 3.4, positioning errors due to tissue deformation is expected to be less for 3D ultrasound-based than existing freehand ultrasound-based systems. If similar downward probe pressure is used to acquire simulation and treatment ultrasound scans using dedicated 3D probes, then partial cancellation of the effect of tissue deformation can potentially be achieved. In practice, tissue deformation can be significant in some treatment sites [4]. Thus, studies could be performed to evaluate the magnitude and direction of typical target displacement due to probe pressure during imaging for a particular treatment site.

6.3.2 Phantom Validation

The experimental methodology presented in Chapter 5 to validate the proposed 3D ultrasound patient positioning system can easily be adapted to assess the accuracy of other IGRT systems. As it was shown in Chapter 5, the same phantom was used to determine the positioning error for the freehand ultrasound-based localisation approach, optical-guidance, and laser positioning. Indeed, the phantom could also have been used to assess the accuracy of any other ultrasound patient positioning system, including the BAT, SonArray, and Restitu.

Comparative studies on the accuracy of different ultrasound patient positioning systems have not been widely reported in the literature [20]. Therefore, such an investigation would be invaluable for researchers, cancer clinics, and even the manufacturers of such systems. The difficulties in performing such a test include the lack of control in the subjects (i.e., patients being positioned), access to the different systems, and variations in validation techniques. Using a phantom such as the one in Chapter 5, however, these problems can be overcome. Firstly, since the phantom is rigid, its 'anatomy' is temporally stable. Secondly, the phantom is portable, so can be transported to different centers operating different systems. Lastly, the same validation technique utilising polymer gels to store the delivered dose can be used to evaluate different systems. The same treatment plan can also be reused for each system to ensure consistency in the intended target locations.

Modifications to the phantom could be made to accommodate validation of IGRT systems based on other imaging modalities besides ultrasound. For example, the ultrasound gel and balloons inside the box can be replaced with material with suitable CT contrast to evaluate CT-based IGRT systems.

Development of less toxic polymer gel formulations with longer lifespan is another possible area of related research. Currently, polymer gels cannot be manufactured in large quantities, and must be handled with care. In addition, they must be manufactured on the same day it is to be irradiated. If these two restrictions were removed, then the polymer gel could be housed directly inside the same container as the contrast materials to be imaged on the phantom. In fact, the balloons inside the phantom used in Chapter 5 could directly be filled with the polymer gel. Then, the target locations would lie within the ultrasound image field of view during testing, as they would be in conventional use of ultrasound for patient positioning.

6.3.3 Patient Validation

While phantoms can be used to gauge the lower-bound positioning accuracy of the proposed system, validation of the system accuracy on real patients provides the most realistic measure of the expected treatment outcome. Effects such as poor contrast, noise, and the presence of

artifacts in ultrasound images, tissue and organ deformation, can all have detrimental effects on the patient positioning accuracy.

Unfortunately, all these effects cannot be simulated using a phantom. Conversely, it is not possible to measure the dose delivered to a real patient using polymer gel dosimetry. This means that the performance of the proposed system on real patients can only be assessed by comparison with another IGRT system which can be trusted to provide reliable results.

Previously, the BAT and Restitu ultrasound patient positioning systems have been tested on patients and validated using repeat CT scanning [20, 61], and portal imaging [58, 108]. Other IGRT systems that could be used to validate the proposed system include cone-beam CT and even current existing ultrasound-based patient positioning systems. With the increased usage of IGRT systems in clinical practice, the opportunity to validate the proposed 3D ultrasound-based patient positioning system on real patients is a likely prospect in the future.

6.3.4 Real-time 3D Ultrasound Guidance During Treatment Delivery

Finally, a natural extension of the proposed 3D ultrasound patient positioning system is to utilise the 4D imaging capabilities of the Voluson 730 to monitor the position of the tumour in real-time during the treatment delivery process. This would help to remove uncertainties in the target location caused by possible intrafractional motion and would facilitate even more accurate delivery of radiation to highly mobile tumour sites. Incidentally, this approach would also eliminate the detrimental effect of tissue deformation due to probe pressure on ultrasound target localisation accuracy, as the ultrasound probe would remain in place during entire treatment procedure.

The recent work of Hsu *et al.* [44] suggests that this approach may be highly feasible. In this study, a 2D ultrasound probe positioned just outside the radiation field was used to track in-plane rigid motion of a phantom while the LINAC operated. The motion tracking algorithm used was based on optimising the image correlation coefficient, similar to the algorithm used in this thesis for registering 3D ultrasound images. It was found that the LINAC beam did not significantly degrade the accuracy of the tracking algorithm, and did not cause permanent or temporary adverse effects on the ultrasound transducer and its ability to acquire images. Furthermore, minimal changes

in dose distributions were caused by scatter from the probe. With advancements in both 3D ultrasound imaging technology and computing power, real-time tracking of organ motion in 3D ultrasound for radiotherapy applications remains an exciting possibility.

Bibliography

[1] ICRU Report #50. Prescribing, recording and reporting photon beam therapy. Technical report, International Commission on Radiation Units and Measurements, 1993.

[2] J. R. Adler Jr, M. J. Murphy, S. D. Chang, and S. L. Hancock. Image-guided robotic radiosurgery. *Neurosurgery*, 44(6):1299–1306, 1999.

[3] H. Alasti, M. P. Petric, C. N. Catton, and P. R. Warde. Portal imaging for evaluation of daily on-line setup errors and off-line organ motion during conformal irradiation of carcinoma of the prostate. *Int. J. Radiat. Oncol. Biol. Phys.*, 49(3):869–884, 2001.

[4] X. Artignan, M. Smitsmans, J. Lebesque, D. Jaffray, M. van Her, and H. Bartelink. Online ultrasound image guidance for radiotherapy of prostate cancer: impact of image acquisition on prostate displacement. *Int. J. Radiat. Oncol. Biol. Phys.*, 59(2):595–601, 2004.

[5] A. W. Beavis. Is tomotherapy the future of IMRT? *Br. J. Radiol.*, 77(916):285–295, 2004.

[6] G. C. Bentel. *Patient Positioning and Immobilization in Radiation Oncology.* McGraw-Hill, first edition, 1999.

[7] P. J. Besl and N. D. McKay. A method for registration of 3-D shapes. *IEEE Trans. Pattern Anal. Machine Intell.*, 14(2):239–256, 1992.

[8] P. J. Biggs, M. Goitein, and M. D. Russell. A diagnostic X ray field verification device for a 10 MV linear accelerator. *Int. J. Radiat. Oncol. Biol. Phys.*, 11(3):635–643, 1985.

[9] N. Bilaniuk and G. S. K. Wong. Speed of sound in pure water as a function of temperature. *J. Acoust. Soc. Am.*, 93(3):1609–1612, 1993.

[10] L. N. Bohs, B. J. Geiman, M. E. Anderson, S. C. Gebhart, and G. E. Trahey. Speckle tracking for multi-dimensional flow estimation. *Ultrasonics.*, 38:369–375, 2000.

[11] L. G. Bouchet, S. L. Meeks, G. Goodchild, F. J. Bova, J. M. Buatti, and W. A. Friedman. Calibration of three-dimensional ultrasound images for image-guided radiation therapy. *Phys. Med. Biol.*, 46(2):559–577, 2001.

[12] A. L. Boyer, L. Antonuk, A. Fenster, M. Van Herk, H. Meertens, P. Munro, L. E. Reinstein, and J. Wong. A review of electronic portal imaging devices (EPIDs). *Med. Phys.*, 19(1):1–16, 1992.

[13] S. Brindha, A. J. Venning, B. Hill, and C. Baldock. Experimental study of attenuation properties of normoxic polymer gel dosimeters. *Phys. Med. Biol.*, 49(20):N353–361, 2004.

[14] M. M. Burlew, E. L. Madsen, J. A. Zagzebski, R. A. Banjavic, and S. W. Sum. A new ultrasound tissue-equivalent material. *Radiology*, 134:517–520, 1980.

[15] N. L. Bush and C. R. Hill. Gelatin-alginate complex gel: a new acoustically tissue-equivalent material. *Ultrasound Med. Biol.*, 9(5):479–484, 1983.

[16] A. Chandra, L. Dong, E. Huang, D. A. Kuban, L. O'Neill, I. Rosen, and A. Pollack. Experience of ultrasound-based daily prostate localization. *Int. J. Radiat. Oncol. Biol. Phys.*, 56(2):436–447, 2003.

[17] C. W. Cheng, J. Wong, L. Grimm, M. Chow, M. Uematsu, and A. Fung. Commissioning and clinical implementation of a sliding gantry CT scanner installed in an existing treatment room and early clinical experience for precise tumor localization. *Am. J. Clin. Oncol.*, 26(3):e28–e36, 2003.

[18] D. A. Christensen. *Ultrasonic Bioinstrumentation.* Wiley, first edition, 1988.

[19] L. Court, I. Rosen, R. Mohan, and L. Dong. Evaluation of mechanical precision and alignment uncertainties for an integrated CT/LINAC system. *Med. Phys.*, 30(6):1198–1210, 2003.

[20] F. Cury, G. Shenouda, L. Souhami, M. Duclos, S. Faria, M. David, R. Corns, and T. Falco. Comparison of BAT system and a new 3D trans-abdominal ultrasound-based image-guided system for prostate daily localization during external beam radiotherapy. *Int. J. Radiat. Oncol. Biol. Phys.*, 60(1):S329, 2004.

[21] H. C. de Boer, J. R. van Sornsen de Koste, C. L. Creutzberg, A. G. Visser, P. C. Levendag, and B. J. Heijmen. Electronic portal image assisted reduction of systematic set-up errors in head and neck irradiation. *Radiother. Oncol.*, 61(3):299–308, 2001.

[22] Y. De Deene, C. Hurley, A. Venning, K. Vergote, M. Mather, B. J. Healy, and C. Baldock. A basic study of some normoxic polymer gel dosimeters. *Phys. Med. Biol.*, 47(19):3441–3463, 2002.

[23] L. Dong, R. de Crevoisier, M. Bonnen, A. Lee, R. Cheung, H. Wang, J. O'Daniel, R. Mohan, J. Cox, and D. Kuban. Evaluation of an ultrasound-based prostate target localization technique with an in-room CT-on-rails. *Int. J. Radiat. Oncol. Biol. Phys.*, 60(1):S332–S333, 2004.

[24] C. Enke, K. Ayyangar, C. B. Saw, W. Zhen, Thompson R. B., and N. V. Raman. Inter-observer variation in prostate localization utilizing BAT. *Int. J. Radiat. Oncol. Biol. Phys.*, 54(2):S269, 2002.

[25] L. A. Feldkamp, L. C. Davis, and J. W. Kress. Practical cone-beam algorithm. *J. Opt. Soc. Am. A*, 1(6):612–619, 1984.

[26] A. Fenster, D. B. Downey, and H. N. Cardinal. Three-dimensional ultrasound imaging. *Phys. Med. Biol.*, 46(5):R67–R99, 2001.

[27] M. Ferrant, S. K. Warfield, C. R. G. Guttmann, R. V. Mulkern, F. A. Jolesz, and R. Kikinis. 3D image matching using a finite element based elastic deformation model. In *Lecture Notes in Computer Sciences*, volume 1679, pages 202–209. Springer-Verlag, 1999.

[28] J. M. Fitzpatrick and M. Sonka, editors. *Handbook of Medical Imaging*, volume 2. SPIE, 2000.

[29] G. Flaccavento. Patient and probe tracking during freehand ultrasound. Master's thesis, The University of British Columbia, 2004.

[30] D. Fu, G. Kuduvalli, V. Mitrovic, W. Main, and L. Thomson. Automated skull tracking for the Cyberknife® image-guided radiosurgery system. In *Medical Imaging 2005 - Visualization, Image-Guided Procedures, and Display*, volume 5744 of *Proceedings of SPIE*, pages 366–377, 2005.

[31] M. Fuss, S. X. Cavanaugh, C. Fuss, D. A. Cheek, and B. J. Salter. Daily stereotactic ultrasound prostate targeting: inter-user variability. *Technol. Cancer. Res. Treat.*, 2(2):161–170, 2003.

[32] M. Fuss, B. J. Salter, S. X. Cavanaugh, C. Fuss, A. Sadeghi, C. D. Fuller, A. Ameduri, J. M. Hevezi, T. S. Herman, and C. R. Thomas Jr. Daily ultrasound-based image-guided targeting for radiotherapy of upper abdominal malignancies. *Int. J. Radiat. Oncol. Biol. Phys.*, 59(4):1245–1256, 2004.

[33] P. C. Gerszten and W. C. Welch. Cyberknife radiosurgery for the spine. *Tech. neurosurg.*, 9(3):232–241, 2003.

[34] R. C. Gonzalez and R. E. Woods. *Digital Image Processing.* Prentice-Hall, second edition, 2002.

[35] B. A. Groh, J. H. Siewerdsen, D. G. Drake, J. W. Wong, and D. A. Jaffray. A performance comparison of flat-panel imager-based MV and kV cone-beam CT. *Med. Phys.*, 29(6):967–975, 2002.

[36] A. R. Groves and R. N. Rohling. Two-dimensional spatial compounding with warping. *Ultrasound Med. Biol.*, 30(7):929–942, 2004.

[37] M. G. Herman. Clinical use of electronic portal imaging. *Semin. Radiat. Oncol.*, 15(3):157–167, 2005.

[38] M. G. Herman, T. M. Pisansky, J. J. Kruse, J. I. Prisciandaro, B. J. Davis, and B. F. King. Technical aspects of daily online positioning of the prostate for three-dimensional conformal radiotherapy using an electronic portal imaging device. *Int. J. Radiat. Oncol. Biol. Phys.*, 57(4):1131–1140, 2003.

[39] M. Hilts, C. Audet, C. Duzenli, and A. Jirasek. Polymer gel dosimetry using x-ray computed tomography: a feasibility study. *Phys. Med. Biol.*, 45(9):2559–2571, 2000.

[40] M. Hilts, A. Jirasek, and C. Duzenli. Technical considerations for implementation of x-ray CT polymer gel dosimetry. *Phys. Med. Biol.*, 50:1727–1745, 2005.

[41] S. C. Hoffelt, L. M. Marshall, M. Garzotto, A. Hung, J. Holland, and T. M. Beer. A comparison of CT scan to transrectal ultrasound-measured prostate volume in untreated prostate cancer. *Int. J. Radiat. Oncol. Biol. Phys.*, 57(1):29–32, 2003.

[42] B. K. P. Horn. Closed-form solution of absolute orientation using unit quaternions. *J. Opt. Soc. Am. Ser. A.*, 4(4):629–642, 1987.

[43] J. Hsieh. *Computed tomography: principles, design, artifacts, and recent advances.* SPIE, first edition, 2003.

[44] A. Hsu, N. R. Miller, P. M. Evans, J. C. Bamber, and S. Webb. Feasibility of using ultrasound for real-time tracking during radiotherapy. *Med. Phys.*, 32(6):1500–1512, 2005.

[45] E. Huang, L. Dong, A. Chandra, D. A. Kuban, I. I. Rosen, A. Evans, and A. Pollack. Intrafraction prostate motion during imrt for prostate cancer. *Int. J. Radiat. Oncol. Biol. Phys.*, 53(2):261–268, 2002.

[46] Northern Digital Inc. *OPTOTRAK® Rigmaker Guide.* Northern Digital Inc., 2000.

[47] Northern Digital Inc. *OPTOTRAK® 3020 Technical Specifications.* Northern Digital Inc., 2006.

[48] D. A. Jaffray. Emergent technologies for 3-dimensional image-guided radiation delivery. *Semin. Radiat. Oncol.*, 15(3):208–216, 2005.

[49] D. A. Jaffray, D. G. Drake, M. Moreau, A. A. Martinez, and J. W. Wong. A radiographic and tomographic imaging system integrated into a medical linear accelerator for localization of bone and soft-tissue targets. *Int. J. Radiat. Oncol. Biol. Phys.*, 45(3):773–789, 1999.

[50] D. A. Jaffray, D. Yan, and J. W. Wong. Managing geometric uncertainty in conformal intensity-modulated radiation therapy. *Semin. Radiat. Oncol.*, 9(1):4–19, 1999.

[51] A. Jirasek, M. Hilts, C. Shaw, and P. Baxter. Investigation of tetrakis hydroxymethyl phosphonium chloride as an antioxidant for use in x-ray computed tomography polyacrylamide gel dosimetry. *Phys. Med. Biol.*, 51(7):1891 – 1906, 2006.

[52] J. M. Kapatoes, G. H. Olivera, J. P. Balog, H. Keller, P. J. Reckwerdt, and T. R. Mackie. On the accuracy and effectiveness of dose reconstruction for tomotherapy. *Phys. Med. Biol.*, 46(4):943–966, 2001.

[53] A. Khamene, P. Bloch, W. Wein, M. Svatos, and F. Sauer. Automatic registration of portal images and volumetric CT for patient positioning in radiation therapy. *Med. Image Anal.*, 10(1):96–112, 2006.

[54] D. A. Kuban, L. Dong, R. Cheung, E. Strom, and R. De Crevoisier. Ultrasound-based localization. *Semin. Radiat. Oncol.*, 15(3):180–191, 2005.

[55] K. Kuriyama, H. Onishi, N. Sano, T. Komiyama, Y. Aikawa, Y. Tateda, T. Araki, and M. Uematsu. A new irradiation unit constructed of self-moving gantry-CT and linac. *Int. J. Radiat. Oncol. Biol. Phys.*, 55(2):428–435, 2003.

[56] G. J. Kutcher, L. Coia, M. Gillin, W. F. Hanson, S. Leibel, R. J. Morton, J. R. Palta, J. A. Purdy, L. E. Reinstein, G. K. Svensson, M. Weller, and L. Wingfield. Report of the AAPM radiation therapy comittee task group 40. *Med. Phys.*, 21(4):581–618, 1994.

[57] K. M. Langen and D. T. L. Jones. Organ motion and its management. *Int. J. Radiat. Oncol. Biol. Phys.*, 50(1):265–278, 2001.

[58] K. M. Langen, J. Pouliot, C. Anezinos, M. Aubin, A. R. Gottschalk, I.-C. Hsu, D. Lowther, Y.-M. Liu, K. Shinohara, L. J. Verhey, V. Weinberg, and M. Roach III. Evaluation of ultrasound-based prostate localisation for image-guided radiotherapy. *Int. J. Radiat. Oncol. Biol. Phys.*, 57(3):635–644, 2003.

[59] K. M. Langen, Y. Zhang, R. D. Andrews, M. E. Hurley, S. L. Meeks, D. O. Poole, T. R. Willoughby, and P. A. Kupelian. Initial experience with megavoltage (MV) CT guidance for daily prostate alignments. *Int. J. Radiat. Oncol. Biol. Phys.*, 62(5):1517–1524, 2005.

[60] J. Lattanzi, S. McNeeley, A. Hanlon, T. E. Schultheiss, and G. E. Hanks. Ultrasound-based stereotactic guidance of precision conformal external beam radiation therapy in clinically localized prostate cancer. *Urology*, 55(1):73–78, 2000.

[61] J. Lattanzi, S. McNeeley, W. Pinover, E. Horwitz, I. Das, T. E. Schultheiss, and G. E. Hanks. A comparison of daily CT localisation to a daily ultrasound-based system in prostate cancer. *Int. J. Radiat. Oncol. Biol. Phys.*, 43(4):719–725, 1999.

[62] J. Lenarčič and V. Parenti-Castelli. A method for determining movements of a deformable body from spatial coordinates of markers. *J. Robot. Syst.*, 18(12):731–736, 2001.

[63] D. Létourneau, A. A. Martinez, D. Lockman, D. Yan, C. Vargas, G. Ivaldi, and J. Wong. Assessment of residual error for online cone-beam CT-guided treatment of prostate cancer patients. *Int. J. Radiat. Oncol. Biol. Phys.*, 62(4):1239–1246, 2005.

[64] C. C. Ling, E. Yorke, and Z. Fuks. From IMRT to IGRT: frontierland or neverland? *Radiother. Oncol.*, 78(2):119–122, 2006.

[65] H. Liu, Y. Yu, M. C. Schell, W. G. O'Dell, R. Ruo, and P. Okunieff. Optimal marker placement in photogrammetry patient positioning system. *Med. Phys.*, 30(2):103–110, 2003.

[66] T. R. Mackie, T. Holmes, S. Swerdloff, P. Reckwerdt, J. O. Deasy, J. Yang, B. Paliwal, and T. Kinsella. Tomotherapy: a new concept for the delivery of dynamic conformal radiotherapy. *Med. Phys.*, 20(6):1709–1719, 1993.

[67] T. R. Mackie, J. Kapatoes, K. Ruchala, W. Lu, C. Wu, G. Olivera, L. Forrest, J. Tome, W. Welsh, R. Jeraj, P. Harari, P. Reckwerdt, B. Paliwal, M. Ritter, H. Keller, J. Fowler, and M. Mehta. Image guidance for precise conformal radiotherapy. *Int. J. Radiat. Oncol. Biol. Phys.*, 56(1):89–105, 2003.

[68] E. L. Madsen, J. A. Zagzebski, and G. R. Frank. Oil-in-gelatin dispersions for use as ultrasonically tissue-mimicking materials. *Ultrasound Med. Biol.*, 8(3):277–287, 1982.

[69] S. L. Mahan, C. R. Ramsey, D. D. Scaperoth, D. J. Chase, and T. E. Byrne. Evaluation of image-guided helical tomotherapy for the retreatment of spinal metastasis. *Int. J. Radiat. Oncol. Biol. Phys.*, 63(5):1576–1583, 2005.

[70] J. B. Maintz and M. A. Viergever. A survey of medical image registration. *Med. Image. Anal.*, 2(1):1–36, 1998.

[71] M. J. Maryanski, J. C. Gore, R. P. Kennan, and R. J. Schulz. NMR relaxation enhancement in gels polymerized and cross-linked by ionizing radiation: a new approach to 3D dosimetry by MRI. *Magn. Reson. Imaging*, 11(2):253–258, 1993.

[72] J. P. McGahan, J. Ryu, and M. Fogata. Ultrasound probe pressure as a source of error in prostate localization for external beam radiotherapy. *Int. J. Radiat. Oncol. Biol. Phys.*, 60(3):788–793, 2004.

[73] J. E. McGary, B. S. Teh, B. Butler, and W. Grant III. Prostate immobilisation using a rectal balloon. *J. Appl. Clin. Med. Phys.*, 3(1):6–11, 2002.

[74] S. L. Meeks, J. M. Buatti, L. G. Bouchet, F. J. Bova, T. C. Ryken, E. C. Pennington, K. M. Anderson, and W. A. Friedman. Ultrasound-guided extracranial radiosurgery: technique and application. *Int. J. Radiat. Oncol. Biol. Phys.*, 55(4):1092–1101, 2003.

[75] L. Mercier, T. Lango, F. Lindseth, and D. L. Collins. A review of calibration techniques for freehand 3-D ultrasound systems. *Ultrasound Med. Biol.*, 31(2):143–165, 2005.

[76] S. Minohara, T. Kanai, M. Endo, K. Noda, and M. Kanazawa. Respiratory gated irradiation system for heavy-ion radiotherapy. *Int. J. Radiat. Oncol. Biol. Phys.*, 47(4):1097–1103, 2000.

[77] R. Mohan, X. Zhang, H. Wang, Y. Kang, X. Wang, H. Liu, K. K. Ang, D. Kuban, and L. Dong. Use of deformed intensity distributions for on-line modification of image-guided IMRT to account for interfractional anatomic changes. *Int. J. Radiat. Oncol. Biol. Phys.*, 61(4):1258–1266, 2005.

[78] J. Morr, T. DiPetrillo, J. S. Tsai, M. Engler, and D. E. Wazer. Implementation and utility of a daily ultrasound-based localization system with intensity-modulated radiotherapy for prostate cancer. *Int. J. Radiat. Oncol. Biol. Phys.*, 53(5):1124–1129, 2002.

[79] M. A. Mosleh-Shirazi, P. M. Evans, W. Swindell, S. Webb, and M. Partridge. A cone-beam megavoltage CT scanner for treatment verification in conformal radiotherapy. *Radiother. Oncol.*, 48(3):319–328, 1998.

[80] V. Narayana, P. L. Roberson, A. T. Pu, H. Sandler, R. H. Winfield, and P. W. McLaughlin. Impact of differences in ultrasound and computed tomography volumes on treatment planning of permanent prostate implants. *Int. J. Radiat. Oncol. Biol. Phys.*, 37(5):1181–1185, 1997.

[81] T. R. Nelson, D. H. Pretorius, A. Hull, M. Riccabona, M. S. Sklansky, and G. James. Sources and impact of artifacts on clinical three-dimensional ultrasound imaging. *Ultrasound Obstet. Gynecol.*, 16(4):374–383, 2000.

[82] R. P. Parker, P. A. Hobday, and K. J. Cassell. The direct use of CT numbers in radiotherapy dosage calculations for inhomogeneous media. *Phys. Med. Biol.*, 24(4):802–809, 1979.

[83] M. Partridge, M. Ebert, and B-M. Hesse. IMRT verification by three-dimensional dose reconstruction from portal beam measurements. *Med. Phys.*, 29(8):1847–1858, 2002.

[84] K. Paskalev, S. Feigenberg, L. Wang, B. Movsas, D. Laske, and C. Ma. A method for repositioning of stereotactic brain patients with the aid of real-time CT image guidance. *Phys. Med. Biol.*, 50(16):N201–N207, 2005.

[85] K. Paskalev, C. M. Ma, R. Jacob, R. Price, S. McNeeley, L. Wang, B. Movsas, and A. Pollack. Daily target localization for prostate patients based on 3D image correlation. *Phys. Med. Biol.*, 49(6):931–939, 2004.

[86] L. Pisani, D. Lockman, D. Jaffray, D. Yan, A. Martinez, and J. Wong. Setup error in radiotherapy: on-line correction using electronic kilovoltage and megavoltage radiographs. *Int. J. Radiat. Oncol. Biol. Phys.*, 47(3):825–839, 2000.

[87] T. C. Poon and R. N. Rohling. Comparison of calibration methods for spatial tracking of a 3-D ultrasound probe. *Ultrasound Med. Biol.*, 31(8):1095–1108, 2005.

[88] J. Pouliot, A. Bani-Hashemi, J. Chen, M. Svatos, F. Ghelmansarai, M. Mitschke, M. Aubin, P. Xia, O. Morin, K. Bucci, P. Roach III, M. Hernandez, Z. Zheng, D. Hristov, and L. Verhey. Low-dose megavoltage cone-beam CT for radiation therapy. *Int. J. Radiat. Oncol. Biol. Phys.*, 61(2):552–560, 2005.

[89] V. Pratt. Direct least-squares fitting of algebraic surfaces. *Computer Graphics*, 21(4):145–152, 1987.

[90] C. R. Ramsey, K. M. Langen, P. A. Kupelian, D. D. Scaperoth, S. L. Meeks, S. L. Mahan, and R. M. Seibert. A technique for adaptive image-guided helical tomotherapy for lung cancer. *Int. J. Radiat. Oncol. Biol. Phys.*, 64(4):1237–1244, 2006.

[91] R. N. Rohling and A. H. Gee. Issues in 3-D free-hand medical ultrasound imaging. Technical report, Cambridge University Department of Engineering, 1996.

[92] H. M. Sandler, R. L. Bree, P. W. McLaughlin, H. B. Grossman, and A. S. Lichter. Localization of the prostatic apex for radiation therapy using implanted markers. *Int. J. Radiat. Oncol. Biol. Phys.*, 27(4):915–919, 1993.

[93] L. Sciavicco and B. Siciliano. *Modelling and Control of Robot Manipulators*. Springer, second edition, 2001.

[94] E. J. Seppi, P. Munro, S. W. Johnsen, E. G. Shapiro, C. Tognina, D. Jones, J.M. Pavkovich, C. Webb, I. Mollov, L. D. Partain, and R. E. Colbeth. Megavoltage cone-beam computed tomography using a high-efficiency image receptor. *Int. J. Radiat. Oncol. Biol. Phys.*, 55(3):793–803, 2003.

[95] C. F. Serago, S. J. Chungbin, S. J. Buskirk, G. A. Ezzell, A. C. Collie, and S. A. Vora. Initial experience with ultrasound localisation for positioning prostate cancer patients for external beam radiotherapy. *Int. J. Radiat. Oncol. Biol. Phys.*, 53(5):1130–1138, 2002.

[96] M. B. Sharpe, D. J. Moseley, T. G. Purdie, M. Islam, J. H. Siewerdsen, and D. A. Jaffray. The stability of mechanical calibration for a kV cone beam computed tomography system integrated with linear accelerator. *Med. Phys.*, 33(1):136–144, 2006.

[97] R. G. Simpson, C. T. Chen, E. A. Grubbs, and W. Swindell. A 4-MV CT scanner for radiation therapy: the prototype system. *Med. Phys.*, 9(4):574–579, 1982.

[98] A. R. Skovoroda, S. Y. Emelianov, and M. O'Donnell. Tissue elasticity reconstruction based on ultrasonic displacement and strain images. *IEEE Trans. Ultrason. Ferroelectr. Freq. Control*, 42(4):747–765, 1995.

[99] S. W. Smith, H. G. Pavy Jr, and O. T. von Ramm. High-speed ultrasound volumetric imaging system. I. Transducer design and beam steering. *IEEE Trans. Ultrason., Ferroelect., Freq. Contr.*, 38(2):100–108, 1991.

[100] M. H. Smitsmans, J. W. Wolthaus, X. Artignan, J. de Bois, D. A. Jaffray, J. V. Lebesque, and M. van Herk. Automatic localization of the prostate for on-line or off-line image-guided radiotherapy. *Int. J. Radiat. Oncol. Biol. Phys.*, 60(2):623–635, 2004.

[101] W. A. Tomé, S. L. Meeks, N. P. Orton, L. G. Bouchet, and F. J. Bova. Commissioning and quality assurance of an optically guided three-dimensional ultrasound target localization system for radiotherapy. *Med. Phys.*, 29(8):1781–1788, 2002.

[102] J. V. Trapp, S. A. Back, M. Lepage, G. Michael, and C. Baldock. An experimental study of the dose response of polymer gel dosimeters imaged with x-ray computed tomography. *Phys. Med. Biol.*, 46(11):2939–2951, 2001.

[103] J. V. Trapp, G. Michael, Y. de Deene, and C. Baldock. Attenuation of diagnostic energy photons by polymer gel dosimeters. *Phys. Med. Biol.*, 47(23):4247–4258, 2002.

[104] G. M. Treece, A. H. Gee, R. W. Prager, and C. J. C. Cash. High-definition freehand 3-D ultrasound. *Ultrasound Med. Biol.*, 29(4):529–546, 2003.

[105] G. M. Treece, R. W. Prager, A. H. Gee, and L. Berman. Correction of probe pressure artifacts in freehand 3D ultrasound. *Med. Image. Anal.*, 6(3):199–214, 2002.

[106] F. Trichter and R. D. Ennis. Prostate localization using transabdominal ultrasound imaging. *Int. J. Radiat. Oncol. Biol. Phys.*, 56(5):1225–1233, 2003.

[107] M. Uematsu, T. Fukui, A. Shioda, H. Tokumitsu, K. Takai, T. Kojima, Y. Asai, and S. Kusano. A dual computed tomography linear accelerator unit for stereotactic radiation therapy: a new approach without cranially fixated stereotactic frames. *Int. J. Radiat. Oncol. Biol. Phys.*, 35(3):587–592, 1996.

[108] F. Van den Heuvel, T. Powell, E. Seppi, P. Littrupp, M. Khan, Y. Wang, and J. D. Forman. Independent verification of ultrasound based image-guided radiation treatment, using electronic portal imaging and implanted gold markers. *Med. Phys.*, 30(11):2878–2887, 2003.

[109] M. van Herk, D. Jaffray, A. Betgen, P. Remeijer, J. Sonke, M. Smitsmans, L. Zijp, and J. Lebesque. First clinical experience with cone-beam CT guided radiation therapy; evaluation of dose and geometric accuracy. *Int. J. Radiat. Oncol. Biol. Phys.*, 60(1):S196, 2004.

[110] E. Vigneault, J. Pouliot, J. Laverdiere, J. Roy, and M. Dorion. Electronic portal imaging device detection of radioopaque markers for the evaluation of prostate position during megavoltage irradiation - a clinical study. *Int. J. Radiat. Oncol. Biol. Phys.*, 37(1):205–212, 1997.

[111] C. M. Washington and D. Leaver. *Principals and Practice of Radiation Therapy.* Mosby, St. Louis, Missouri, second edition, 2004.

[112] C. Wu, R. Jeraj, G. H. Olivera, and T. R. Mackie. Re-optimization in adaptive radiotherapy. *Phys. Med. Biol.*, 47(17):3181–3195, 2002.

[113] N. J. Yue, J. P. Knisely, H. Song, and R. Nath. A method to implement full six-degree target shift corrections for rigid body in image-guided radiotherapy. *Med. Phys.*, 33(1):21–31, 2006.

[114] L. Zhang, A. S. Garden, J. Lo, K. K. Ang, A. Ahamad, W. H. Morrison, D. I. Rosenthal, M. S. Chambers, X. R. Zhu, R. Mohan, and L. Dong. Multiple regions-of-interest analysis of setup uncertainties for head-and-neck cancer radiotherapy. *Int. J. Radiat. Oncol. Biol. Phys.*, 64(5):1559–1569, 2006.

Appendix A

Ultrasound Tissue-Equivalent Gel Manufacture

The ingredients required to make approximately $500mL$ of the ultrasound tissue-equivalent gel described in [14] and used for phantom construction in this thesis are shown in Table A.1.

Table A.1: Constituents of the ultrasound tissue-equivalent gel.

Constituent	Amount
Distilled water	$500mL$
n-Propanol	$60.8mL$
Agar (high gel strength)	$17g$

To manufacture the gel, use the following steps:

1. Combine water and n-Propanol in a beaker.
2. Slowly pour the agar powder into the solution while stirring on high-speed using a magnetic stirrer.
3. Cover the top of the beaker with saran wrap.
4. Heat the mixture on medium heat while stirring on high-speed until a temperature of $90°C$ is reached and a clear solution is obtained.
5. Reduce stirring speed to low and allow liquid to cool to $45°C$.
6. Slowly pour the liquid into the container to be used for gelling to avoid creating air bubbles.

7. Place the liquid in a refrigerator until coagulation is complete.

If desired, the solid gel, once set, can be covered using saran wrap to prevent desiccation. The gel is resistant to bacterial/fungal invasion, and if kept in the refrigerator when not in use, it can last indefinitely.

Appendix B

Polymer Gel Manufacture

To make $600g$ of the polymer gel described in [51] and used in Chapter 5 of this thesis, the ingredients shown in Table B.1 are required.

Table B.1: Constituents of the polymer gel.

Constituent	Amount
Acrylamide (electrophoresis grade) $\geq 99\%$, powder	$18g$
N,N'-Methylenebisacrylamide (electrophoresis grade), $\geq 98\%$, powder	$18g$
Gelatin (Type A from porcine skin)	$30g$
Tetrakis (hydroxymethyl) phosphonium chloride solution	$0.43ml$
Distilled water	$533.43ml$

Since acrylamide, bis-acrylamide, and tetrakis are toxic, use extreme caution and proper protection when handling these materials:

- Wear a labcoat or overalls, goggles, laboratory gloves, and a respirator.
- Do not dispose into the sink. Store excess unwanted chemical in a container for later removal by toxic waste disposal.
- Clean all equipment, glassware, and bench-top thoroughly after use.
- Do not store the gel in a refrigerator where food is also kept.

To manufacture the gel, use the following steps:

1. Measure the amount of water required into a beaker.

2. Apply medium heat to the beaker while stirring at high-speed using a magnetic stirrer.

3. Mix gelatin powder with water while stirring. Adjust heat to maintain a solution temperature of $40 - 45°C$. Wait until gelatin is completely dissolved and solution is clear.

4. Stir in acrylamide powder. Maintain constant solution temperature and stir speed. The acrylamide should dissolve easily.

5. Stir in half the bis-acrylamide powder. Maintain constant solution temperature and stir speed. Wait until the bis-acrylamide completely dissolves (may take 5-10 minutes), then stir in the remaining bis-acrylamide, and repeat.

6. Measure the required amount of tetrakis using a Hamilton MICROLITER^{TM} syringe. Mix into solution while maintaining heat and stir speed.

7. Stop stirring and heating the solution. Slowly and carefully pour the solution into the container to be used for housing the gel.

8. Place the gel in a refrigerator until coagulation is complete. It will remain sensitive to x-ray radiation for approximately 6 hours after manufacture.

9. Store excess gel (if any) in another container until it can be properly disposed by toxic waste removal. Do not pour down the sink.

Appendix C

3D Ultrasound-to-Ultrasound Registration Results for Target Localisation

The 3D ultrasound-to-ultrasound registration results ${}^{U'}\mathbf{T}_{U}$ used to localise all 4 targets in Chapter 5 with the proposed 3D ultrasound patient positioning system are shown below and summarised as 3 translations and 3 rotations (roll-pitch-yaw angles) [93] in Table C.1. As it can be seen, ${}^{U'}\mathbf{T}_{U}$ was close to the identity matrix for all 4 targets. It was previously shown in Equation 3.13 in Section 3.4 that this can help to minimise the effect of systematic imaging errors, such as probe calibration error, on the target localisation accuracy of the proposed system.

$$\text{Target 1 } {}^{U'}\mathbf{T}_{U} = \begin{bmatrix} 0.99974 & -0.021118 & -0.0082633 & 2.9631 \\ 0.021433 & 0.99896 & 0.040223 & -2.3522 \\ 0.0074054 & -0.04039 & 0.99916 & -3.5231 \\ 0 & 0 & 0 & 1 \end{bmatrix} \tag{C.1}$$

$$\text{Target 2 } {}^{U'}\mathbf{T}_{U} = \begin{bmatrix} 0.99897 & 0.045297 & 0.003369 & 4.823 \\ -0.045152 & 0.99837 & -0.034934 & 4.6864 \\ -0.0049459 & 0.034746 & 0.99938 & -1.356 \\ 0 & 0 & 0 & 1 \end{bmatrix} \tag{C.2}$$

$$\text{Target 3 } {}^{U'}\mathbf{T}_{U} = \begin{bmatrix} 0.99973 & -0.013939 & 0.018477 & 1.8191 \\ 0.013537 & 0.99967 & 0.021735 & -1.4094 \\ -0.018773 & -0.021479 & 0.99959 & -0.74345 \\ 0 & 0 & 0 & 1 \end{bmatrix} \tag{C.3}$$

$$\text{Target 4 } {}^{U'}\mathbf{T}_{U} = \begin{bmatrix} 0.99647 & 0.052349 & 0.065586 & -4.5151 \\ -0.05407 & 0.99823 & 0.024756 & 2.2901 \\ -0.064174 & -0.028215 & 0.99754 & 3.3446 \\ 0 & 0 & 0 & 1 \end{bmatrix} \tag{C.4}$$

Table C.1: The homogeneous transformation matrix ${}^{U'}\mathbf{T}_{U}$ for 3D ultrasound localisation of all 4 targets in Chapter 5 expressed in terms of 3 translations x, y, z, and 3 rotations φ, ϑ, ψ (roll-pitch-yaw angles).

Target	$x(mm)$	$y(mm)$	$z(mm)$	$\varphi(°)$	$\vartheta(°)$	$\psi(°)$
1	3.0	-2.4	-3.5	1.2	-0.4	-2.3
2	4.8	4.7	-1.4	-2.6	0.3	2.0
3	1.8	-1.4	-0.7	0.8	1.1	-1.2
4	-4.5	2.3	3.3	-3.1	3.7	-1.6